

Validation of Load Models and Calculations of Response for a Monopile in Steep Water Waves

Master Thesis at Department of Dynamics of Maritime Systems (TU Berlin)
and at Department of Marine Technology (NTNU)

Submitted by: Miloš Ristić
Matriculation No.: 351271
Course of study: Naval Architecture and Ocean Engineering
Submission date: October 8, 2018
First supervisor: Prof. Dr.-Ing. Andrés Cura Hochbaum
Second supervisor: Prof. Erin E. Bachynski (NTNU)

Eidesstattliche Erklärung

Hiermit erkläre ich, dass ich die vorliegende Arbeit selbstständig und eigenhändig sowie ohne unerlaubte fremde Hilfe und ausschließlich unter Verwendung der aufgeführten Quellen und Hilfsmittel angefertigt habe.

Berlin, den 08.10.18

Abstract

The aim of this thesis was to explore challenges related to severe wave loading on offshore wind turbines. The focus was on large-diameter inertia-dominated monopile foundations. To achieve the research aim, three main tasks were set. First, numerous hydrodynamic loading cases were calculated using Morison, Rainey, and FNV load models for steep water waves. The calculations were developed in *MATLAB* and were limited to non-breaking forces that act on a cylindrical and rigid pile, in both regular and irregular wave fields. Second, the calculations were validated with experimental data. The experimental data were obtained from the model testing in a wave flume, using the same simplifications as in the previous calculations. These tests were carried out by SINTEF Ocean and NTNU. Third, considering an idealized single-degree-of-freedom rotational system with a flexible pile, a numerical model was also developed in *MATLAB*. This model enabled an initial forecast of the structural response.

Keywords: offshore wind turbine, monopile, higher-order wave loads, hydrodynamic model testing, structural response

Kurzfassung

Das Ziel dieser Abschlussarbeit war es die Herausforderungen zu untersuchen, die entstehen, wenn starke Wellenlasten auf eine Offshore-Windkraftanlage wirken. Der Fokus lag hierbei auf Monopile- Gründungsstrukturen mit großen Durchmessern, die hauptsächlich durch Trägheitskräfte belastet werden. Um dieses Ziel zu erreichen, wurden drei primäre Aufgaben gesetzt. Als erstes wurden zahlreiche hydrodynamische Lastfälle mithilfe von Morison-, Rainey- und FNV- Gleichungen in steilen Wellen berechnet. Die Berechnungen wurden mithilfe von *MATLAB* durchgeführt und beschränkten sich auf nicht-brechende Kräfte, die auf einen zylindrischen und starren Pfahl in regulären und irregulären Wellenfeldern wirken. Zweitens wurden die Berechnungen anhand von experimentellen Daten validiert, die aus den Modelltests in einem Wellentank gewonnen wurden. Diese Tests wurden von SINTEF Ocean and NTNU mit selben Vereinfachungsprinzipien durchgeführt, die in der Berechnung verwendet wurden. Drittens wurde anhand von einem idealisierten Pfahl mit einem Freiheitsgrad, ein numerisches Modell in *MATLAB* entwickelt. Das Modell ermöglichte eine erste Abschätzung der Strukturantwort.

Schlüsselwörter: Offshore Windkraftanlage, Monopile, Wellenlasten höherer Ordnung, Hydrodynamische Modelluntersuchungen, Strukturantwort

Contents

LIST OF FIGURES III

LIST OF TABLES V

NOMENCLATURE..... VI

1 INTRODUCTION..... 1

1.1 BACKGROUND AND MOTIVATION..... 1

1.2 OBJECTIVES..... 2

2 THEORETICAL BACKGROUND..... 4

2.1 REGULAR WAVE KINEMATICS 4

2.1.1 *Linear Wave Theory (LWT)*..... 4

2.1.2 *Nonlinear Wave Theories*..... 7

2.1.3 *Validity and Applicability of Wave Theories*..... 12

2.2 IRREGULAR WAVE KINEMATICS 14

2.3 WAVE LOADS..... 16

2.3.1 *Morison Equation*..... 17

2.3.2 *MacCamy-Fuchs Equation*..... 18

2.3.3 *Rainey Equation*..... 18

2.3.4 *FNV Equation*..... 19

2.4 DYNAMICS OF OFFSHORE WIND TURBINES 20

3 LOAD MODELS FOR A STIFF STRUCTURE 22

3.1 ENVIRONMENTAL CONDITIONS 22

3.1.1 *Regular Waves* 22

3.1.2 *Irregular Waves* 23

3.2 REGULAR WAVE ANALYSIS 24

3.2.1 *Wave Number* 25

3.2.2 *Wave Elevation*..... 26

3.2.3 *Wave Load*..... 27

3.2.4 *Higher Order Loads*..... 31

3.3 IRREGULAR WAVE ANALYSIS 33

3.4 CONCLUSIONS 36

4 VALIDATION USING MODEL TEST MEASUREMENTS 37

4.1 EXPERIMENTAL SETUP 37

4.2 PRINCIPLES OF MODEL TESTING..... 39

4.3 ANALYSIS OF THE MEASURED DATA..... 41

4.3.1 *Regular Wave Validation* 41

4.3.2 *Irregular Wave Validation* 51

4.4 CONCLUSIONS 53

5 CALCULATED RESPONSES FOR THE FLEXIBLE STRUCTURE 55

5.1 STRUCTURAL PARAMETERS 55

5.2 RESPONSE AND DISPLACEMENT ANALYSIS 57

5.3 CONCLUSIONS 61

6	SUMMARY AND RECOMMENDATIONS FOR FURTHER WORK.....	62
6.1	SUMMARY	62
6.2	RECOMMENDATIONS FOR FURTHER WORK	63
	REFERENCES.....	I
A.	APPENDIX	IV
A.1	<i>MATLAB</i> CODE	IV
A.2	DIAGRAMS	XII

List of Figures

FIGURE 1: ILLUSTRATION OF CONSTANT STRETCHING METHOD [37].....	6
FIGURE 2: STRETCHING OF VELOCITY PROFILE [11].....	7
FIGURE 3: WAVE PROFILES OF FIRST AND SECOND ORDER WAVES [12].....	8
FIGURE 4: WAVE SORTS [14].....	11
FIGURE 5: REGIONS OF VALIDITY FOR VARIOUS GRAVITY WAVE THEORIES [36].....	13
FIGURE 6: COMPOSITION OF IRREGULAR SEA STATE AND WAVE SPECTRUM [38].....	15
FIGURE 7: JONSWAP SPECTRUM FOR $HS = 4\text{ m}$, $Tp = 8\text{ s}$, AND FOR $\gamma = 1$, $\gamma = 2$, AND $\gamma = 5$ [11].....	16
FIGURE 8: WAVE FORCES ON A VERTICAL PILE [12].....	17
FIGURE 9: RESPONSE REGIONS UNDER DIFFERENT DAMPING COEFFICIENTS [39].....	21
FIGURE 10: 50-YEAR ENVIRONMENTAL CONTOURS FOR DIFFERENT WIND SPEEDS [33].....	23
FIGURE 11: VALIDITY REGION OF INVESTIGATED SEA STATES FOR TWO WATER DEPTHS, MODIFIED [36].....	24
FIGURE 12: CALCULATED ELEVATION OF FOUR TYPES OF STOKES WAVES.....	26
FIGURE 13: TWO WAVE CONDITIONS AT WATER DEPTH $D = 33\text{ M}$	27
FIGURE 14: HORIZONTAL WAVE PARTICLE VELOCITIES AND ACCELERATIONS OVER Z FOR THE WHOLE TIME-STEP (SECOND-ORDER STOKES KINEMATICS, $D = 9\text{ M}$).....	28
FIGURE 15: RELATIVE IMPORTANCE OF INERTIA, DRAG AND DIFFRACTION WAVE FORCES [22].....	28
FIGURE 16: TIME SERIES OF THE TOTAL WAVE FORCES AT SWL FOR TWO WAVE CONDITIONS USING MORISON EQUATION WITH SECOND-ORDER KINEMATICS ($D = 9\text{ M}$).....	29
FIGURE 17: TOTAL AND MAXIMUM INERTIAL AND DRAG FORCE DISTRIBUTION FOR TWO WAVE CONDITIONS USING MORISON EQUATION WITH SECOND-ORDER KINEMATICS ($D = 9\text{ M}$).....	29
FIGURE 18: TOTAL AND MAXIMUM FORCE DISTRIBUTION OVER STRUCTURE LENGTH USING MORISON EQUATION WITH THE SECOND ORDER STOKES WAVE KINEMATICS ($D = 9\text{ M}$).....	30
FIGURE 19: FFT OF THE GLOBAL FORCE FOR FOUR WAVE CONDITIONS IN TWO WATER DEPTHS, USING SECOND- ORDER MORISON EQUATION ($D = 9\text{ M}$).....	31
FIGURE 20: JONSWAP SPECTRA FOR ALL SIX SEA STATES.....	33
FIGURE 21: WAVE ELEVATIONS OVER 3-HOUR TIME.....	34
FIGURE 22: GLOBAL FORCE DEVELOPMENT OVER 3-HOUR TIME FOR TWO WATER DEPTHS ($D = 9\text{ M}$).....	35
FIGURE 23: MODEL TEST SET-UP.....	37
FIGURE 24: MONOPILE SET-UP [33].....	38
FIGURE 25: SURFACE OF THE MODEL.....	40
FIGURE 26: MEASURED WAVE ELEVATION FOR TWO WAVE CONDITIONS.....	41
FIGURE 27: COMPARISON OF THE TOTAL FORCE DISTRIBUTION OVER THE LENGTH OF STRUCTURE, RS20T6.....	42
FIGURE 28: COMPARISON OF THE TOTAL DISTRIBUTION OVER THE LENGTH OF STRUCTURE, RS20T14.....	43
FIGURE 29: COMPARISON OF HIGHEST GLOBAL FORCES FOR ALL WAVE PERIODS.....	44
FIGURE 30: COMPARISON OF HIGHEST GLOBAL MOMENTS FOR ALL WAVE PERIODS.....	44
FIGURE 31: COMPARISON OF RELATIVE GLOBAL FORCES BETWEEN TWO PILE DIAMETERS FOR $S = 1/20$	45
FIGURE 32: COMPARISON OF HIGHEST RELATIVE GLOBAL FORCES BETWEEN TWO PILE DIAMETERS, $S = 1/40$	46
FIGURE 33: COMPARISON OF MEASURED AND CALCULATED TOTAL & GLOBAL FORCES OVER A TIME STEP.....	47
FIGURE 34: COMPARISON OF FIRST-ORDER FORCE-TERM MAGNITUDES.....	48
FIGURE 35: COMPARISON OF SECOND-ORDER FORCE-TERM MAGNITUDES.....	48
FIGURE 36: COMPARISON OF THIRD-ORDER FORCE-TERM MAGNITUDES.....	49
FIGURE 37: COMPARISON OF FOURTH-ORDER FORCE-TERM MAGNITUDES.....	49
FIGURE 38: COMPARISON OF FIFTH AND SIXTH ORDER FORCE-TERM MAGNITUDES.....	50
FIGURE 39: EXAMPLES OF IRREGULAR WAVE SPECTRA FOR IH9T12.5G2.6 IN TWO WATER DEPTHS.....	51
FIGURE 40: MONOPILE MODEL WITH THE FIRST EIGENMODE [35].....	55
FIGURE 41: COMPARISON OF THE STRUCTURAL RESPONSE, RS20T14.....	58

FIGURE 42: COMPARISON OF THE STRUCTURAL RESPONSE. RS20T14 (ZOOMED) 58

FIGURE 43: COMPARISON OF THE MAX. DISPLACEMENT ALONG THE STRUCTURE FOR DYNAMIC AND STATIC
EXCITATION, RS20T14 59

FIGURE 44: COMPARISON OF THE STRUCTURAL RESPONSE, RS20R6 60

FIGURE 45: COMPARISON OF THE MAX. DISPLACEMENT ALONG THE STRUCTURE FOR DYNAMIC AND STATIC
EXCITATION, RS20R6 61

FIGURE 46: WHOLE WAVE-ELEVATION SET FROM GENTLE TO SEVERE WAVE CONDITIONS (MEASURED) XII

FIGURE 47: MEASURED WAVE ELEVATION FOR TWO SELECTED SEA STATES (D = 33 M)..... XII

FIGURE 48: GLOBAL FORCE FOR TWO WAVE CONDITIONS IN TWO WATER DEPTHS AND FOR TWO PILE DIAMETERS,
USING FIRST-ORDER MORISON EQUATION XIII

FIGURE 49: GLOBAL FORCE FOR TWO WAVE CONDITIONS IN TWO WATER DEPTHS AND FOR TWO PILE DIAMETERS,
USING FIRST-ORDER MACCAMY-FUCHS EQUATION (DRAG TERM INCLUDED) XIV

FIGURE 50: FFT OF THE GLOBAL FORCE FOR FOUR WAVE CONDITIONS IN TWO WATER DEPTHS, USING SECOND-
ORDER MORISON EQUATION (D = 11 M)..... XV

FIGURE 51: COMPARISON OF THE TOTAL FORCE DISTRIBUTION OVER THE LENGTH OF STRUCTURE, D = 33 M
(CALCULATED FORCE OBTAINED FROM THE MEASURED WAVE-ELEVATION IS ADDITIONALLY GIVEN) XVI

FIGURE 52: COMPARISON OF HIGHEST GLOBAL FORCES FOR ALL WAVE PERIODS XVII

FIGURE 53: EXAMPLES OF IRREGULAR WAVE SPECTRA FOR IH6.5T12G1.4 IN TWO WATER DEPTHS..... XVIII

FIGURE 54: COMPARISON OF HIGHEST GLOBAL MOMENTS FOR ALL WAVE PERIODS..... XVIII

FIGURE 55: EXAMPLES OF IRREGULAR WAVE SPECTRA FOR IH6.8T13.2G1 IN TWO WATER DEPTHS..... XVIII

List of Tables

TABLE 1: RANGES OF APPLICATION OF REGULAR WAVE THEORIES [22]	13
TABLE 2: WAVE PERIODS	22
TABLE 3: WAVE STEEPNESSES	22
TABLE 4: IRREGULAR SEA STATE CHARACTERISTICS	23
TABLE 5: FOUR SELECTED REGULAR WAVE CONDITIONS	25
TABLE 6: FROUDE SCALING TABLE	40
TABLE 7: MAXIMUM GLOBAL FORCE IN IRREGULAR WAVES (WATER DEPTH $D = 27$ M).....	52
TABLE 8: MAXIMUM GLOBAL FORCE IN IRREGULAR WAVES (WATER DEPTH $D = 33$ M).....	52
TABLE 9: COMPARISON OF THE CALCULATION METHODS	53
TABLE 10: POLYNOMIAL COEFFICIENTS.....	56
TABLE 11: SDOF MODEL PARAMETERS	56

Nomenclature

Abbreviations

DNV	Det Norske Veritas
FFT	Fast Fourier Transformation
IFFT	Inverse Fast Fourier Transformation
JONSWAP	Joint North Sea Wave Observation Project (spectrum)
LWT	Linear Wave Theory
MWL	Mean Water Level
OWT	Offshore Wind Turbine
PM	Pierson-Moskowitz (spectrum)
SDOF	Single Degree of Freedom (system)
SWL	Still Water Level

Latin Symbols

a	Horizontal water particle acceleration	m/s ²
A	Response amplitude	m
a_n	Fifth-order Stokes coefficients	-
c	Wave celerity	m/s
\bar{c}	Critical damping	Ns/m
c_a	Added-mass coefficient	-
c_d	Drag coefficient	-
c_m	Added-mass coefficient	-
d	Water depth	m
D	Pile diameter	m
F	Force	N
F_N	Froude number	-
g	Gravitational acceleration	m/s ²
H	Wave height	m
H_S	Significant wave height	m
k	Wave number	rad/m
\bar{k}	Generalized stiffness	N/m
L	Wave length	m
\bar{m}	Generalized mass	kg
M	Moment	Nm
\bar{P}	Generalized force	N
p_n	Polynomial coefficients	-
r	Radius of the surface hemispheres and monopile	m
Re	Reynold number	-
S	Wave steepness parameter	-
S_n	Wave spectrum	m ² s
t	Time	s
T	Wave period	s

T_p	Peak spectral period	s
u	Horizontal water particle velocity	m/s
U_r	Ursell number	-
w	Vertical water particle velocity	m/s
w_d	Structural displacement	m
x	Wave position	m
Y	Dynamic structural response	-
Y_{stat}	Static structural response	-
z	Vertical coordinate (zero at mean water surface)	m

Greek Symbols

γ	Peak enhancement factor	-
ε_n	Wave phase	-
ϵ	Perturbation expansion parameter	-
ζ	Wave elevation	m
ζ_a	Wave amplitude	m
λ	Scaling factor	-
ρ	Water density	kg/m ³
ν	Kinematic viscosity	m ² /s
φ	Random phase	-
ϕ	Velocity potential	-
ϕ_s	Shape function	-
ψ	Stream function	-
ω	Angular wave frequency	1/s

1 Introduction

1.1 Background and Motivation

Mitigation of the global effects of climate change can be best achieved by utilizing renewable and sustainable energy resources. In the last decade, offshore wind turbines (OWTs) have become one of the fastest growing sources of electrical energy among renewable-energy generators. This growth is largely due to expansion of the near-shore wind farms around European shores. Europe provides almost 90% of the world's capacity for offshore wind energy generation. The European offshore wind energy market in 2016 was estimated at 13.4 GW. With an annual growth of 12%, the figure is expected to reach 29.8 GW by 2024 [1].

Compared to onshore wind turbines, the main advantages of offshore turbines are wind speeds that are higher, more constant, and more predictable; low visual intrusion and noise; easy transportation of high-capacity wind turbines; lower transmission costs for coastal cities; and conservation of land. Offshore turbines can also help to avoid overexploitation of potential onshore sites. To maximize the impact of sustainable energy from OWTs and to render it more affordable and attractive, the turbine's structure must be designed optimally. The correct design can cut the investment and service costs, thus contributing greatly to achieving economic viability.

Depending on the installation site and its water depth, a wide variety of foundation types can be used, such as monopile, jackets, gravity-based, or floating foundations. The most commonly used foundation for an OWT structure is a monopile. As of 2016, 81% of European OWTs were equipped with them [2]. A monopile is a long steel or concrete pipe, hammered or drilled into the seabed at a predetermined depth. The embedded length can be calculated as a function of the pile's diameter and the relative pile–soil stiffness ratio [3]. Typically (and simplified), 40% to 50% of the length is embedded into the sea bottom [4]. This type of foundation is the market leader due to its structural simplicity, competitive production costs, and robust installation.

Since the power output of a wind turbine depends directly on the area of the rotor-blade sweep, fewer structures are needed per unit of power output. The scale of turbines has steadily been increasing, and with it the scale of monopiles – in both their length and diameter. Early designs targeted a pile diameter of $D = 4\text{ m}$ and they currently anticipate $D = 10\text{ m}$ and more. The monopiles for these large diameters are called “XL monopiles” and their power output reaches 12 MW [5]. They typically consist of a pile, a transitional piece, a tower, a nacelle (with a generator), and three rotor blades.

This study was conducted as a part of project related to WAS XL, which stands for “wave loads and soil support for extra-large monopiles.” Hence, specific environmental conditions in the North Sea were provided [6]. In the project, water depths of $d = 27\text{ m}$ and $d = 33\text{ m}$ were considered, and in steep waves the wave loads are assumed to dominate. This means the wind loads can be neglected initially. The rough environmental conditions, which

would otherwise be examined in the scope of this thesis, are too heavy for a turbine to maintain energy production, so that the turbine is assumed to be parked.

The investigated wave conditions at these water depths lie mostly in the range of relative intermediate depths (relative to wave period). In contrast to deep water situations, accurate prediction of kinematics and structural response in these shallower waters is generally more challenging. The shallow-water effects cause strong nonlinearities and more complex wave-structure interactions. Wave kinematics are often modelled as linearized or weakly nonlinear for simplification. However, in nonlinear waves there are “hidden” terms of a higher frequency that can significantly affect the extreme loads and cause nonlinear and unwanted responses of the monopile structure. These include springing and ringing. They could also influence the fatigue life of the structure. “*Springing is characterized as a steady-state response to sum-frequency wave effects*”, whereas ringing can be described as fast build-up of transient structural deflection, usually followed by a steep wave in irregular waves [7]. The second, third, or fourth excitation period of the shallower water waves might coincide with the lowest resonance period of fixed offshore turbines, which is typically low for these structures, at around $T_R \approx 4 \text{ s}$ [8]. Furthermore, under the investigated wave conditions and given monopile diameters of $D = 9 \text{ m}$ and $D = 11 \text{ m}$, the free-surface diffraction effects might be significant.

Several methods are used to calculate hydrodynamic loads. The most widely applied is a well-known Morison equation with its inertia and drag terms. Under consideration of diffraction effects, the inertia term of the Morison equation can be modified using the MacCamy-Fuchs equation. Other theories that might be more accurate for capturing the higher-order load components are the Rainey and FNV (Faltinsen, Newman, and Vinje [9]) theories. They account for certain diffraction effects and include further nonlinear terms that are not necessarily present for Morison equation. Those terms are introduced in a form of additional distributed and point forcing terms, which should reproduce the real condition even more accurately.

1.2 Objectives

Precise prediction of the hydrodynamic loads and structural response of a monopile is essential for achieving structural optimization, through avoiding overly conservative designs while maintaining adequate safety. Fulfilling all these aspects brings increased economic viability. The core aim of this thesis was thus to analyze and compare the existing theories about hydrodynamic load prediction. This includes calculating and examining the wave kinematics, the load distribution maxima along the structure, and the global load development over time and over frequencies, using different wave kinematics and load-calculation methods. Furthermore, the results in a study like this should be validated with the data from model test experiments. The thesis focuses on regular waves using Stokes kinematics. However, initial irregular wave analysis was conducted to better understand the impact of irregular waves.

To simplify the study, neither wind nor current forces are included; only head sea is considered. The work is further limited to the modelling of undisturbed, long-crested waves acting on an idealized pile of constant diameter over the whole structure length.

The final aim of the thesis was to preliminary calculate and analyze the structural

response using a flexible, single-degree-of-freedom monopile, using differential equations for dynamic equilibrium. As an excitation input, the calculated and measured loads were used, and the results were compared. The rough structural characteristics needed to solve the differential equations were given by the *SIMA* simulation tool. All calculations and post-processing work were completed with *MATLAB* software.

2 Theoretical Background

In this chapter, the relevant methods and effects that are essential for understanding the thesis contents are discussed. However, a basic understanding of certain aspects of classical mechanics is required to fully comprehend the content. The chapter is focused on wave kinematics and wave loads. Additionally, an overview of structural dynamics and the equation of motion is presented.

2.1 Regular Wave Kinematics

To describe wave kinematics and predict the effects of wave conditions, approximations in the form of wave theories have been developed. The accurate description of wave kinematics is relevant for calculating the loads that waves cause.

Wave kinematics can be categorized into two main groups: regular versus irregular wave kinematics. The regular waves have constant (co)sinusoidal wave properties: constant amplitude ζ_a , wave length L , and wave period k [10]. They can be subdivided into linear and nonlinear waves. A linear wave has a sinusoidal surface profile with small amplitude and steepness, whereas a nonlinear wave has larger amplitude, sharper crests, and flatter troughs than the linear wave.

Three main parameters are used in describing all wave theories: wave height H , wave period T , and water depth d . Based on these parameters, the most relevant wave theory is selected, as discussed in section 2.1.3.

2.1.1 Linear Wave Theory (LWT)

The simplest and most commonly applied method of describing wave kinematics is linear wave theory, also called airy theory. It is often used as a first step in predicting wave behavior in engineering practice. This first-order theory is generally applicable for ocean gravity waves with a small amplitude ζ_a relative to the wave length λ and water depth d [11].

The assumptions in this theory are that water is *inviscid* and *incompressible* and fluid motion is *irrotational*. Therefore, the velocity potential ϕ exists and fulfills the Laplace equation $\nabla^2\phi = 0$. In addition, the following three boundary conditions must be satisfied to derive the expression for the velocity potential:

1. Kinematic free surface boundary condition, which states that the free surface cannot be penetrated by water particles.
2. Dynamic free surface boundary condition, which states that the pressure variations at the surface are negligible.

3. Bottom boundary condition, which states that the value of the vertical water velocity at the seabed is zero.

Based on the assumptions, a solution for the velocity potential ϕ in finite water depths ($0.05 < d/L < 0.5$) is given by the following equation [12]:

$$\phi = \frac{\zeta_a g}{\omega} \frac{\cosh k(z+d)}{\cosh kd} \sin(kx - \omega t) \quad (1)$$

where g is the gravitational acceleration, $\omega = 2\pi/T$ is the angular frequency, $k = 2\pi/L$ is the wave number, and the z is the vertical axis. The variable ζ_a represents the amplitude of the wave, which is measured as the distance between the highest point of the wave and the mean water level (MWL) ($z=0$). Due to fully symmetrical wave shape, the amplitude of the wave is half the wave height $\zeta_a = H/2$. The surface elevation, which varies with space x and time t , can be described as follows:

$$\zeta = \zeta_a \cos(kx - \omega t). \quad (2)$$

Therefore, the wave elevation reaches its maximum at the wave crest, when $x = 0$ and $t = 0$. Because the wave number k or wave length L are usually unknown, it is important to obtain them by satisfying the dispersion relation. The equation describes the relation between angular frequency ω and the wave number k as follows:

$$\omega = \sqrt{kg \tanh kd}. \quad (3)$$

The derivative of ϕ in any direction equals the flow velocity in that direction. The horizontal wave kinematics, local velocity u , and local acceleration a at any distance are therefore derived as follows:

$$u = \frac{\partial \phi}{\partial x} = \zeta_a \omega \frac{\cosh k(z+d)}{\sinh kd} \cos(kx - \omega t) \quad (4)$$

$$a = \frac{\partial u}{\partial t} = \zeta_a \omega^2 \frac{\cosh k(z+d)}{\sinh kd} \sin(kx - \omega t). \quad (5)$$

Here it should be noted that a phase shift exists between velocity and acceleration of 90° due to different sine and cosine functions. The velocity is in the phase with the wave elevation. Therefore, maximum positive velocity occurs at the wave crest, zero velocity at the MWL, and the highest negative velocity at the trough. By contrast, acceleration reaches its maximum when wave elevation is at MWL. Lastly, according to the free surface boundary conditions, the LWT is valid only up to the MWL.

Modified Linear Wave Theory (Stretching)

Given that the LWT is valid only up to MWL, it does not describe wave kinematics at points above that level. However, to accurately determine the hydrodynamic loads, it is important to include this region. An extrapolation of the kinematics above MWL would introduce extremely high wave-particle velocity at the top of the wave, which would lead to highly inaccurate load predictions. Two possible solutions are constant stretching and Wheeler stretching [10]:

1. Constant (vertical) stretching is a simple model, where the wave kinematics at the MWL are used for the whole region above MWL. If the particle of the wave elevation is below the MWL, the integration is conducted to that water level. This principle is illustrated in Figure 1. The dynamic pressure is assumed to be constant, whereas the pressure below MWL remains unaffected.

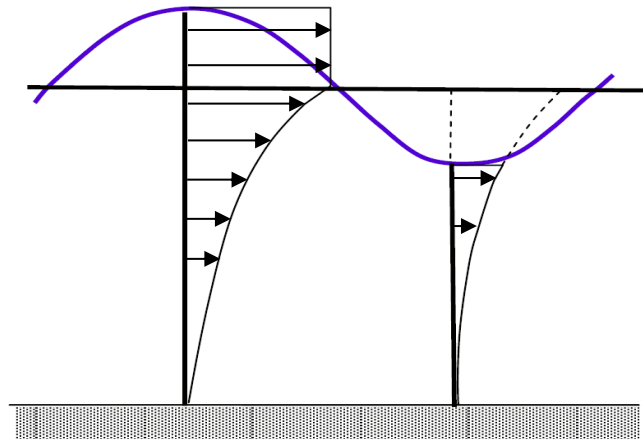


Figure 1: Illustration of constant stretching method [37]

2. In Wheeler stretching, wave kinematics from linear theory at the MWL are shifted to the actual free surface $z = \zeta$. Figure 2 shows the distributions of velocity in a stretched and a non-stretched state. Wheeler stretching is a nonlinear extension of linear theory, since the resulting horizontal force on the vertical pile includes second-order effects. The vertical coordinate is stretched as follows [11]:

$$z = \frac{z_s - \zeta}{1 + \frac{\zeta}{d}}; \quad -d < z < 0; \quad -d < z_s < 0. \quad (6)$$

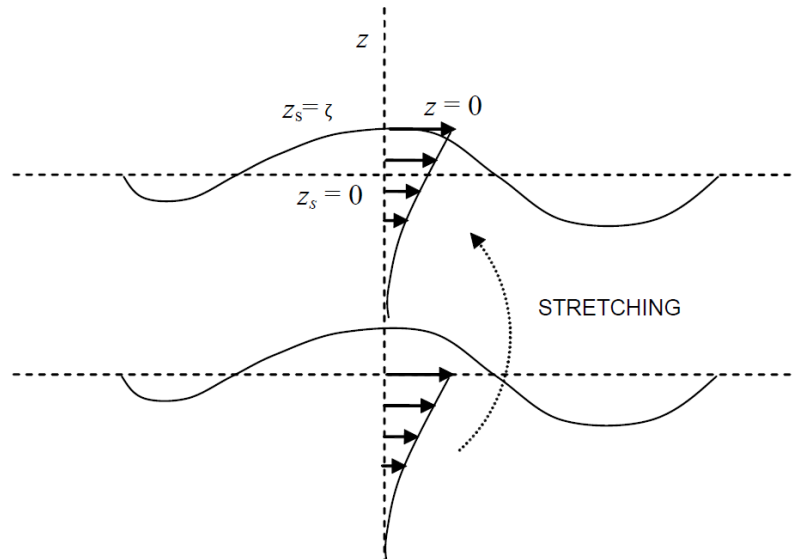


Figure 2: Stretching of velocity profile [11]

For this thesis, constant stretching was selected as the more useful method, because it is known that Wheeler stretching significantly underpredicts the magnitude of the effects around MWL and at lower levels, especially in steep waves [13], [11]. Also, because only linear effects are used in constant stretching, a direct comparison between linear and non-linear kinematics is possible.

2.1.2 Nonlinear Wave Theories

To better approximate “real” wave kinematics, which would in turn improve accuracy (compared with LWT) when the wave amplitude is not small, nonlinear wave theories were developed. Nonlinear waves are nonsymmetric about MWL, with steeper and narrower crests and wider and shallower troughs than linear waves. Linear wave theory is unable to capture these nonlinear features of wave kinematics.

Depending on the wave characteristics and the mathematical methods used to obtain their solutions, nonlinear wave theories can be categorized into various types, namely the Stokes, cnoidal, solitary, bousinesq, and stream wave theories. All of them can be directly implemented in force calculation formulas.

An initial option for improving the LWT is to use Stokes wave theories. They are based on a perturbation solution using successive approximations. Generally, including more higher-order terms leads to improved agreement with the “real” wave kinematics, which improves the accuracy over LWT when the wave amplitude is not small. This is because the higher-order theories describe the mass transport, shoaling, reflection of the waves, and nonlinear characteristics better [14].

The first-order Stokes theory corresponds exactly to the airy wave theory (see the previous chapter) and represents the first-order approximation for satisfying the free surface conditions. Expansion up to the fifth-order is possible to better satisfy the nonlinear free surface agreement.

A disadvantage of the perturbation techniques is that the potential loses its superposition property and therefore cannot be transferred to the irregular wave field. Furthermore, it is only

applicable for wave amplitudes smaller than all other length scales. Despite these drawbacks, higher-order Stokes wave theory is still helpful for studying nonlinear wave kinematics.

Second-Order Stokes Theory

The first and simplest way to include the nonlinear effects of wave kinematics is to use the second-order Stokes theory. To solve the nonlinear boundary value problem, Stokes developed this theory in 1847. Its formulation is based on the perturbation expansions of the linear elements. The theory introduces the second component of twice the frequency, but with smaller amplitude and therefore reduced contribution.

Analogous to linear waves, with an identical first term and an additional nonlinear second term, the velocity potential is described as follows [15], [12]:

$$\phi = \frac{Hg}{2\omega} \frac{\cosh k(z+d)}{\cosh kd} \sin(kx - \omega t) + \frac{3H^2\omega}{32} \frac{\cosh 2k(z+d)}{\sinh^4 kd} \sin 2(kx - \omega t) \quad (7)$$

The surface wave elevation profile is given by:

$$\zeta = \frac{H}{2} \cos(kx - \omega t) + \frac{\pi H^2}{8\lambda} \frac{\cosh kd}{\sinh^3 kd} (2 + \cosh 2kd) \cos 2(kx - \omega t). \quad (8)$$

The resulting second-order waves become slightly asymmetric with respect to MWL and surge with an increase of wave steepness. This means that the crests are steeper, and the troughs are flatter than for linear waves, making the wave form more recognizable for waves observed at sea. The amplitude is higher and troughs shallower, hence the wave height does not change. The profile of this wave is shown in Figure 3, together with a first-order wave profile.

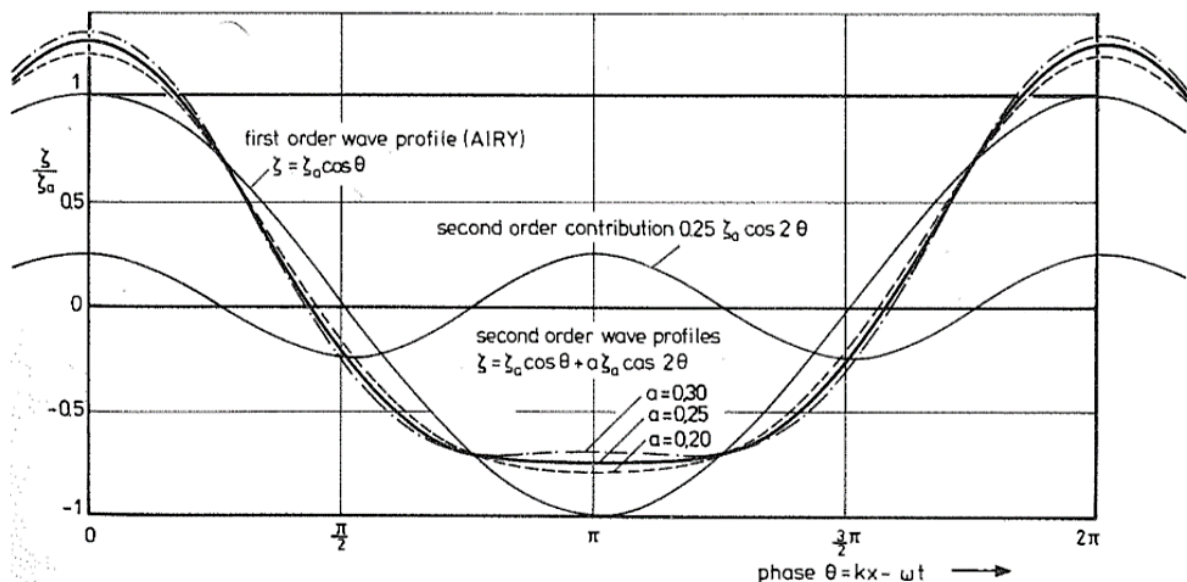


Figure 3: Wave profiles of first and second order waves [12]

The horizontal velocity and acceleration under second-order waves are given by the following equations:

$$u = \frac{\partial \phi}{\partial x} = \frac{H}{2} \omega \frac{\cosh k(z+d)}{\sinh kd} \cos(kx - \omega t) + \frac{3H^2 \omega k \cosh 2k(z+d)}{16 \sinh^4 kd} \cos 2(kx - \omega t) \quad (9)$$

$$a = \frac{\partial u}{\partial t} = \frac{H}{2} \omega^2 \frac{\cosh k(z+d)}{\sinh kd} \sin(kx - \omega t) + \frac{3H^2 \omega^2 k \cosh 2k(z+d)}{8 \sinh^4 kd} \sin 2(kx - \omega t). \quad (10)$$

It should be noted that the linear dispersion relation from Eq. 3 holds for second-order Stokes waves. Hence, the wave length L remains independent of wave height. This makes the calculation almost as simple as for the linear airy theory.

Fifth-order Stokes Theory

To describe waves even more realistically, a jump from the second order to the fifth order is widely used in practical applications. There are various options for calculating the fifth-order Stokes kinematics. The first reliable method was developed in 1961 by Skjelbreia and Hendrickson [16]. In 1985, John D. Fenton noticed that their method showed calculation errors for solving fifth-order Stokes theory. The analytical – and more accurate – approach of Fenton was selected for this thesis [17]. Fenton introduced a dimensionless perturbation expansion parameter $\epsilon = kH/2$. This made the calculations even simpler; the main challenges were to calculate the wave number, insert all coefficients, and eventually apply all higher-order terms. Each term in the series is smaller in amplitude than the previous one, but not less relevant. Their phases also differ due to different frequencies.

Because of nonlinear effects, the wave length depends not only on the wave period and water depth, as in the case of linear dispersion, but also on wave height. In this case, the wave length increases. There are different approaches for solving this equation, for example the approximation formula of Chang [18], which should yield explicit and concise results. The approach is based on extension of the calculation of linear dispersion by Fenton [19]. Other solutions are iterative, numerical calculations. Based on Fenton [17], the velocity potential is given by the following equation:

$$\phi = C_0 \sqrt{\frac{g}{k^3}} \sum_{n=1}^5 \epsilon^n a_n \cosh nk(z+d) \sin n(kx - \omega t) \quad (11)$$

where

$$a_1 = A_{11} + \epsilon^2 A_{31} + \epsilon^4 A_{51}$$

$$a_2 = A_{22} + \epsilon^2 A_{42}$$

$$a_3 = A_{33} + \epsilon^2 A_{53} \quad (12)$$

$$a_4 = A_{44}$$

$$a_5 = A_{55}$$

The coefficients A_{ij} , B_{ij} , and C are dimensionless functions of the water depth d and wave number k . The wave elevation is calculated by the following equation:

$$\zeta = \frac{1}{k} \sum_{n=1}^5 \epsilon^n b_n \cos n(kx - \omega t) \quad (13)$$

$$b_1 = 1 + \epsilon^2 B_{31} - \epsilon^4 (B_{53} + B_{55})$$

$$b_2 = B_{22} + \epsilon^2 B_{42}$$

$$b_3 = -B_{31} + \epsilon^2 B_{53} \quad (14)$$

$$b_4 = B_{44}$$

$$b_5 = B_{55}.$$

Finally, the horizontal velocity u and acceleration a , under a fifth-order wave, are given by the following equations:

$$u = \frac{\partial \phi}{\partial x} = C_0 \sqrt{\frac{g}{k}} \sum_{n=1}^5 \epsilon^n a_n n \cosh nk(z + d) \cos n(kx - \omega t) \quad (15)$$

$$a = \frac{\partial u}{\partial t} = C_0 \omega \sqrt{\frac{g}{k}} \sum_{n=1}^5 \epsilon^n a_n n^2 \cosh nk(z + d) \sin n(kx - \omega t). \quad (16)$$

Boussinesq Wave Theory

Boussinesq theory is applicable for weakly non-linear and moderately long waves in shallow water. The theory is thus ideal in coastal work but is also frequently used in monopile wind turbine projects. The main idea of Boussinesq wave theory is to eliminate the vertical coordinate from the flow equations, while retaining certain influences of the vertical structure of the flow below water waves.

Cnoidal Wave Theory

Cnoidal wave theory follows from a shallow water approximation, where it is assumed that waves are much longer than the water depth. Compared to Stokes theory, the waves in this theory are distinguished by sharper crests that are separated with wider troughs (Figure 4). The

theory uses many Jacobian elliptic functions and integrals, which renders its calculation effortful; for an extensive application, cnoidal theory is often too complex [20].

Solitary Wave Theory

Solitary waves are characterized as periodic waves with sharp peaks and exceptionally wide troughs (Figure 4). The profile exists only above the MWL and consists of a single crest, which does not oscillate. These waves emerge from cnoidal waves in shallow waters when the wave conditions are close to breaking events or when wave length is infinite [14]. Solitary waves do not occur in nature, but certain phenomena – such as tsunamis – occasionally behave in similar ways. Therefore, and because solitary waves do not represent a wave train, this theory is not applicable for offshore design in the North Sea.

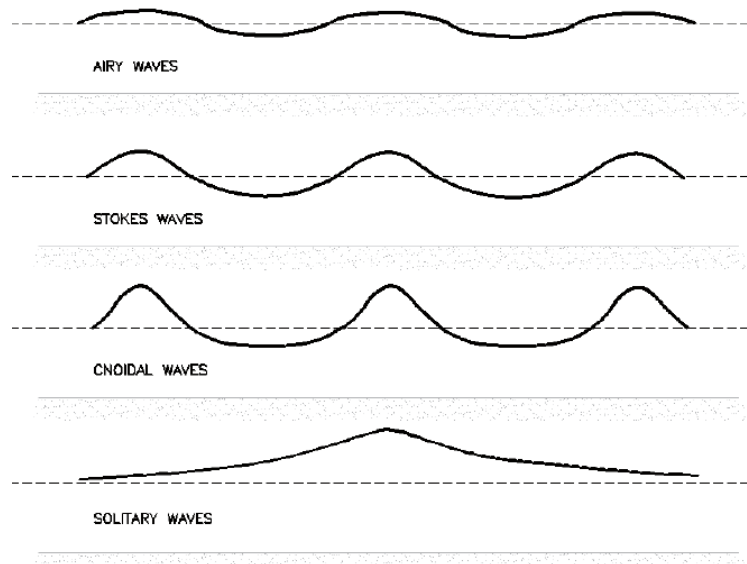


Figure 4: Wave sorts [14]

Stream Function Wave Theory

This theory is a solely numerical approach to approximate wave profiles; it has a wide range of uses. As the name implies, the waves are described by stream function rather than by velocity potential. The theory was developed by Dean in 1965 [21] for symmetrical and nonlinear waves, much like higher-order Stokes theory. Both stream function wave theory and higher-order Stokes theory satisfy the Laplace equation. The greatest advantage of the stream function theory is its range of applicability. Compared to Stokes' theories, this theory should rather be applied for shallow waters. The stream function theory describes the wave as follows:

$$\psi(x, z) = cz + \sum_{n=1}^N X(n) \cdot \sinh nk(z + d) \cdot \cos nkx. \quad (17)$$

Here, c represents the wave celerity and N is the order of the theory. The order of the stream function theory describes the nonlinearity of the wave. The closer the wave is to the breaking wave limits, the more terms are required to provide an accurate representation of the wave. The first order of the theory $N = 1$ corresponds to linear wave theory [11].

2.1.3 Validity and Applicability of Wave Theories

To ensure that a suitable theory is selected, the range of its validity must be established. Three variables that are used in describing wave theories can help to identify valid wave theories, namely wave height H , wave period T , and water depth d . Based on their relationships, the best wave theory for a case can be determined. These three variables can also be used to create the following three widespread and non-dimensionless variables, which can confirm the range of application for a wave theory [22]:

- Wave steepness parameter: $S = \frac{H}{L}$
- Shallow water parameter: $\mu = \frac{d}{L}$
- Ursell parameter: $U_r = \frac{S}{4\pi^2 \cdot \mu^3}$

Figure 5 presents the various regions of validity. Linear theory, which is shown in yellow, is recommended for transitional and deep waters with small wave steepness. The higher-order Stokes theories are applicable for steeper waves, mostly in deep water and in parts of the intermediate depth range. It should be noted that the range of validity of fourth-order Stokes theory may be replaced with the more popular fifth-order Stokes theory. The light-blue area shows the range of validity for cnoidal wave theory; the dark-blue area shows the range extension by numerical approximations using fifth-order stream-function theory.

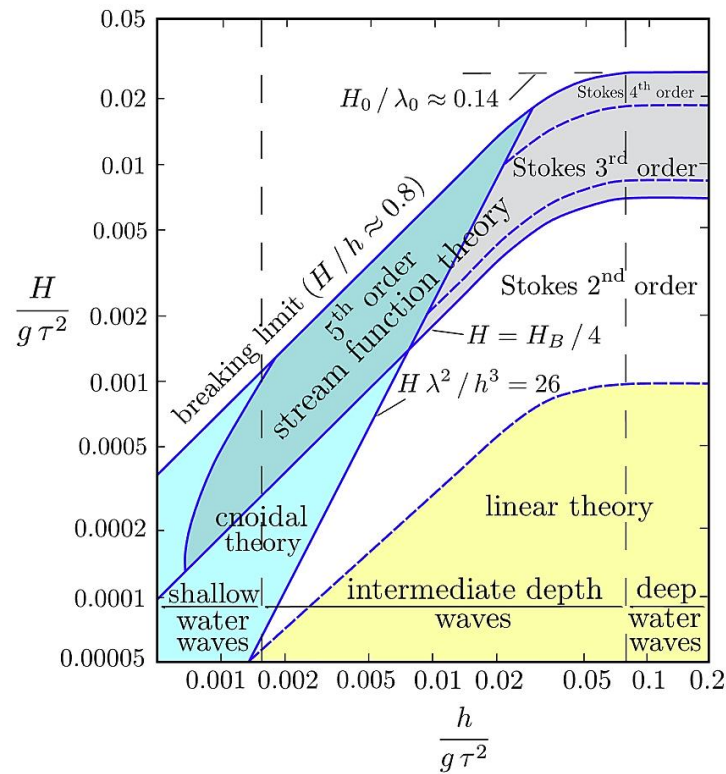


Figure 5: Regions of validity for various gravity wave theories [36]

The area of applicable theories is enveloped by two wave-breaking criteria. The first is the maximum wave steepness for periodic and propagating deep-water waves. Its value is $H/L \approx 0.142$, so the wave height is about one-seventh of the wave length L . The second criterion counts for the shallow and intermediate waters and lies around $H/D \approx 0.89$. In Table 1, all ranges of application according to DNV GL (Det Norske Veritas) are presented.

Table 1: Ranges of application of regular wave theories [22]

Theory	Application	
	Water Depth	Approximate range
Linear (airy) wave	Deep to shallow	$S < 0.006$; $S/\mu < 0.03$
Second-order Stokes wave	Deep to shallow	$U_r < 0.65$; $S < 0.04$
Fifth-order Stokes wave	Deep and intermediate	$U_r < 0.65$; $S < 0.14$
Cnoidal wave	Intermediate and shallow	$U_r > 0.65$; $\mu < 0.125$

In contrast to the statements from the previous subchapter, the higher orders are not always advantageous. For instance, second-order Stokes theory would give unrealistic results for shallow waters; fifth-order is even more limited regarding deep waters. Therefore, increasing the order not only increases the complexity but also imposes limitations for the applicability of theory, where strong inaccuracies might occur.

2.2 Irregular Wave Kinematics

The main drivers of sea waves are global and local winds. They force the waves to travel in different directions over variable distances, thereby making the ocean surface highly irregular. To mathematically replicate these pseudo-random processes, the sea surface must be reduced to a single point and then the surface elevation must be measured or calculated over time. Through superposition, an irregular sea can be modeled as a sum of many regular harmonic wave components, where each wave component is assigned random phase angles. To be exact, the wave elevation of an irregular sea state, ζ , can be expressed as a summation of the individual amplitudes ζ_a , angular frequencies ω , and phases ε :

$$\zeta(t) = \sum_{n=1}^N \zeta_{a,n}(\omega) \cdot \cos(k_n x - \omega_n t + \varepsilon_n) \quad (18)$$

Here, the random phase angles ε are uniformly distributed in a range between 0° and 360° and constant over time. Angular frequencies ω_n and wave number k_n are, as in LWT, related by the dispersion relationship. The contributions of wave kinematics for each wave component were also summed up to form the wave kinematics for the sea surface, as follows:

$$u(t) = \sum_{n=1}^N \zeta_a \omega_n \frac{\cosh k_n(z+d)}{\sinh k_n d} \cos(k_n x - \omega_n t + \varepsilon_n) \quad (19)$$

$$a(t) = \sum_{n=1}^N \zeta_a \omega_n^2 \frac{\cosh k_n(z+d)}{\sinh k_n d} \sin(k_n x - \omega_n t + \varepsilon_n). \quad (20)$$

It is necessary to use irregular wave models to represent the waves in this stochastic or instantaneous behavior. If the time varying signal that is mentioned above is Fourier transformed, it is possible to obtain a wave spectrum, which represents the density of energy. The measured or raw wave spectrum is given by the following equation:

$$S(\omega) = \frac{2}{\Delta\omega} |\zeta_a(\omega)|^2 \quad (21)$$

where

$$\Delta\omega = \frac{2\pi}{\Delta T}. \quad (22)$$

Figure 6 shows the connection between a time domain solution of the waves (Eq.18) and the frequency domain representation of the wave in the form of a spectrum $S(\omega)$.

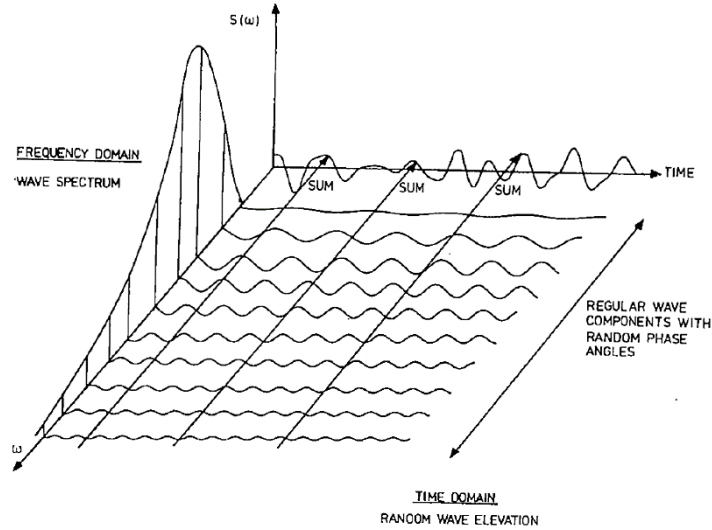


Figure 6: Composition of irregular sea state and wave spectrum [38]

If the spectrum data cannot be obtained from measurements, it is common practice to use numerical approximations of wave spectra for wind-generated waves, such as the Pierson-Moskowitz (PM) spectrum and JONSWAP spectrum. They are both empirically gained, have only one peak, and define the distribution of energy according to frequency within the ocean. Their applicability depends solely on geographical area and the severity of the sea state [11].

In the case of fully developed sea, such as in the Atlantic Ocean, DNV [11] recommended using the Pierson-Moskowitz spectrum S_{PM} , which is calculated as follows:

$$S_{PM}(\omega) = \frac{5}{16} \cdot H_S^2 \omega_P^4 \cdot \omega^{-5} \exp\left(-\frac{5}{4} \left(\frac{\omega}{\omega_P}\right)^{-4}\right). \quad (23)$$

Here, H_S is the significant wave height, which is defined as the average of the highest one-third among waves. It is the most important quantity used in describing the sea state. Furthermore, $\omega_P = 2\pi/T_P$ is the angular spectral frequency where the wave spectrum has its maximum value, and T_P represents its period.

The North Sea conditions cannot be assumed to be a fully developed sea. Therefore, it is more suitable to use the JONSWAP spectrum S_J . The basis of its equation, according to DNV, is the Pierson-Moskowitz spectrum:

$$S_J(\omega) = A_\gamma S_{PM}(\omega) \cdot \gamma^{\exp\left(-0.5 \left(\frac{\omega - \omega_P}{\sigma \cdot \omega_P}\right)^2\right)} \quad (24)$$

where

$$A_\gamma = 1 - 0.287 \ln(\gamma) \quad (25)$$

and

$$\sigma = \begin{cases} 0.07, & \omega \leq \omega_P \\ 0.09, & \omega > \omega_P. \end{cases} \quad (26)$$

Here, γ represents the peak shape parameter. If the value of the shape parameter is $\gamma = 1$, there is no difference between the two spectra. In Figure 7, the influence of the peak-shape parameter in a JONSWAP spectrum is presented.

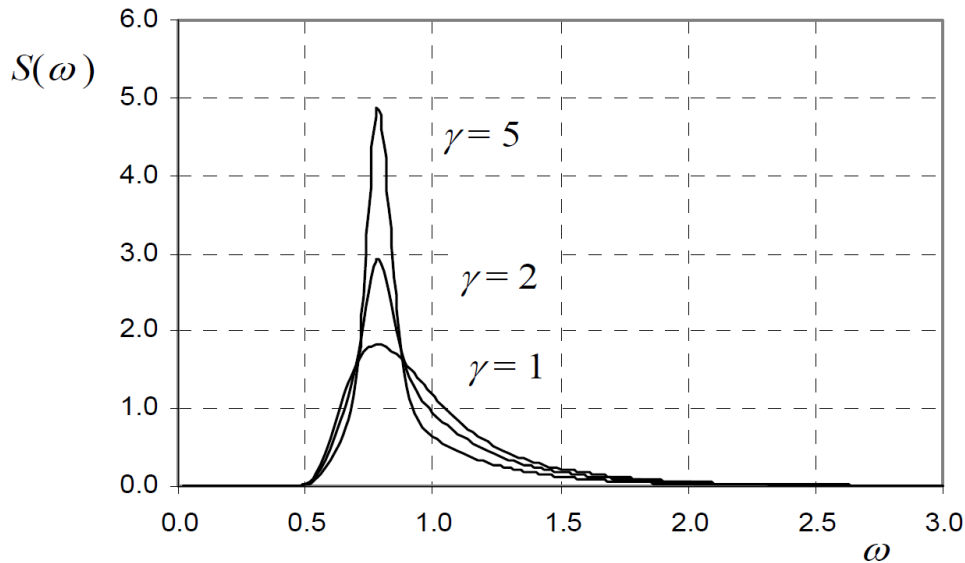


Figure 7: JONSWAP spectrum for $H_s = 4 \text{ m}$, $T_p = 8 \text{ s}$, and for $\gamma = 1$, $\gamma = 2$, and $\gamma = 5$ [11]

The choice of the theoretical spectrum should be based on factors such as the sea state, state of development, water depth, fetch length, and the combination of wind sea and swell. Although PM and JONWAP are the most frequently used spectra, other descriptions do exist. Two noteworthy spectra are the TMA spectrum and Two Peak spectrum. For more information, interested readers should consult DNV [11], since the topic falls beyond the scope of this thesis.

Lastly, those models solely provide an approximation of actual measured spectra under certain conditions and in certain locations. If it is possible to obtain data from long-term measurements for a site to create a “real” spectrum instead, the real spectrum should be used in calculations to achieve more accurate results [23]. It is also possible to implement the second-order correction for irregular waves to yield more realistic results. This step fell beyond the scope of the current study.

2.3 Wave Loads

The loads acting on an OWT are primarily wind and wave loads. The environmental conditions, which fall within the scope of this thesis, were too heavy for the turbine to still produce energy; therefore, they were omitted. Thus, only the wave loads were examined.

To calculate the loads acting on a monopile, there are different approaches to evaluating the magnitudes of linear and nonlinear force terms. In all of them, incident wave kinematics are transformed to structural loads. The Morison equation and MacCamy-Fuchs equation might not be suitable for accurately capturing higher-order effects (higher-order distortion) because they neglect the loads from nonlinear potentials. Therefore, the Rainey equation and FNV theory were additionally investigated. The nonlinear force terms are typically much smaller than the linear terms. Nonetheless they are important to account for, as their frequencies may coincide

with the natural frequencies of the structure and cause resonance behavior of the structure. These higher-order forces are mainly caused by including the area above MWL in the integration of the global force.

2.3.1 Morison Equation

The most widely employed method for calculating horizontal sea loads in offshore fields is the Morison equation. This semi-empirical method gained its popularity because of its efficient calculations and convenient implementation. In the case of a slender, vertical, cylindrical body, the equation considers only two forces: inertial force F_m and nonlinear drag force F_d . Figure 8 shows these two Morison forces acting on a pile.

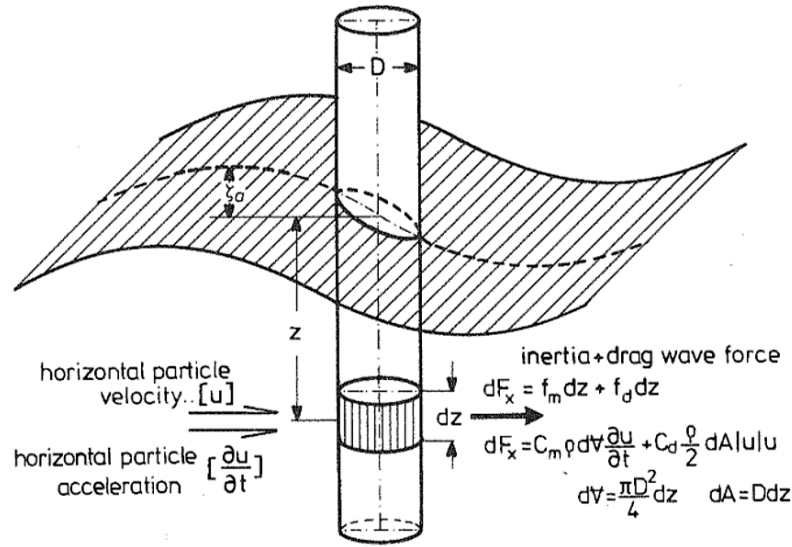


Figure 8: Wave forces on a vertical pile [12]

Using the conventions shown in Figure 8, the force unit length dF_x can be written as follows:

$$dF_x = dF_m + dF_d = C_m \rho \pi \frac{D^2}{4} a dz + C_d \rho \frac{D}{2} u |u| dz. \quad (27)$$

Here, the force acts on a section of length dz . The variables u and a represent the undistributed wave-particle velocity and acceleration respectively. The $\rho = 1025 \text{ kg/m}^3$ term is the water density, D is the pile diameter, C_m is the added-mass coefficient, and C_d is the drag coefficient. The first coefficient, C_m , is usually called an inertia term and is caused by Froud-Krylov and hydrodynamic mass forces. The second, C_d , is a viscous term that includes the form and friction drag [12]. Those two coefficients depend on the shape of the structure, presence of marine growth (i.e. structure roughness) and the specific load case [23].

In the drag force dF_d , the absolute value of horizontal particle velocity is used to maintain the same phase of the force and velocity. The relative velocity of the structure is ignored here, since its magnitude is negligible compared to the water particle velocities. The Morison equation assumes hydrodynamic transparency of the structure, which is achieved when the dimension of the structure is small relative to the wave length $D < 0.2 L$ [10], [22]. This being case, the structure has no significant effect on the waves.

Based on the potential flow solution, the undisturbed velocity u and acceleration a are applied in the Morison load model for sections up to the free surface level $z = \zeta$. Lastly, it should be noted that the inertia and drag loads are phase-shifted by 90° . This means that the peak load of the drag and inertia loads occur at different time instants and their amplitudes thus cannot simply be added. The global wave loads can be obtained by integrating Eq. 27 from the seabed to the free surface level.

2.3.2 MacCamy-Fuchs Equation

In cases where a monopile cannot be assumed to be a transparent structure ($D > 0.2 L$), a diffraction effect must be considered. For this purpose, MacCamy and Fuchs reformulated the inertia term of the Morison equation, which includes the free surface diffraction of linear waves only [24]. The result leads to significant load reductions for shorter waves. The expression for horizontal force per unit axial length is given by the following equation:

$$dF_x = \frac{2\rho g H \cosh k(z+d)}{k \cosh kd} A(kr) \cos(\omega t - \alpha) \quad (28)$$

where

$$A(kr) = \frac{1}{\sqrt{(J'_1(kr))^2 + (Y'_1(kr))^2}} \quad (29)$$

and

$$\alpha = \tan^{-1} \left(\frac{J'_1(kr)}{Y'_1(kr)} \right). \quad (30)$$

In these equations, J_1 and Y_1 are Bessel functions and r represents the radius of the monopile. The total force on the cylinder is obtained by integrating dF up to the surface level together with the drag term of the Morison equation.

2.3.3 Rainey Equation

In most practical cases, the Morison equation is suitable for determining the linear terms of the loading. The limitation in using the Morison equation mainly lies in the integration method, which ignores the free surface piecing effect at the wave-structure intersection. Hence, to accurately capture the critical nonlinear effects, this equation might be inadequate because it often underpredicts higher-order loads [25]. This situation led to the need for a more accurate model that can precisely determine higher-order loads acting on a monopile. A well-established potential-flow model was provided by the work of Rainey (1989) [26] and Rainey (1995) [27].

The calculation of the Rainey equation is based on the Morison equation, with an extension in the form of two additional terms. These terms are an axial divergence correction and a surface intersection point force. The first additional force term corrects the assumption

that a cylinder is slender in the vertical direction. It can be described as the rate of added-mass change in the vertical direction; the total force acting on a pile is given by the following equation [26]:

$$F_{x,AD} = \int_{-d}^{\zeta} (c_m - 1) \rho \pi \frac{D^2}{4} u \frac{\partial w}{\partial z} dz. \quad (31)$$

Here, $\frac{\partial w}{\partial z}$ is the vertical velocity, differentiated with respect to z .

The second additional term represents the change in kinetic flow energy associated with an alteration of wetted cylinder area. Its center of action is at the intersection of the cylinder with the free surface [28]. The pressure field in the free surface decays over distance, proportional to the cylinder radius, which leads to this point load [29]. Using the velocity components at $z = 0$, the force is calculated as follows, according to Rainey (1995):

$$F_{x,SI} = -\frac{1}{2} (c_m - 1) \rho \pi \frac{D^2}{4} u^2 \frac{\partial \zeta}{\partial x} \quad (32)$$

where $\frac{\partial \zeta}{\partial x}$ is the slope of the surface elevation, to any order, and represents the change in surface elevation along the diameter of monopile. Due to the maximum value of acceleration and inertial force at MWL, the point load is lumped down to that position. This also enables a direct comparison using FNV theory, which is discussed in the next section.

These terms can be used to calculate linear and nonlinear wave forces, since their inputs are the wave kinematics, which can be either linear or nonlinear. However, the terms are expected to be relatively small in magnitude but can lead to higher harmonic load components.

2.3.4 FNV Equation

The initial FNV theory by Faltinsen et al. (1995) [9] was developed to calculate the loads on a vertical, circular, free-surface-piercing, bottom-mounted and non-moving cylinder for infinite water depth. The regular third-order Stokes waves with frequency ω were used to calculate the force. This theory is based on the potential flow of an incompressible fluid [30]. More recently, Kristiansen [30] expanded FNV theory to include finite water depths and possibly to account for fifth-order wave kinematics. This method is based on potential flow theory, with the following assumptions: the waves do not break, flow separation is insignificant, and there is no far-field wave generation by the cylinder.

For horizontal loads, the FNV equation contains the mass term from the Morison equation, with two additional terms from nonlinear free-surface conditions. Furthermore, FNV agrees with the distributed force terms of Rainey, so that the only difference between the two load models is the additional point force [30]:

$$F_x^\Psi = \rho \pi \frac{D^2}{g} u^2 \dot{u}. \quad (33)$$

The center of action and the point at which all quantities are evaluated is the MWL.

2.4 Dynamics of Offshore Wind Turbines

In the previous sections, the loads and load cases that are vital for designing offshore energy structures were discussed. To assess the functionality and structural integrity of a design, it is crucial to predict the motion and structural responses. A reliable and robust design should be based on accurate calculation of loads and responses. Here, a simple model of the first generalized mode of the monopile is proposed.

Depending on the level of simplification, the tower foundation of the wind turbine can be viewed as a beam or group of beams with elastic boundary conditions at the soil–pile interface. The simplest way of calculating the response is by solving the linear equation of motion for a single-degree-of-freedom system (SDOF). The relevant equation is derived from the second Newtonian law, as follows:

$$\vec{F} = m\vec{a} = m\ddot{Y} \Rightarrow \quad (34)$$

$$m\ddot{Y} + c\dot{Y}(t) + kY(t) = F. \quad (35)$$

The left side of Eq. 35 represents the mechanical properties of the structure, whereas the right side describes the load to which the structure is subjected. The mechanical properties involve the mass of the structure m , damping coefficient c , and stiffness k . Multiplied with the second derivative \ddot{Y} , first derivative \dot{Y} of the response, and response itself Y , respectively, these variables create inertia, damping, and restoring forces. The natural frequency of a SDOF-structure can be calculated as follows:

$$\omega_n = \sqrt{\frac{k}{m}}. \quad (36)$$

This simple relation between stiffness k and mass m is referred to as the “undamped natural frequency” of the system [31]. Depending on where the load frequency lies compared to the natural frequency of the system, three response regions can be distinguished [23]:

- *Quasi-static region* or stiffness-dominated region ($\omega < \omega_n$)
- *Resonance* ($\omega \cong \omega_n$)
- *Inertia-dominated region* ($\omega > \omega_n$)

In the *quasi-static region*, the loading force is lower than the natural frequency. The structure follows the force nearly instantaneously, as if it is excited by a static load. This response is characteristic for rigid platforms that are exposed to wave forces of the first order. When the load frequency lies within a narrow region of the system’s natural frequency, the system is in *resonance*. In such cases, a rough equilibrium exists between the damping force and the inertial force, which causes the response to be significantly larger than it would usually be. The amplitude of this response depends on the damping ability of the system. Therefore, it is customary to design offshore structures to avoid resonance by placing the natural frequency beyond the range of environmental frequency, or increasing the damping.

Finally, for load frequencies that are meaningfully higher than the natural frequency, the system is in an *inertia-dominated region*. The structure cannot follow the excitation behavior, which leads to a small dynamic response [32]. Figure 9 shows the described regions under different damping coefficients. The damping is crucial for the response level when the structure is near the resonance range. Increased damping reduces the resonant portion of the dynamic response.

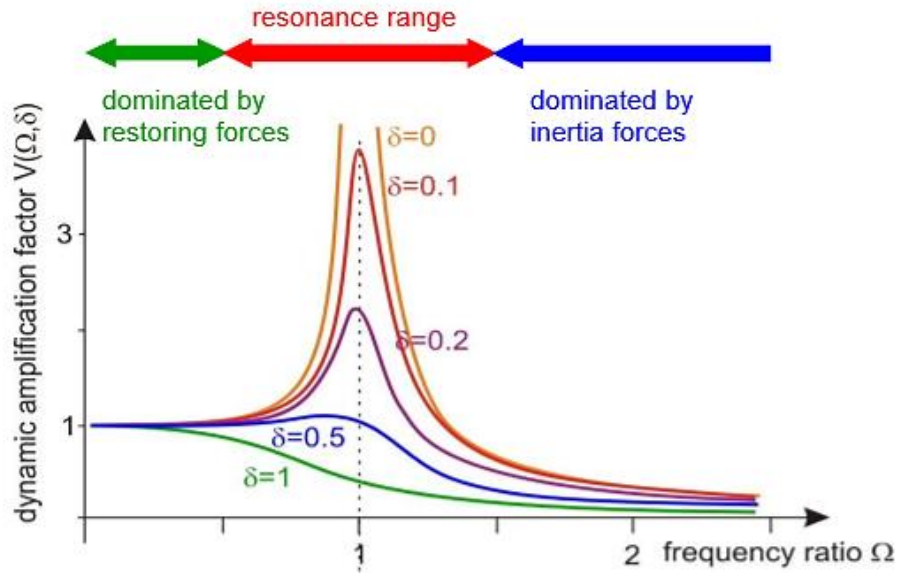


Figure 9: Response regions under different damping coefficients [39]

3 Load Models for a Stiff Structure

This chapter starts by introducing the environmental conditions and then explains, in depth, how the calculations were performed. The results of the selected sea conditions are presented, compared, and briefly discussed. The discussion includes several investigation methods for capturing and describing as many occurring effects as possible. The calculations and analyses in this thesis were performed mainly through computer tools such as *MATLAB* and *Microsoft Excel*. Both of those programs were used for extensive data analysis.

3.1 Environmental Conditions

3.1.1 Regular Waves

During this study, several sets of environmental conditions were examined. In the regular wave study, 22 different wave periods T , five wave steepnesses S , two water depths ($d = 27\text{ m}$ and $d = 33\text{ m}$), and two monopile diameters ($D = 9\text{ m}$ and $D = 11\text{ m}$) were provided as the input. Testing the three sorts of wave kinematics and using diverse load-calculation methods resulted in more than 3000 simulations. All the investigated periods lay between $T = 6\text{ s}$ and $T = 16.5\text{ s}$, with a step of $\Delta T = 0.5\text{ s}$. The periods are listed in Table 2.

Table 2: Wave Periods

Wave Period	Value in [s]
T ₁	6.0
T ₂	6.5
T ₃	7.0
...	...
T ₁₇	14.0
...	...
T ₂₂	16.5

For each wave period, five wave steepnesses ranging between $S = 1/20$ and $S = 1/40$ were included, as shown in Table 3.

Table 3: Wave Steepnesses

Wave Steepness	Value in [-]
S ₁	1/20
S ₂	1/22
S ₃	1/25
S ₄	1/30
S ₅	1/40

3.1.2 Irregular Waves

According to the plans of the WAS-XL project, OWT should be placed roughly in the middle of the North Sea [33]. The JONSWAP spectrum could be therefore an optimal spectrum for describing the irregular wave characteristics.

As mentioned in the previous chapter, wave and wind conditions are correlated because waves are typically wind-generated. This correlation is usually described in the form of environmental contours. Based on a 50-year contour (Figure 10), six sea states were selected for this study. They were described in terms of significant wave height H_s and peak period T_p . Reductions in H_s were made for two sea states to move them out from the breaking limits; the breaking effect is not captured well by extrapolation from the hindcast. Most of the sea states were correlated with the wind speed $U_w = 25 \text{ m/s}$. The average steepness S was thus selected to be below the criterion of $S_c = 0.059$ [11]. Furthermore, the average Ursell numbers U_r were below the classical validity limit of second-order waves, $U_r = 0.33$ [7].

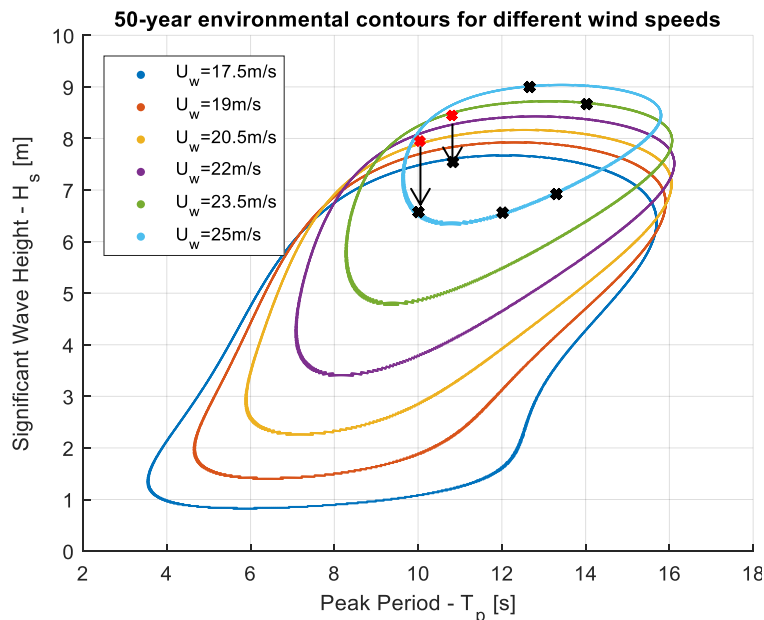


Figure 10: 50-year environmental contours for different wind speeds [33]

All relevant irregular wave characteristics are shown in Table 4. They represented the storm condition. For a cleaner representation of the sea states in diagrams and for easier traceability, an abbreviation for each sea state was introduced. Their names were selected to provide essential information about the sea state. Thus, “I” stands for irregular waves, “H” indicates significant wave height, “T” means peak wave period, and “G” refers to gamma.

Table 4: Irregular sea state characteristics

Irregular Sea State Abbreviation	H_s [m]	T_p [s]	Gamma [-]
IH6.7T10G3.7	6.7	10.0	3.7
IH7.6T11G3.2	7.6	11.0	3.2
IH6.5T12G1.4	6.5	12.0	1.4
IH9T12.5G2.6	9.0	12.5	2.6
IH6.8T13.2G1	6.8	13.2	1.0
IH8.6T14G1.3	8.6	14.0	1.3

3.2 Regular Wave Analysis

Before calculating the wave loads of regular waves, it is crucial to determine whereabouts in the diagram of applicability (Figure 5) the investigated wave conditions reside. This enables optimal selection of the best wave theory. In Figure 11, red and green circles represent the boundaries of the investigated wave conditions that were calculated according to the formulas given at the abscissa and ordinate of the figure. The upper two rows of circles represent the highest steepness $S = 1/20$ and the two lower rows show the lowest $S = 1/40$. The remaining three steepnesses were spread between those two values. Red circles indicate the water depth $d = 27\text{ m}$ and green indicates $d = 33\text{ m}$. Most of the wave conditions were classified as suited to for the second and third Stokes wave theories. These could also be directly described with the fifth Stokes wave theory for possible higher accuracy. Several wave conditions having high periods and high wave heights should be represented with the fifth-order stream function theory or with cnoidal theory. However, in the scope of this thesis, all wave conditions were calculated using the Stokes theories. Linear wave theory was used as the first step of the calculation, followed by the second Stokes wave theory and eventually the fifth Stokes theory. None of the wave conditions exceeded the breaking criterion.

It was noted that most of the wave conditions lay in the field of relative intermediate-depth waves; in a few cases, they lay in the relative deep-water waves. Nevertheless, all calculations in this thesis were performed for intermediate depth waves, because they are valid for all regions.

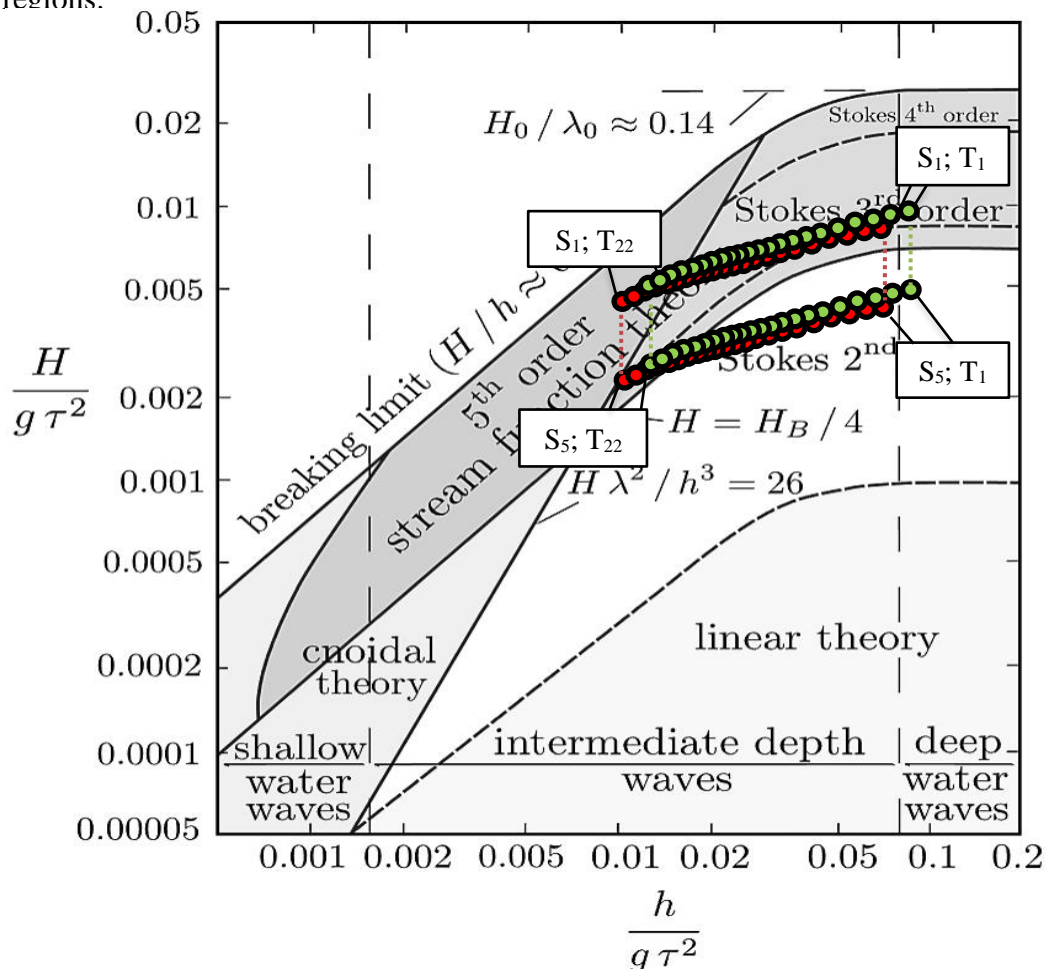


Figure 11: Validity region of investigated sea states for two water depths, modified [36]

The best representation of all the tested wave conditions had the wave period $T = 14.0$ s and steepness $S = 1/20$, as this was the most extreme case that was located in the valid range. Even one period higher, $T = 14.5$ s, was beyond the range and the results would have shown strong deviations and thus been inaccurate. In addition to the mentioned representor of all wave conditions, several others were usually also included in a comparison; those cases had the lowest period and lowest steepness. This method enabled conclusions to be drawn regarding all other results, as their behavior was expected to lie between the tested cases. The most interesting wave condition combinations are shown in Table 5. “R” stands for regular waves, “S” for wave steepness, and “T” for wave period.

Table 5: Four selected regular wave conditions

<i>Regular Wave Condition Abbreviation</i>	S [-]	T [s]
RS20T6	1/20	6.0
RS20T14	1/20	14.0
RS40T6	1/40	6.0
RS40T14	1/40	14.0

3.2.1 Wave Number

One of the first challenges was to calculate the wave number, which was needed to obtain the wave length and wave height. In the case of linear and second-order Stokes theory, the linear dispersion relation from Eq. 3 holds. It can be solved by standard numerical methods, such as trial and error, bisection, or Newton’s method. However, the simplest accurate approximation for solving this equation was given by Guo, as follows [34]:

$$k = \frac{\omega^2}{g} \left(1 - e^{-\left(\omega \sqrt{\frac{d}{g}}\right)^{\frac{5}{2}}} \right)^{-\frac{2}{5}} \quad (37)$$

Finding the wave number and wave length in the case of fifth-order Stokes theory was more challenging, because the linear dispersion relation was invalid due to the non-linear effects. As mentioned in the previous chapter, a recommended option is to use an approximation by Chang [18]. In this method, several empirical parameters must still be calculated, but the results are more convenient than numerical calculations for engineering purposes. The accuracy of this method was tested in this thesis.

3.2.2 Wave Elevation

After the wave number was obtained, the wave elevations of the Stokes waves were calculated and examined. Figure 12 shows the wave conditions RS20T6 and RS20T14, with two wave kinematics. In the left part of the figure, the total wave elevations of the second-order Stokes wave are shown together with first and higher-order harmonics. Among lower wave periods in RS20T6 (Figure 12, top left panel), the first-order wave dominated. However, the second-order was also present and marginally influenced the overall form of the wave. It should be noted that the first-order harmonic has the same amplitude and form as an airy wave. Thus, the airy waves are not presented separately in the following comparisons.

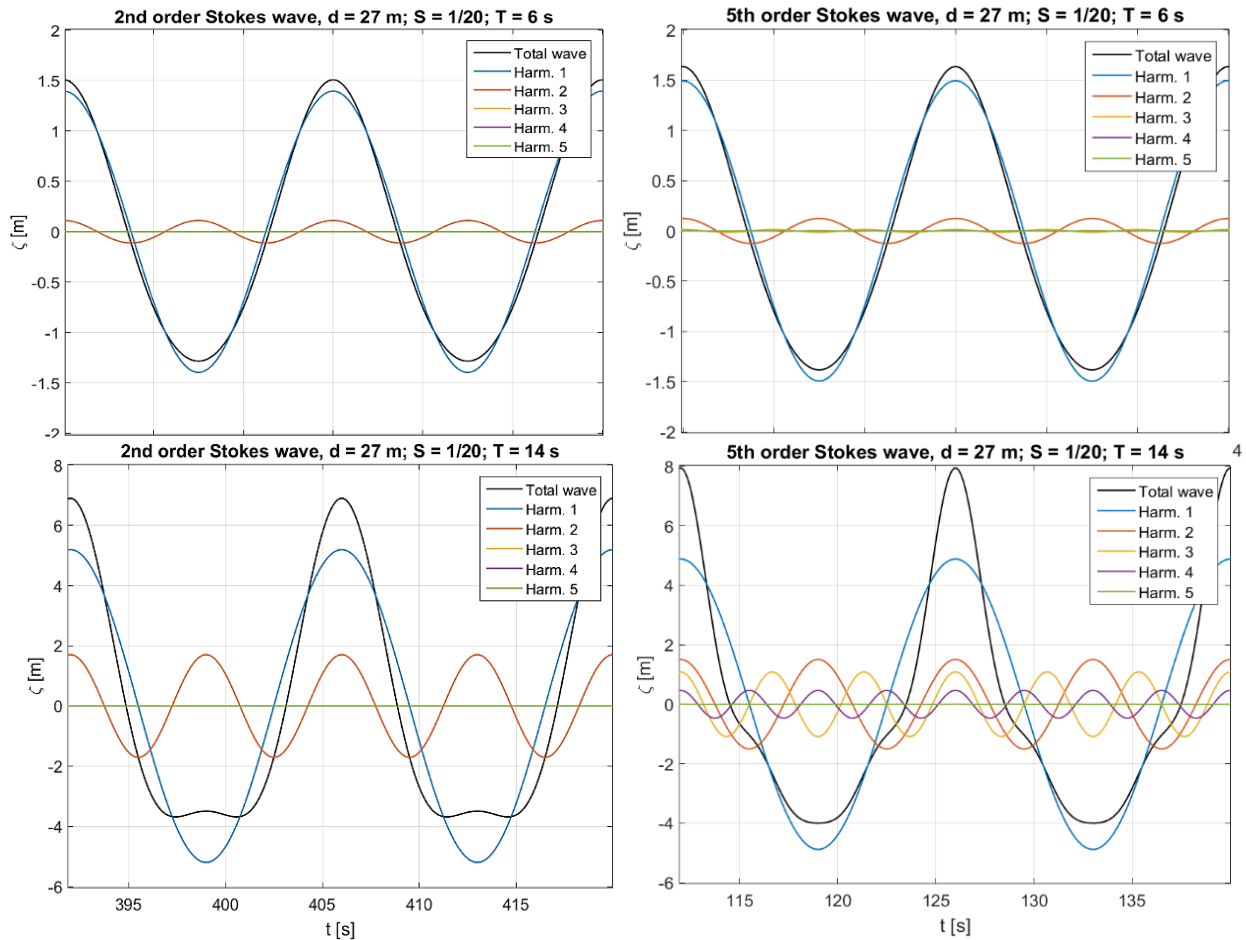


Figure 12: Calculated elevation of four types of Stokes waves

Using fifth-order wave theory (Figure 12, top right panel), the identical wave form was observed. However, it was noted that the amplitude of first-order waves was slightly higher here, as a result of using different approximations of the wave number. With an increase of wave period, the influence of higher-order effects arises. Using the second-order Stokes theory for the representative wave RS20T14, it was not possible to capture the effects of orders higher than second (Figure 12, lower left panel). Furthermore, a slight “bump” in the trough of the wave was observed, because this wave condition was on the border of the validity range. The crest of the fifth-order Stokes waves (Figure 12, lower right panel) was steeper and the trough was shallower. This pattern resulted from higher-order harmonics. A similar tendency was noted when increasing the wave steepness.

Lastly, the impact of increased water depth on the wave form was examined. Figure 13

illustrates two wave conditions, RS20T6 and RS20T14, at a water depth $d = 33\text{ m}$ with different wave periods, using the fifth-order Stokes theory. They are directly comparable with the right-side panels in Figure 12. It is evident that wave amplitudes did not change significantly, especially with lower wave periods. However, when the wave period increased in deeper water, the increase in wave amplitude was less prominent than it was for shallower water ($d = 27\text{ m}$). This difference was caused mainly by the mitigated influence of higher-order harmonics in deeper water.

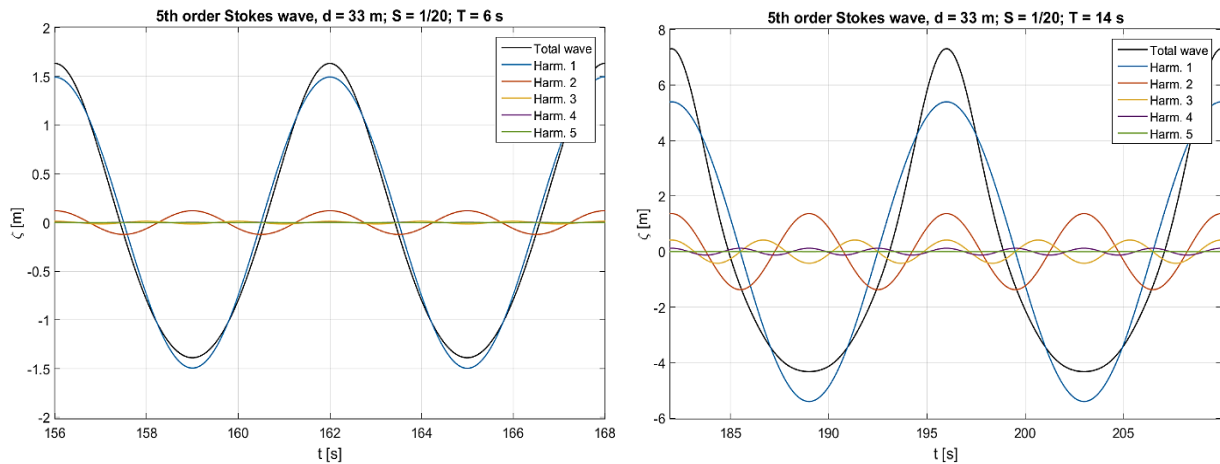


Figure 13: Two wave conditions at water depth $d = 33\text{ m}$

3.2.3 Wave Load

After obtaining an initial impression of how wave elevations behaved under diverse wave conditions, the next step was to examine the loads that acted on the pile. To achieve this, the load distribution over time, frequency, and water depth for all wave conditions was calculated. Thus, several terms were introduced to describe the investigated load form. “Total load” stands for load that resulted from addition of the first-order effect with the higher-order effects. “Global load” refers to load that were obtained by the integration from the seabed to the free surface level. “Maximum load” indicates highest observable load in a time-series.

A quick check regarding the hydrodynamic transparency of the structure if $D < 0.2 \cdot L$ showed that the condition held for all wave conditions, even the larger pile diameter $D = 11\text{ m}$. In the most extreme scenario with the shortest wave length, the ratio $D/L = 0.1973$ remained below the limit of $D/L = 0.2$. That being said, diffraction effects were assumed to be negligible in the first order and the Morison equation is expected to deliver satisfactory results. An extension of the Morison equation to the MacCamy-Fuchs equation in the first order did not yield more realistic results. The force development was analyzed, and no significant difference was noted between the two methods (see Appendix, Figures 48 and 49).

To calculate the force distribution over the pile length, it was necessary first to find the horizontal wave kinematics using the equations presented in the second chapter. The kinematics included the horizontal particle velocity u and horizontal particle acceleration a . In addition, the vertical particle velocity w was needed for the Rainey equation and the FNV equation. Depending on which wave theory was used, different integration methods were used. For airy waves, constant stretching was applied, as shown in Figure 1. For nonlinear waves, the

integration of wave kinematics was performed up to the exact position of wave elevation. An example of nonlinear wave kinematic distribution over water depth, and for the whole time-step, is shown in Figure 14.

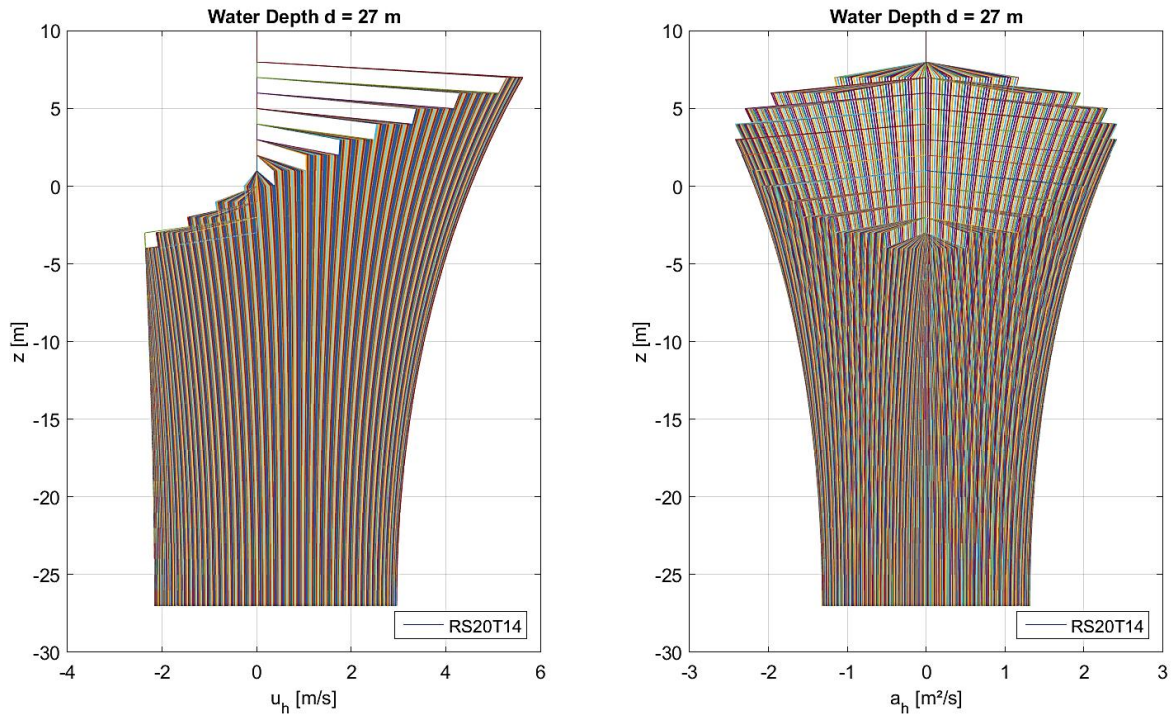


Figure 14: Horizontal wave particle velocities and accelerations over z for the whole time-step (second-order Stokes kinematics, $D = 9$ m)

After the distribution of horizontal wave kinematics had been calculated correctly, it was straightforward to obtain the inertial and drag forces for the Morison equation. In addition, axial divergence correction and the surface intersection point force for the Rainey equation and FNV equation were derived. A selection of the optimal coefficients for these equations was also needed; these depend generally on many factors, which differ for each wave condition. However, for simplicity, a reasonable assumption for the added mass coefficient is $C_m = 2$, whereas the drag coefficient is assumed to be $C_d = 0.9$. These values are assumed to be constant for all wave conditions. Furthermore, to check which forces that act on a structure are dominant, DNV recommends referring to the diagram shown in Figure 15.

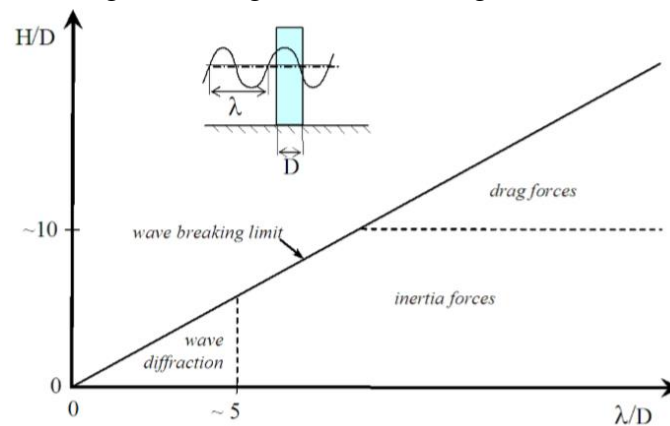


Figure 15: Relative importance of inertia, drag and diffraction wave forces [22]

Although the loads in this thesis were inertia-dominated, in some wave conditions the viscous drag term is high enough to influence the total force. In other words, they both contribute to the

total force. Figure 16 shows the force terms over time at SWL. When the wave is not striking the structure in this section of the length, the total force is $F_{total} = 0$. The red line represents the inertial force and the blue dashed line shows the drag force. In the upper panel of the figure, the wave condition RS20T6 is illustrated. There, the total force is almost unaffected by the drag force. In the lower panel (RS20T14), the drag term rises and shapes the form of total force.

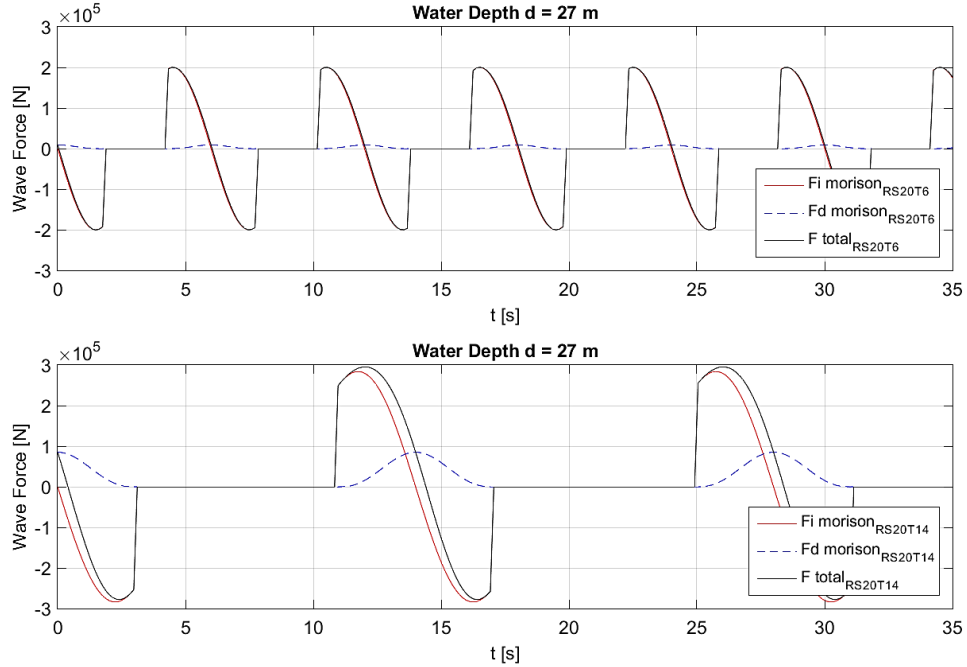


Figure 16: Time series of the total wave forces at SWL for two wave conditions using Morison equation with second-order kinematics ($D = 9$ m)

An increase in the wave period or steepness is directly proportional to an increase in either the drag or inertial forces. In a wave condition example of the second-order Stokes wave, this tendency is observable (Figure 17). Red lines represent the inertia force and blue lines the drag force.

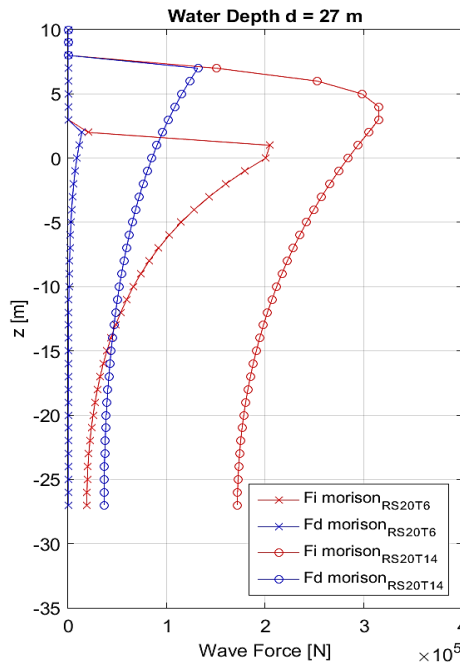


Figure 17: Total and maximum inertial and drag force distribution for two wave conditions using Morison equation with second-order kinematics ($D = 9$ m)

In addition to inertia and drag forces, it was necessary to find the axial divergence force and point forces for the Rainey and FNV equations. Then the total forces for each length segment of the pile could be calculated. Figure 18 shows a distribution of the total force in the case of the Morison equation using second-order Stokes wave theory, for four different wave conditions in two water depths. Several important conclusions or observations can be derived from this graph. First, and again, with an increase in wave period or steepness, the total force rises. With an increase in steepness, the distance that water molecules must travel to compensate for a wave period grows. This leads to higher horizontal particle kinematics and thus higher loads.

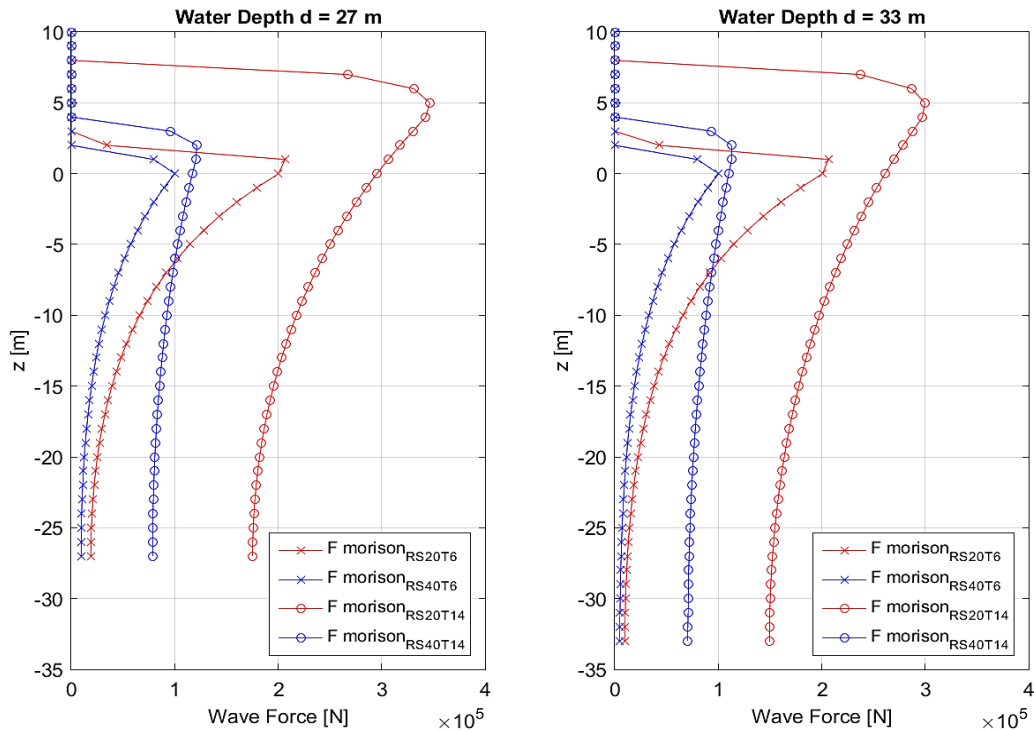


Figure 18: Total and maximum force distribution over structure length using Morison equation with the second order Stokes wave kinematics ($D = 9$ m)

Second, wave conditions with shorter wave periods tend to increase strongly in force when approaching the water surface and show the steeper curve. Third, the form of the distribution of the total force does not change significantly with a change in water depth, compared at the SWL. An exception is the representative wave condition RS20T14 and wave conditions of higher periods. In water with $d = 27$ m, this wave condition lies on the border of theory validity, which results in an overprediction of the forces. A brief comparison among all calculated and measured force distributions along the length of the structure is given in Chapter 4. The impact of increasing diameter is also discussed in that chapter.

The results clearly indicated that for long waves (long periods) in shallow water, the Stokes theory should not be used. The theory in that case falls outside the range of validity and the results are grossly incorrect. Additionally, according to Fenton [17], the upper limit for using the fifth Stokes' is $L/d \approx 10$. Above this limit, the viscous flow separation results in significant discrepancies.

3.2.4 Higher Order Loads

Calculating the force distribution and its magnitude with regular waves was an important step in predicting the effects that act on the structure. However, the main usage of regular waves in this thesis lay in determining the presence and impact of higher order terms. This investigation was crucial, since the higher order excitation frequency may coincide with the lowest resonance period of fixed offshore turbines. This could lead to many undesirable responses of the structure and result in its failure.

The nonlinearity of waves and wave forces can be calculated through fast Fourier transform (FFT) of time series into frequency series. If higher order terms are present, their magnitude can easily be found. To obtain the correct amplitudes, the time interval of FFT should be selected to contain the exact number of the period. In the following chapter, the calculated magnitudes of the higher order terms are compared to the measured magnitudes, for all calculation methods.

In Figure 19, wave conditions RS20T6, RS20T14, RS42T6, and RS42T14 for two water depths are compared. Second-order Stokes theory with the Morison equation was used. Although this wave kinematics consists of effects up to the second order, the Morison equation yielded higher-order forces mostly by capturing the nonlinearities around MWL and at higher levels through the integration. The main driver for this behavior was inertial force.

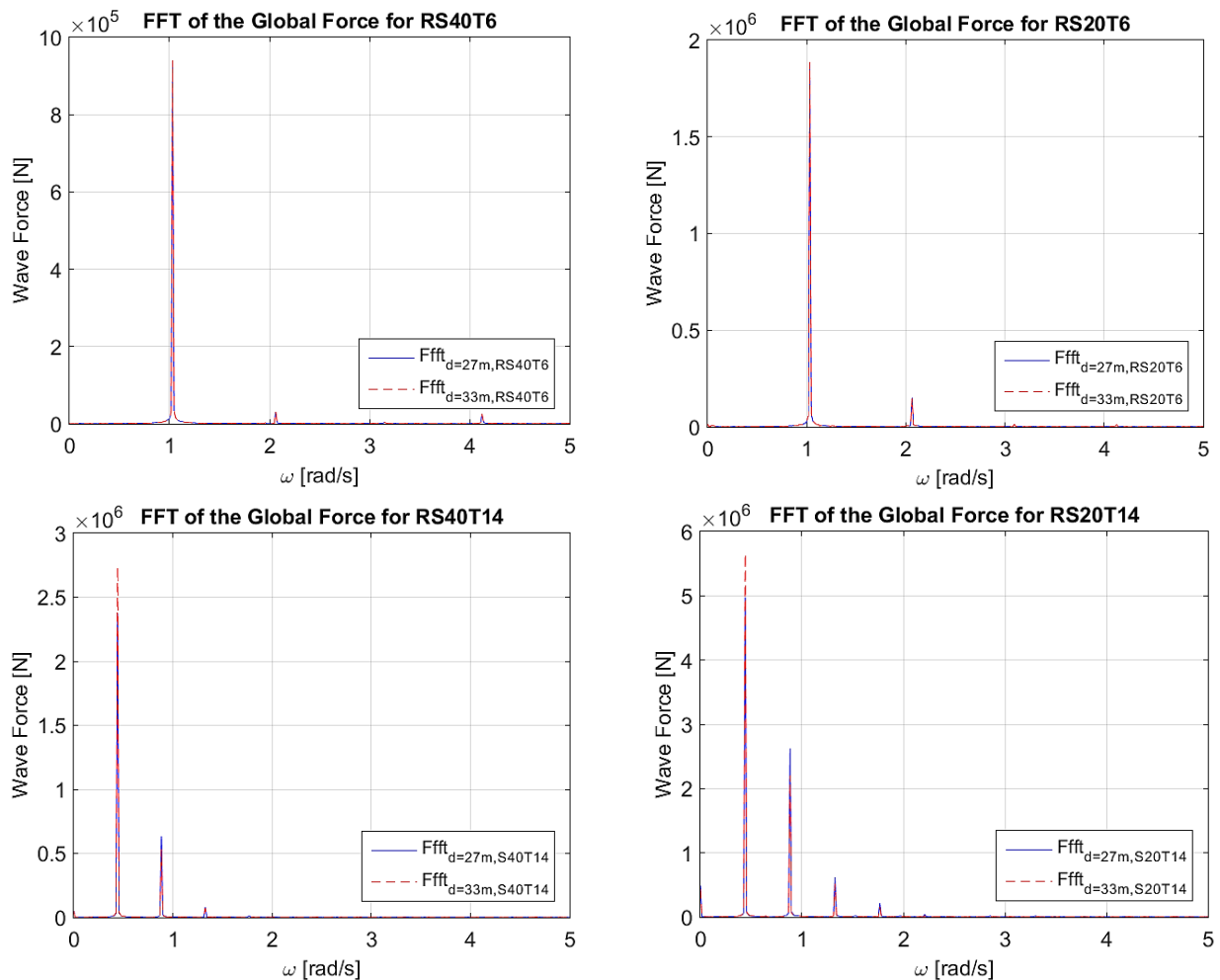


Figure 19: FFT of the global force for four wave conditions in two water depths, using second-order Morison equation ($D = 9$ m)

First, the relative importance of the higher order terms increases with a decrease of water depth. In Figure 19, the blue line always represents a larger magnitude than the dashed red line, for all wave conditions in all higher order terms. In the first-order term, this was not the case; the global force in deeper water was stronger. Thus, the higher order effects were larger for shallow water waves, which implies a larger degree of nonlinearity.

Second, the same trend was observed with an increase of wave steepness and/or wave period. The higher order effects were amplified with an increase in each of these variables. Hence, the maximum higher order terms were observed for the wave condition RS20T14 at the water depth $d = 27\text{ m}$ (Figure 19, lower right panel). The smallest higher order terms were observed for RS40T6 for $d = 33\text{ m}$ (Figure 19, upper left panel). Furthermore, with an increase in pile diameter from $D = 9\text{ m}$ to $D = 11\text{ m}$, only a slight increase in the relative magnitude of higher order effects was noted. In this example with second-order Stokes theory, it might be even assumed to be negligible. More information appears in the Appendix (Figure 50).

Lastly, the relative magnitude of higher order forces was the greatest at or above MWL. This behavior was expected, since the nonlinearity of the waves was introduced there. This effect decreased with the water depth to the seabed, where the first-order forces dominated. When using linear wave theory with constant stretching to predict the occurring loads, the magnitude of the loads was roughly the same as in the first-order load (shown in Figure 19). The theory solely captures the effects occurring up to the MWL, which are linear. Its application would not be critical for the wave condition RS40T6; however, with a slight increase in wave period or steepness, a higher order wave theory must be used to obtain accurate results.

3.3 Irregular Wave Analysis

A first step in analyzing the irregular waves was an additional check whether the JONSWAP spectrum was a reasonable model for the given sea states. That is the case when $3.6 < T_P/\sqrt{H_S} < 5$ is valid [11]. Only the sea state IH6.8T13.2G1 did not meet the criterion precisely, since $T_P/\sqrt{H_S} = 5.062$. Nevertheless, this sea state was replicated by the JONSWAP spectrum; this must be considered when interpreting the results. Using Eq. 24, it was possible to calculate the JONSWAP spectra for all six irregular sea states. The plotted results are shown in Figure 20.

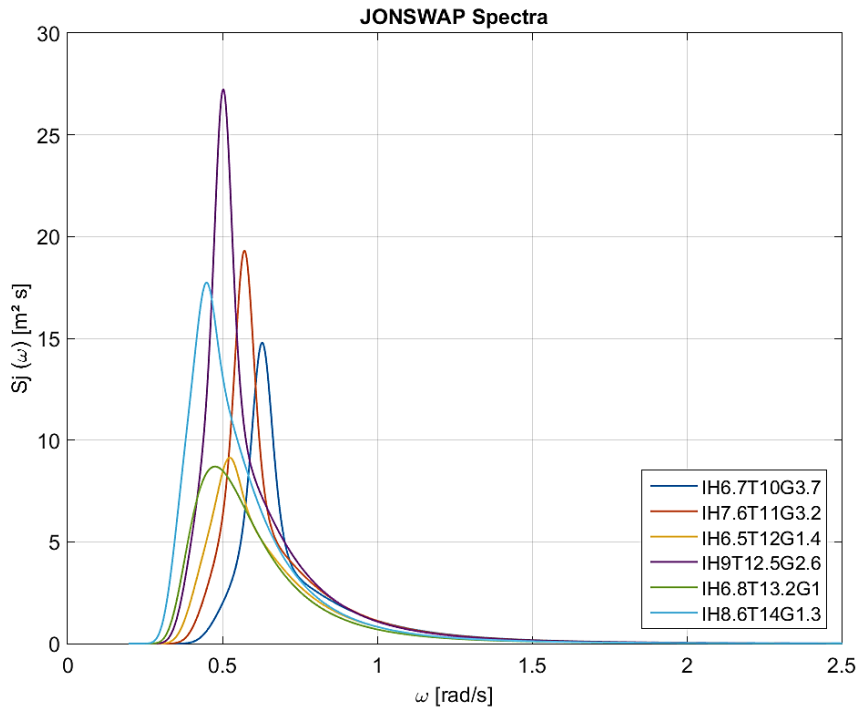


Figure 20: JONSWAP Spectra for all six sea states

Four of the sea states had prominent peaks and were narrow. This result implies that most of the waves in those sea states lay in the range of similar frequency. The sea state IH9T12.5G2.6 had the highest peak of the spectrum $S_j(\omega) = 27.2 \text{ m}^2\text{s}$ at the angular frequency $\omega = 0.5 \text{ rad/s}$. The lowest sea state, IH6.8T13.2G1, had the peak of the spectrum $S_j(\omega) = 8.7 \text{ m}^2\text{s}$ at $\omega = 0.48 \text{ rad/s}$ with a more constant range of wave frequencies in it.

Having the JONSWAP spectrum, the calculation began by converting it back to individual (co)sinusoid waves, using – for example – the inverse FFT (IFFT). From this spectrum and its energy density, it was possible to derive the amplitude and frequency of (co)sinusoids. The total number of regular waves n added to make an irregular wave should be enough to avoid repetition of the irregular wave. This value was selected to be $n = 3000$ for a 3-hour test. The sum of all the (co)sinusoid waves resulted in the total surface elevation at each point of time. An example of total wave elevations for all sea states is shown in Figure 21. For this 3-hour surface process, the maximum amplitude of $\zeta_a = 8.86 \text{ m}$ was found in the sea state IH9T12.5G2.6 in the time position of $t = 4041 \text{ s}$. It should be noted that the data change each time the program runs, due to random alternation of the phase angle and therefore the frequency.

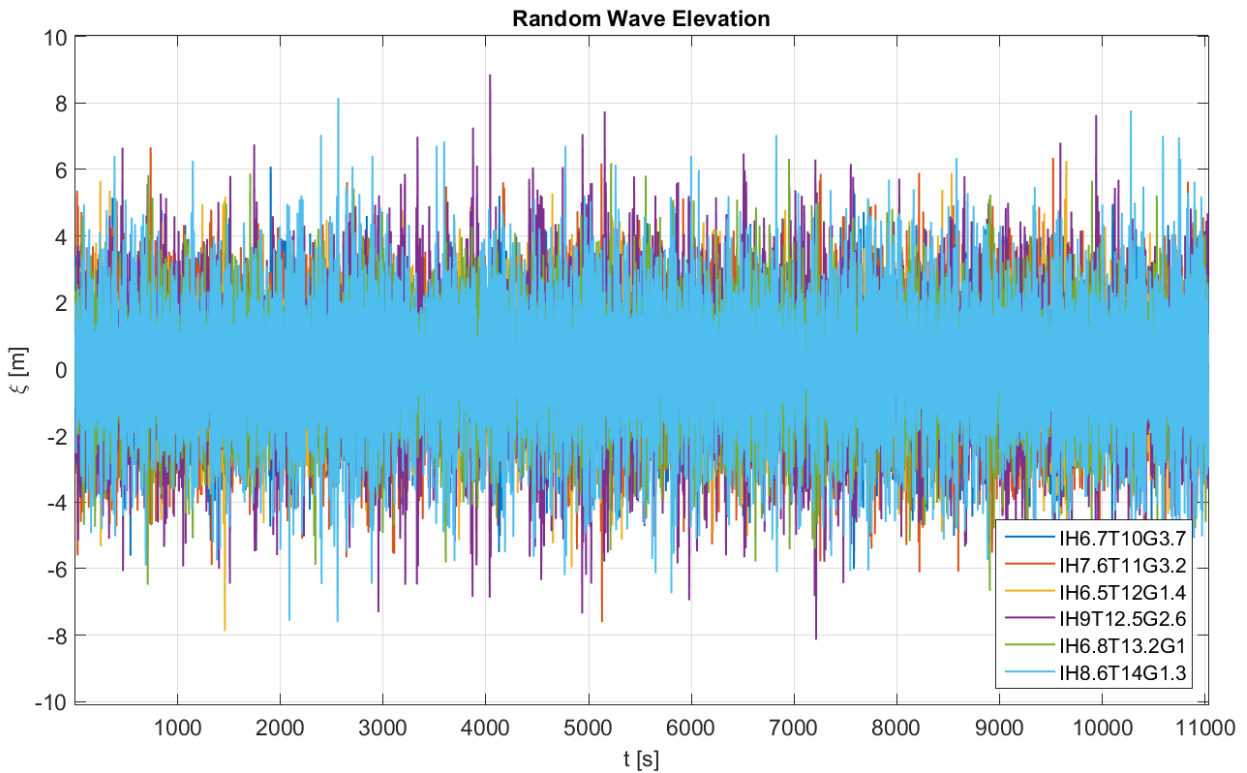


Figure 21: Wave elevations over 3-hour time

Using linear wave theory kinematics with constant stretching above MWL and the Morison equation, the loads caused by irregular waves were calculated. For all sea states, the inertial force was dominant. During the same time, when the wave with the highest amplitude hit the structure, the maximum global force $F_{max} = 1.06 \cdot 10^7 N$ was observed in Figure 22. It was clear that the global forces during the irregular wave process were significantly higher than in regular waves, and were not directly comparable with that field.

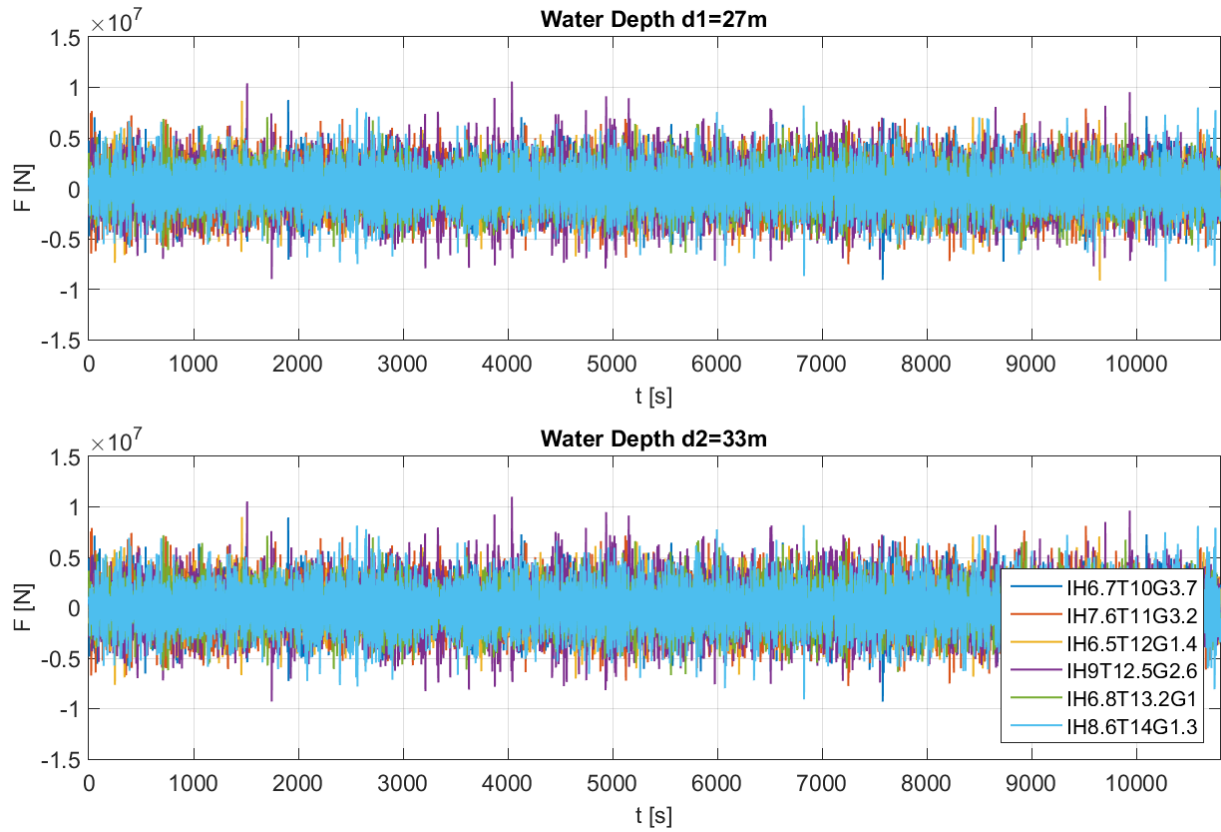


Figure 22: Global force development over 3-hour time for two water depths ($D = 9$ m)

Lastly, to verify the *MATLAB* script used, the control of significant wave height H_s is recommended. The values of the input of H_s should be close to the output H_s . The output of significant wave height (H_s) was calculated as follows:

$$H_s = 4 \sqrt{\sum_{n=1}^N S_j(\omega) \cdot \Delta\omega} \quad (38)$$

The maximum deviation between the input and output of wave heights (H_s) was always less than 3% and was thus assumed to be accurate.

3.4 Conclusions

In the analysis of regular waves, several general observations were noted. As expected, the linear wave theory was unable to accurately predict the effects that occurred in most of the investigated wave conditions. The reason was that the theory ignores the higher order effects, which played a crucial role in this study. Those effects were amplified during longer wave periods, at higher steepness, or in lower water depths. For the wave conditions outside of the range of validity, the Stokes kinematics was strongly inaccurate. Using the approximation formula for the wave number, a minor overprediction of the effects in the fifth-order Stokes kinematics was found for all wave conditions. This finding applied mainly to the wave elevation and wave force amplitudes of the first order, since they should not differ. The largest discrepancy for the first-order amplitude between the two kinematic approximations was about 6%.

The structure is mainly exposed to inertial forces, which are a main driver for the higher order loads that occur. However, the influence of the drag force expanded during the longer wave periods, and must be considered. Generally, nonlinearity effects were amplified with an increase in structural diameter, steepness, or wave period. These effects were the greatest at or above MWL.

Because the slender structure requirement $D/L < 0.2$ was valid for all wave lengths and both diameters, the first-order diffraction was irrelevant in this study. This point was validated through comparing the inertia terms using the Morison equation and the MacCamy-Fuchs equation. No significant differences in wave loads were found.

Initial investigations of the irregular waves predicted that the JONSWAP spectrum might be a good choice to represent the real sea state conditions. In the next chapter, a comparison to the measured waves, using first-order kinematics, is provided. Thereafter, more precise predictions are given.

4 Validation using Model Test Measurements

The objective of the model testing, which was carried out by SINTEF Ocean and NTNU, was to provide data to validate the calculated loads. In this chapter, their experimental setup of the model is described, and the measurements thus obtained are reported. These results are then compared to the calculated results derived from theory, in the same order as in the previous chapter. Certain calculated results that were not presented in the last chapter are introduced for comparison purposes.

4.1 Experimental Setup

The model was tested in a medium-sized wave flume at NTNU/SINTEF Ocean, Trondheim. The flume set-up, from a bird's-eye view and the side view, is illustrated schematically in Figure 23. The tank was 28 m long, 2.5 m wide, and allowed for a maximum water depth of 1 m.

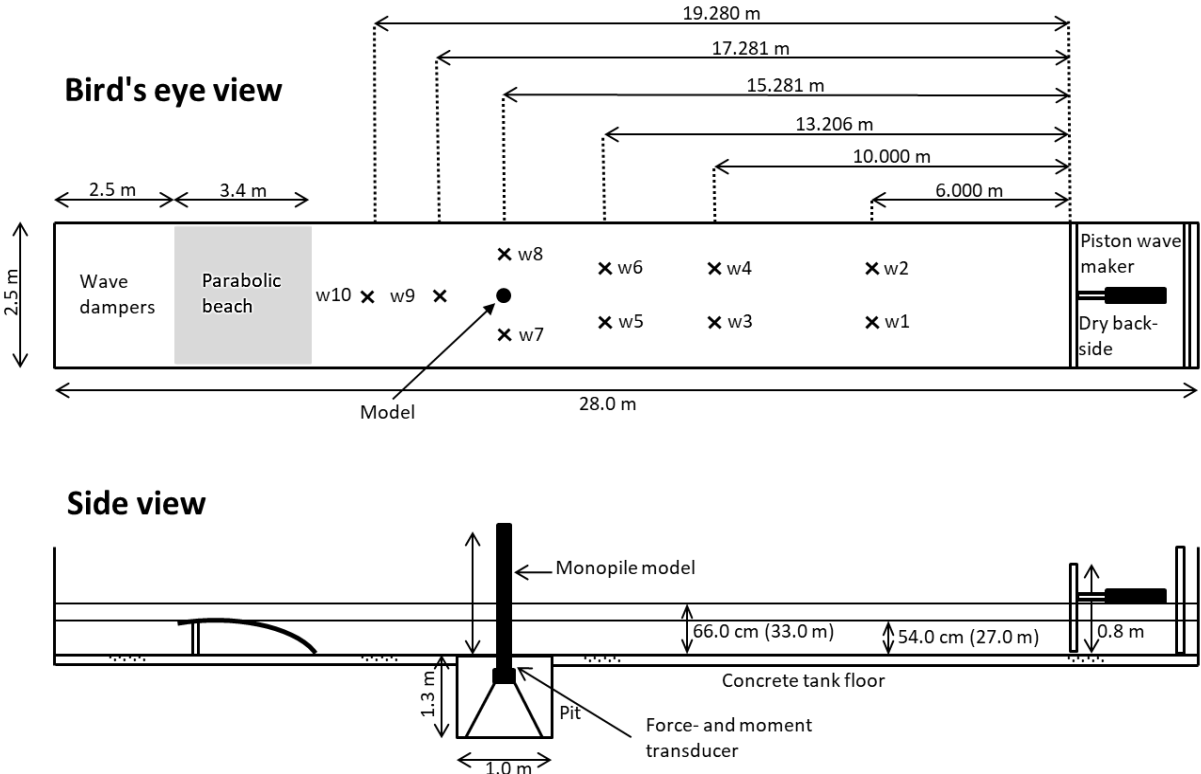


Figure 23: Model test set-up

The first important component is the piston wave-maker, which generates waves through a translational piston-board motion to one side of the flume. Its motion was measured and saved during the tests to check repeatability and to verify the correspondence of the wave calibration and model tests. The piston wave-maker was driven by an electric actuator located

approximately 60 cm above the tank floor.

Another obligatory component at the end of the flume is the bottom-fixed parabolic beach. Its purpose is to absorb the waves and prevent reflection, which could influence the flow acting on the monopile model. To achieve the maximum absorption, the wave height was adjusted to be slightly (1.5 cm) above the still water level, for each water depth. The porosity level of the parabolic beach plates was 4%. Nonetheless, some reflection based on the wave period was inevitable.

Before the forces and moment of the models were tested, the wave elevation tests were performed. Eleven capacitance wave gauges were utilized for this purpose, positioned in the wave tank in the order shown in Figure 10. Instead of the model in this testing phase, the eleventh gauge was placed at the same position. The gauges were linearly calibrated for each water depth. During the tests, the lower points of the wave gauges were placed 15 cm and 30 cm above the tank floor, respectively.

Two stiff monopile models with different set-ups were investigated. The first model had a diameter $D = 0.18 \text{ m}$ (9 m full-scale) and the second model was $D = 0.22 \text{ m}$ (11 m full-scale). Both models were placed 15.26 m from the wave-maker, as shown in Figure 24. At the bottom, they were simply fixed to the ground in the pit with a crossbar stiffener, and connected to the force/moment transducers to provide measurements. To cover the pit, a transparent acrylic glass was used. In the first model, in addition to measuring the global loads, it was instrumented with 11 sections along the pile to measure the force distribution (Figure 25). One force transducer was placed in front of and one after the inner core, which addition led to the total force acting on the length segment. The complete inner portion was surrounded by plastic outer shells, which also prevented inner sloshing.

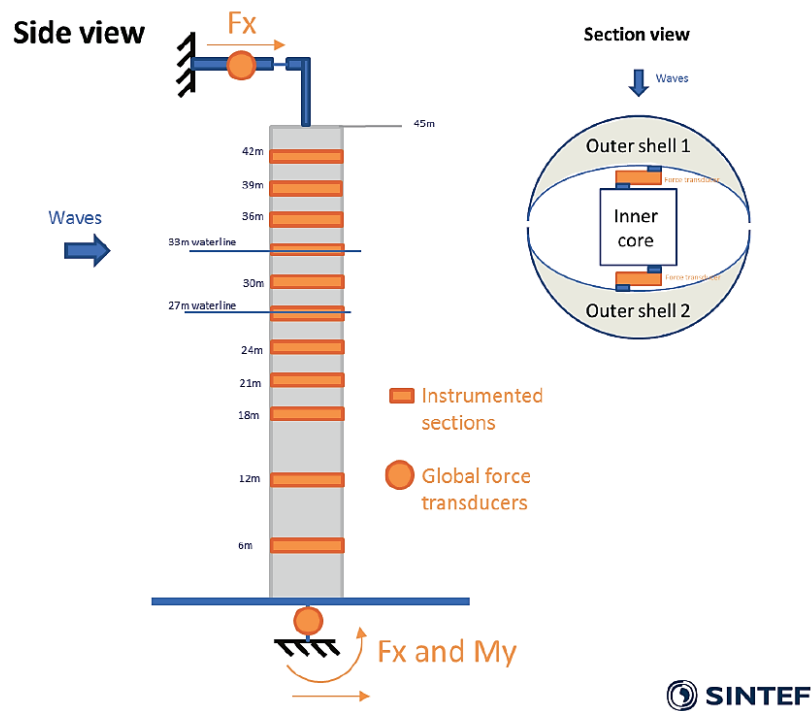


Figure 24: Monopile set-up [33]

The composition of the second model, with a larger diameter, was the same but simpler as it was not equipped with sectional measurements. To prevent sloshing, the inner part was filled with a form of sponge foam.

4.2 Principles of Model Testing

Three conditions of similarity needed to be met to achieve the same behavior of the model compared to the full-scale structure. These were geometrical similarity, kinematic similarity, and dynamic similarity. Geometrical similarity requires that both structures have the same shape and all linear dimensions have the same scale ratio $L_M = \lambda L_F$, where λ represents the length scale ratio, F denotes full-scale and M denotes model. Kinematic similarity represents the similarity of velocities and accelerations. Dynamic similarity refers to the force similarity.

The accuracy of the test data increases with model size, but so do the costs of trials. Increased size leads additionally to higher and undesirable interaction with the wave-tank walls and the capacity of the wave-maker must also be considered. A compromise was needed, and for the purposes of the WAS XL project, the length scale ratio was selected to be $\lambda = 50$.

In maritime applications, two main non-dimensional numbers are used to describe the compliance of effects of the model compared to the full-scale structure. These are:

- *Froude number*, which gives the ratio between inertia and gravity forces

$$F_N = \frac{u_M^2}{g \cdot D_M} = \frac{u_F^2}{g \cdot D_F} \quad (39)$$

- *Reynold number*, which gives the ratio between inertia and viscous forces

$$Re = \frac{u_M \cdot D_M}{\nu} = \frac{u_F \cdot D_F}{\nu} \quad (40)$$

where ν represents the kinematic viscosity of the fluid and u represents the flow velocity. Because the preservation of both numbers in a model test is redundant and not realizable, only one scaling is utilized. When OWTs are tested in wave tanks, the requirement of a true scaling of the wave leads to application of the Froude scaling law. The law is based on the effects of gravitational acceleration, and the scaling is defined by the preservation of the *Froude number*. That means the model and full-scale accelerations are equal [11]. Table 6 shows the Froude scaling, including the multiplication factors for relevant physical parameters. The difference in water density between water in the wave tank and the denser (salty) water in the sea is relevant for the force and moments, and should be considered.

Table 6: Froude Scaling Table

<i>Physical Parameter</i>	<i>Unit</i>	<i>Multiplication factor</i>
Wave Height	[m]	λ
Length	[m]	λ
Force	[N]	$\lambda^3 \frac{\rho_F}{\rho_M}$
Moment	[Nm]	$\lambda^4 \frac{\rho_F}{\rho_M}$
Velocity	[m/s]	$\sqrt{\lambda}$
Acceleration	[m/s ²]	1
Time	[s]	$\sqrt{\lambda}$

As previously mentioned, Froude scaling does not preserve the *Reynolds number*, which is significantly smaller in a model than at full scale. This difference is due to the much lower flow velocity in the model tank. The larger the scale ratio, the larger the discrepancy in the *Reynolds number* between the model and full-scale structure [31]:

$$Re_F = \lambda^{\frac{3}{2}} \cdot Re_M. \quad (41)$$

In the case of scale factor $\lambda = 50$, the Re of the full-scale structure is 353 times higher. The result is that the flow regime of the full-scale structure is completely turbulent ($Re_F > 10^6$), whereas the flow regime of the model is likely to be laminar ($Re_F < 10^5$). The lower *Reynolds number* also leads to higher drag coefficients, c_d [31].

A common practice is to try to obtain the highest possible *Reynolds number* in a model to realistically represent the viscous effects. To achieve this, a high surface roughness is introduced to compensate for the difference in scale. A higher surface roughness decrease and stabilize the drag coefficients, thus creating values closer to the full-scale structure. Figure 25 shows the applied surface, consisting of numerous hemispheres with a radius of $r = 2 \text{ mm}$.

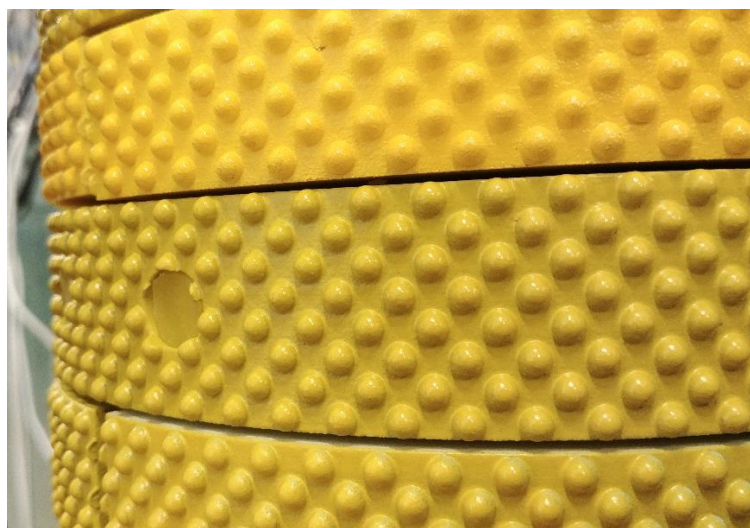


Figure 25: Surface of the Model

4.3 Analysis of the Measured Data

The final step before analyzing the data was to apply a low-pass filter with a cutoff frequency of the natural model-scale structure frequency, which was $f_{nat,m} = 23 \text{ Hz}$. The measured forces were filtered to remove the impact of the response from the pile. Although the structure ought to be rigid, a response might appear as a high-frequency vibration, induced mainly by the wave slamming. All values below the natural structure frequency were therefore kept. This step is important to optimally compare the calculated data with the measured data, as the calculated data consist of a clear (non-noise) shape. The noise is removed with a digital, higher order Butterworth filter, which is a commonly used filter for this kind of application.

4.3.1 Regular Wave Validation

Wave Elevation Comparison

As in Chapter 3, the first step in evaluating the measured data was to scrutinize the wave elevations. The first impression was that the wave form of the measured waves was closest to waves replicated using the fifth-order Stokes theory. Although the wave form for the wave condition RS20T6 looked almost linear (Figure 26, left), the position of MWL was strongly above the SWL. This implied that there might be a centrifugal pump issue, which led to waves that were not properly zeroed. In the case of RS20T6 (Figure 26, right) and all other measured wave conditions, a similar tendency was observable. This led to a tentative conclusion that the waves in a wave tank are more challenging to reconstruct than to calculate. Because the amplitude of the measured waves differed from the calculated amplitudes, a certain deviation in the load comparison was expected.

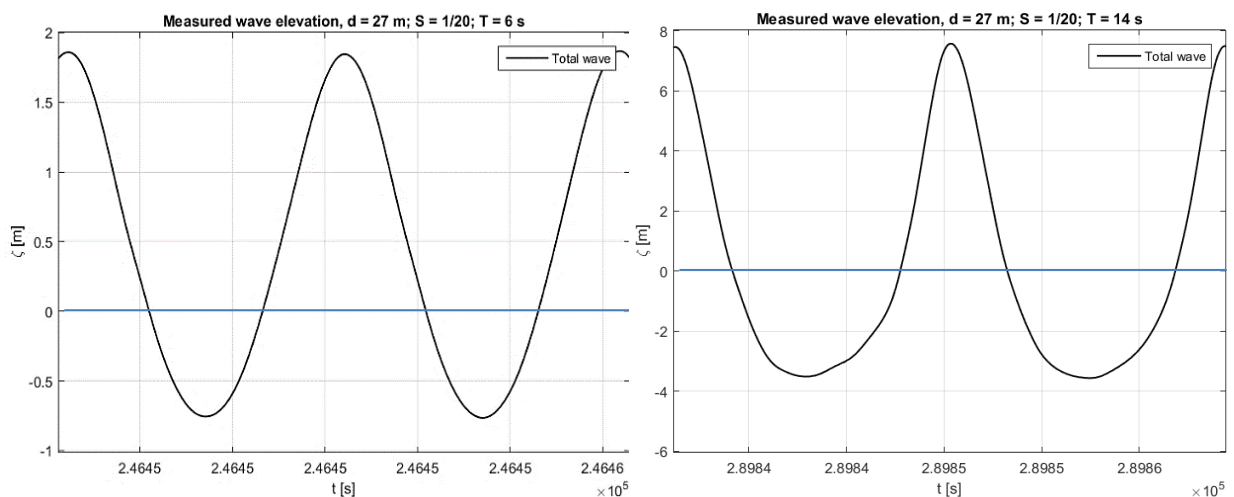


Figure 26: Measured wave elevation for two wave conditions

Comparison of the Maximum Total Force Distribution

The first model with the diameter $D = 0.18 \text{ m}$ (9 m full-scale) was equipped with sections along the structure length to measure the distributed forces. This enabled a direct comparison with the calculated distribution of the total force amplitude acting on each length-segment. Figure 27 shows the first comparison of the maximum and normalized force distribution up to the SWL for the wave condition RS20T6. The first impression is that the measured forces in all sections were meaningfully lower than the calculated forces. All the calculation methods gave similar results; particularly the methods that use same wave kinematics had identical results. The highest discrepancy between a measured and a calculated result was about 80%, observed at the length segment at $z = -12 \text{ m}$. It should be noted that the forces were normalized by setting the maximum occurring value in the investigated condition to 1.0. The results of FNV theory are not presented here because other theories provided more transparent results. The FNV results did not differ from the fifth Rainey theory, except at the SWL, where FNV showed significantly higher loads.

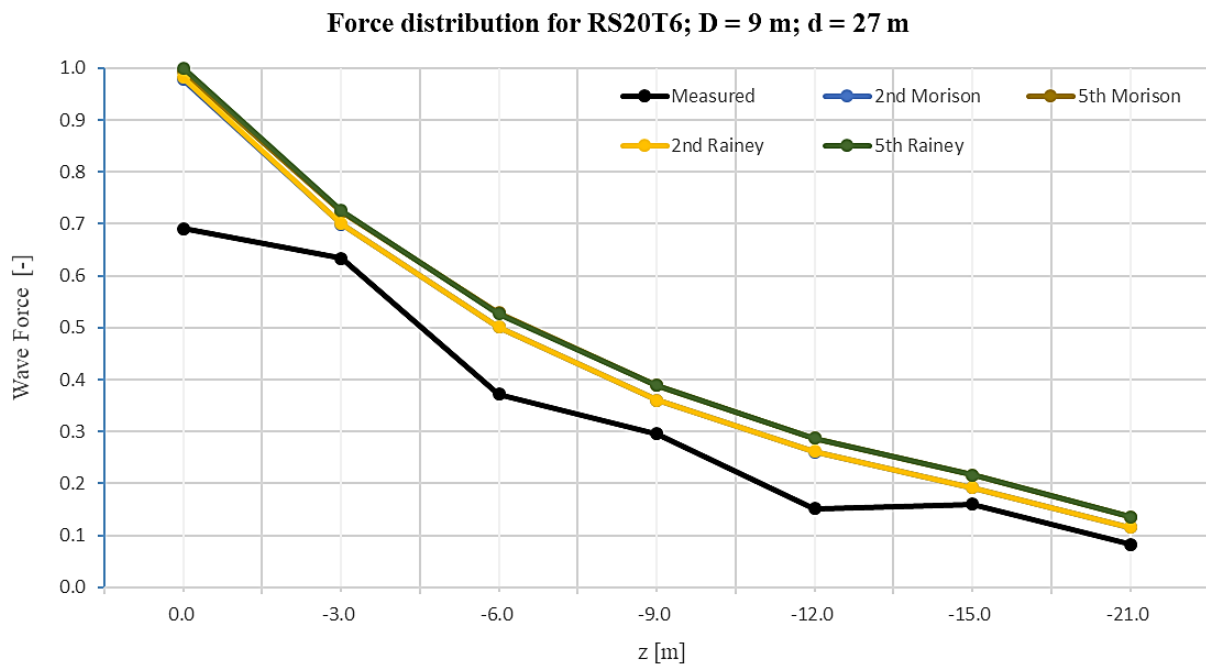


Figure 27: Comparison of the total force distribution over the length of structure, RS20T6

To draw an accurate conclusion, an additional comparison was needed for the wave condition RS20T14 of the higher wave period. Figure 28 shows that the force distribution yielded different results. The measured forces were closer to the calculated forces in this case. However, the values of calculated forces were spread more widely. This deviation is prominent in Figure 28, as the minimum value of the axis was set to 0.4 (not to 0.0 as in Figure 27). The lowest average deviation, 5%, between the measured and calculated values was obtained from the Morison equation using fifth-order Stokes theory. The largest discrepancy was obtained with the second-order Rainey theory.

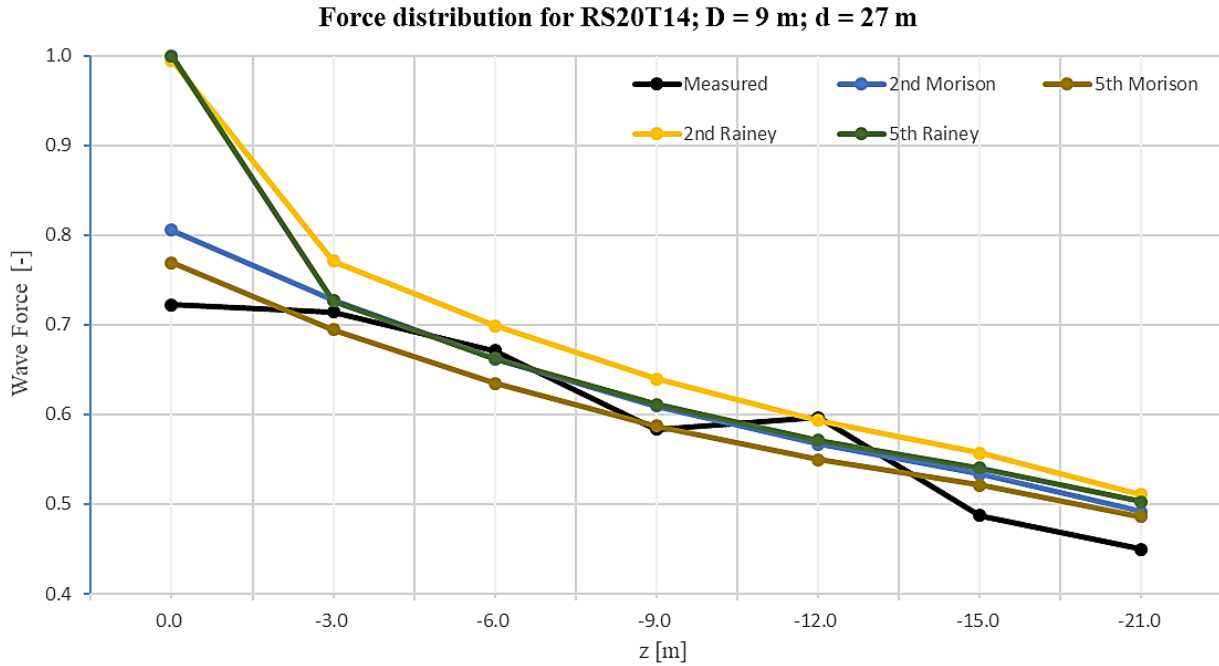


Figure 28: Comparison of the total distribution over the length of structure, RS20T14

The force between $z = -3\text{ m}$ and SWL should increase substantially more than it did. At $z = -12\text{ m}$, the force showed too large a discrepancy between RS20T6 and RS20T14, which was surprising. This pattern was even more noticeable in the case of deeper water ($d = 33\text{ m}$) (see Appendix, Figure 51). It seems that the force sensors at $z = -12\text{ m}$ and at SWL were not precise enough. A check on experimental data regarding this issue showed that the behavior held for all wave conditions; in some more and in some less prominent. The inaccurate force distribution is validated through the existing zigzag-form instead of parabolic form. Moreover, some sensors were not zeroed precisely that led to an additional error.

Maximum Total & Global Load Comparison

A comparison of the maximum global force acting on the structure can be optimally presented by plotting it for each wave period. The greatest global loads for each wave condition were identified, and the largest maxima were selected and utilized in a comparative study of numerical load models versus the measured loads. For $D = 9\text{ m}$, $d = 27\text{ m}$, and $S = 1/20$, the results are shown in Figure 29. In most cases, the second-order Stokes theory with Morison calculations showed the least discrepancy relative to the measured forces, along all wave periods but especially from T1 to T9. By contrast, the greatest deviation was found with the fifth-order Stokes theory using FNV force calculation. With a further increase in the wave period, the deviation increased gradually. After T17 (red zone), the Stokes wave theories could not adequately handle growth in the wave period, and the global forces were over- or underestimated. This was expected behavior because such wave conditions fall outside the validity range.

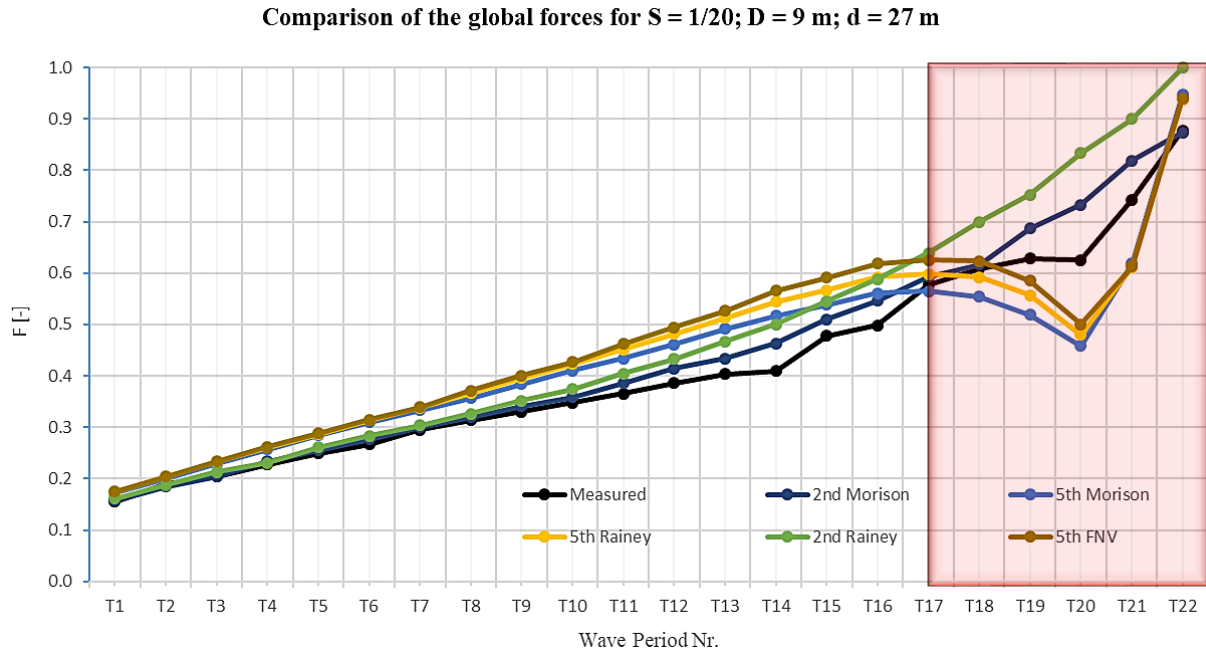


Figure 29: Comparison of highest global forces for all wave periods

Similar trends were noted for other wave steepnesses and water depths. These results appear in the Appendix (Figure 52). However, to additionally validate the measured results, it is recommended to examine the global moments. In Figure 30, moments calculated with the Morison equation are selected for the comparison. The initial impression was that the measured moments are roughly in the same relative relation ($M = F \cdot z$) to the measured values of the forces, which indicates that the sensors for both global force and global moment were accurate.

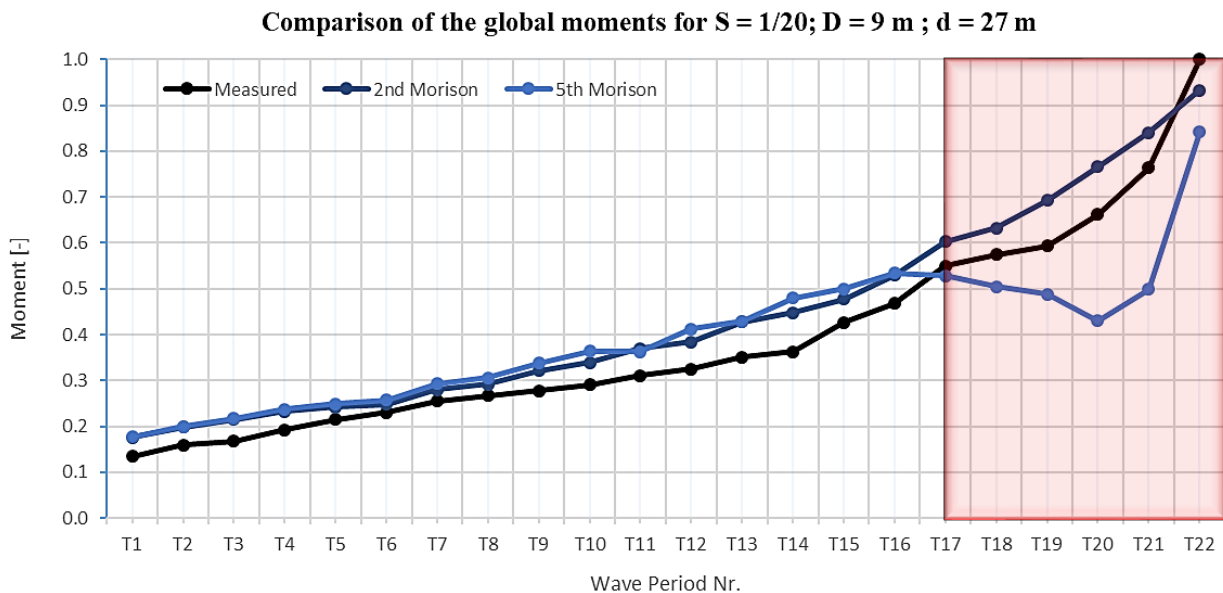


Figure 30: Comparison of highest global moments for all wave periods

Because the structure is exposed mainly to inertial forces, it was expected that the force should increase by roughly 50% (D_1^2 / D_2^2) when using the second pile model ($D = 11$ m). To easily compare the impact of increasing the pile diameter, the relative force (F/D^2) was used. If the forces increase in this pattern, the bar height between the measured and calculated forces

should be roughly the same. If not, the drag term or higher-order diffraction effects are present. This comparison for the steepest wave $S = 1/20$ and water depth $d = 27\text{ m}$, based on the Morison equation using representative second-order Stokes theory, is illustrated in Figure 31.

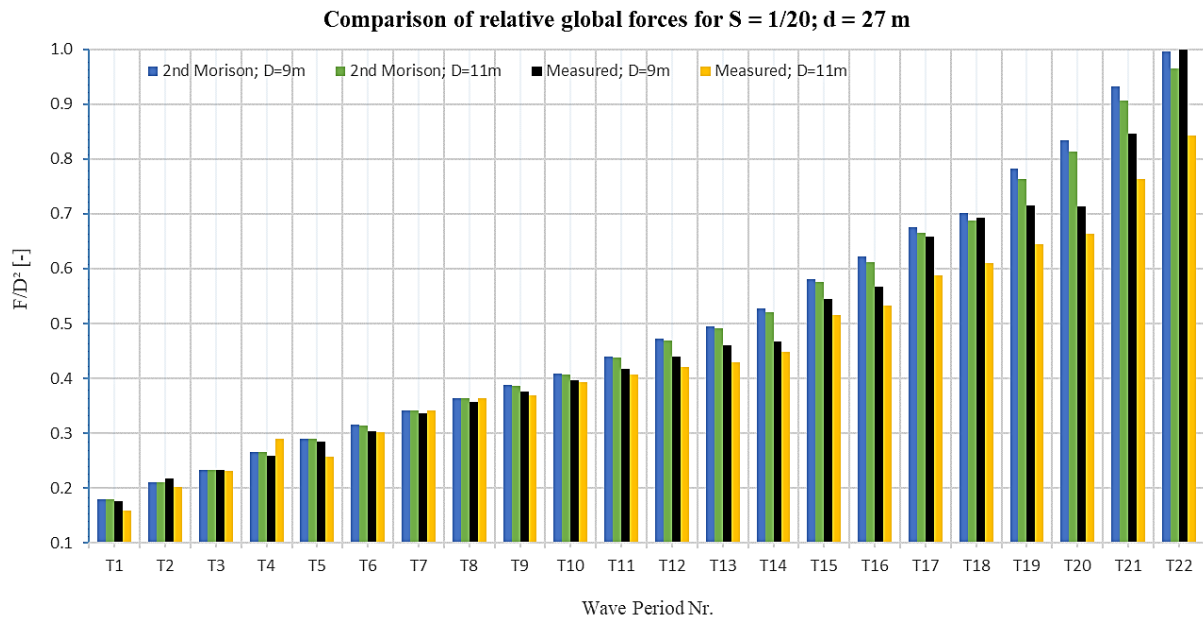


Figure 31: Comparison of relative global forces between two pile diameters for $S = 1/20$

In the first ten wave periods, a clear similarity between the diameters for both calculated and measured forces is observable. However, with a further growth of wave period, a greater discrepancy occurs between the calculated and measured forces, and between the diameters. Although the discrepancy between the diameters in calculated forces remains relatively insignificant, that is not the case for measured forces. The highest discrepancy (roughly 20%) in measured forces was found for the longest wave period, $T = 16\text{ s}$. Here, the impact of inertial effects dropped meaningfully.

As an additional comparison, a “gentle” wave of steepness $S = 1/40$ was selected. Its results are given in Figure 32. Most of the tendencies regarding the steepest wave were again observed. However, the previous strong drop in measured inertial force during longer wave periods did not occur; generally, the inertial force was even higher. Because the increase of drag force for this steepness between the diameters is not as large as for $S = 1/20$, the issue was likely caused by the experimental uncertainty, which was not quantified.

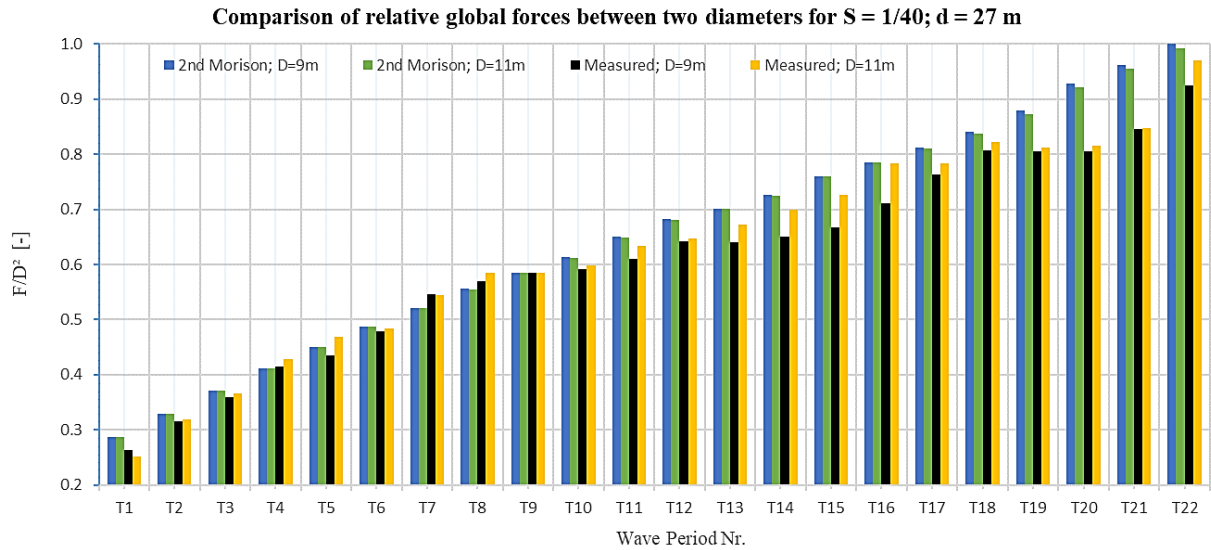


Figure 32: Comparison of highest relative global forces between two pile diameters, $S = 1/40$

Comparison of the Total & Global Force Over Time

Having presented the maximum force over all wave periods, it is useful to select a specific wave condition and observe the total and global force development over a time interval. The wave conditions RS20T6 and RS20T14 were therefore selected and investigated. The forces were again normalized by setting the maximum occurring value in the investigated conditions to 1.0. The upper panel of Figure 33 shows RS20T6. Because their amplitudes are higher, all methods of calculation overpredict the global acting force. Furthermore, the phase is not always exact. However, the shape of the force is closest to the measured when using second-order Stokes kinematics with the Morison or Rainey equations. Other fifth-order theories have identical amplitudes, with slightly different phases. For better transparency, the maximum value of the vertical axis was selected to be 0.3. The lower panel of Figure 31 shows RS20T14. An increase in the drag term was more significant here and was mainly responsible for the non-symmetrical shape of the force. A similar phase shift was observed, but all wave theories were able to replicate the form of the measured wave sufficiently well. The closest in amplitude and wave height was the fifth-order Stokes wave with the Morison equation. This result was expected because the second-order Stokes theory fell well beyond the zone of applicability.

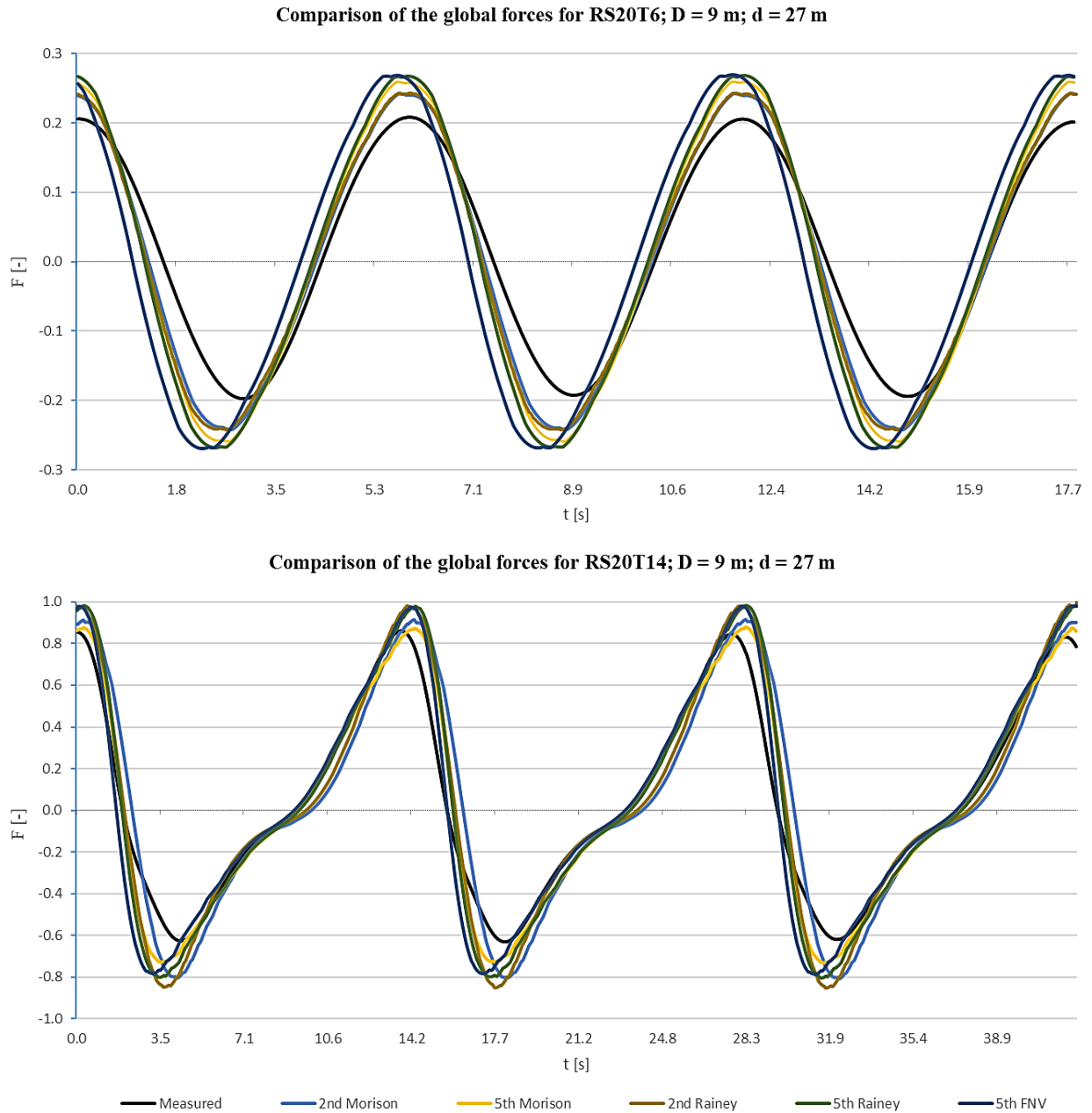


Figure 33: Comparison of measured and calculated total & global forces over a time step

Comparison of Higher Order Loads

The last (but not least important) validation of results was to analyze the magnitude of higher order terms. All relevant force terms for the wave conditions RS20T6 and RS20T14, and for both water depths, and for the pile diameter $D = 9\text{ m}$, are presented in the following diagrams. All forces were normalized in that the highest magnitude in an investigated order had the value 1.0. Setting the highest magnitude in every order to the value 1.0 enabled the comparison of the higher-order terms, that are significantly lower in magnitude than the first-order term. The impact of the higher-order magnitudes in example of second-order Stokes kinematics using Morison equation was given in Chapter 3.2.4

The magnitudes of the first-order terms are shown in Figure 34. All the calculation methods slightly overpredicted the force in all examined conditions compared to the measured ones. Although the calculated magnitudes were expected to be identical for this order, small discrepancies occurred between methods that used second-order Stokes kinematics versus fifth-order Stokes kinematics. The main reason lay in the different approximations of wave numbers.

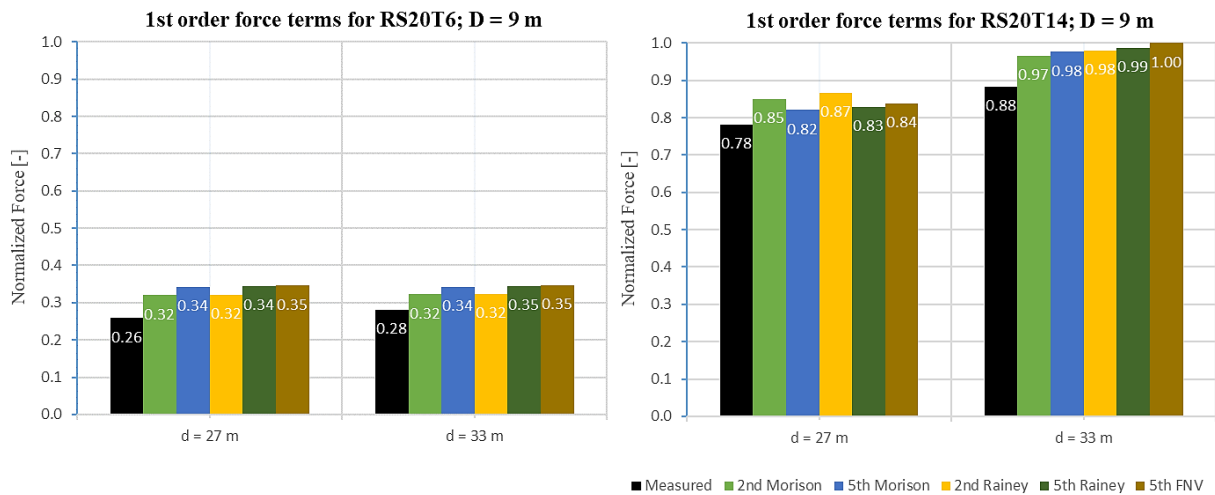


Figure 34: Comparison of first-order force-term magnitudes

In the second order of the force, several different tendencies were noted. In the wave condition RS20T6 (Figure 35, left), not all calculation methods correctly captured the force magnitude of

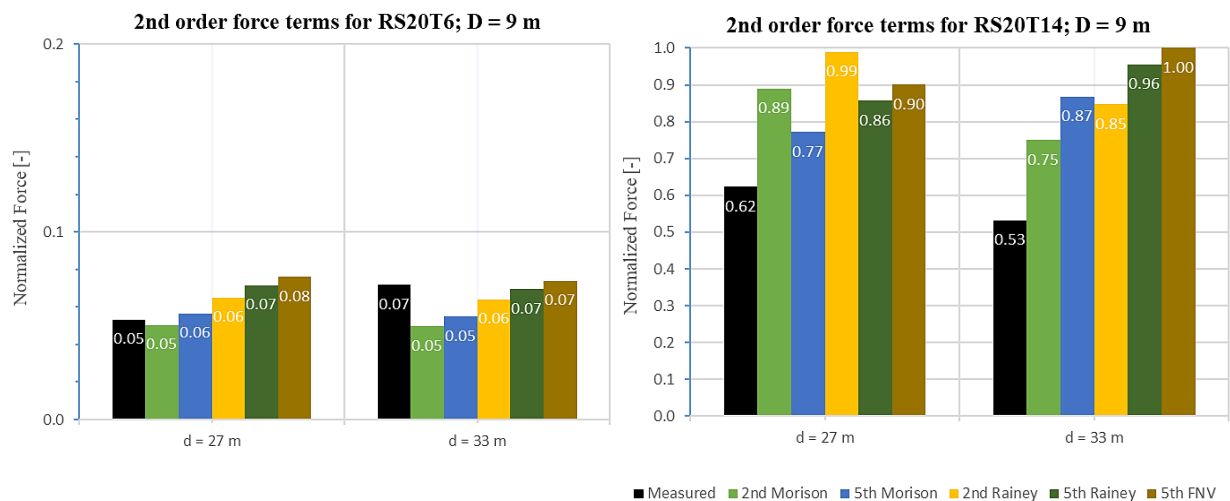


Figure 35: Comparison of second-order force-term magnitudes

the measured force. This was particularly true for the Morison equation using second-order Stokes kinematics. For the wave condition RS20T14 (Figure 35, right), there was a strong overprediction when using the calculation methods. In this case, none of the methods accurately captured the effects of the second-order.

Figure 36 shows the third-order terms. The magnitude of the terms at the wave condition RS20T6 were almost non-existent. However, they did still occur, even in the measured waves. For the wave condition RS20T14 at water depth $d = 27\text{ m}$, the measured force term was unexpectedly low. A possible explanation for this result might be a strong influence of wave reflection from the beach, or higher order diffraction in the wave tank affected by side-wall reflections. At water depth $d = 33\text{ m}$, the calculation methods using second-order Stokes kinematics underestimated the forcing term.

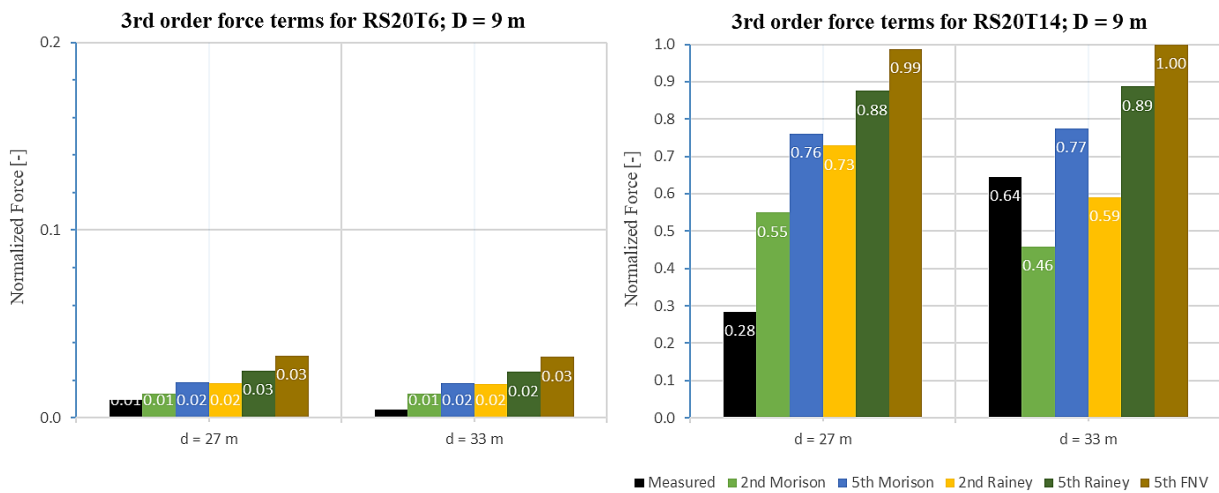


Figure 36: Comparison of third-order force-term magnitudes

The fourth-order measured force term for the wave condition RS20T6 was negligible (Figure 37), but the calculation methods predicted some forcing. By contrast, in the wave condition RS20T14, the calculation methods using second-order theory gave the most accurate results. The FNV theory showed the highest error here.

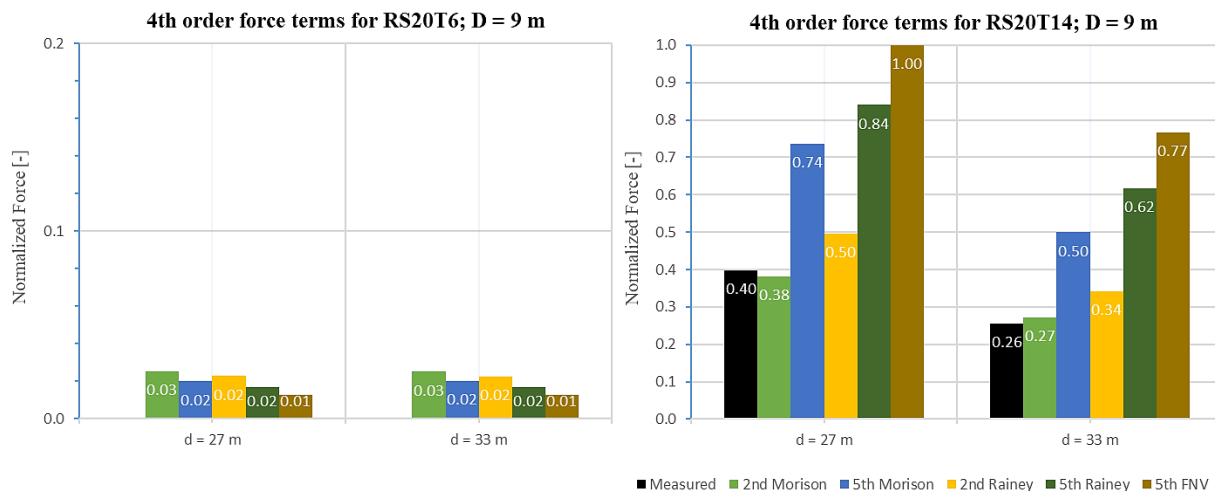


Figure 37: Comparison of fourth-order force-term magnitudes

The fifth and sixth force order terms of RS20T14 are summarized together in Figure 38, as they delivered identical results. The RS20T6 state had no terms in these orders. The calculation methods using the Morison equation with second Stokes kinematics could not estimate the forcing in these orders. The method that showed the least average discrepancy compared with the measured force was the Morison equation with fifth Stokes kinematics. Compared to the first-order terms, the magnitudes of these two high-order terms were about 40 to 300 times lower.

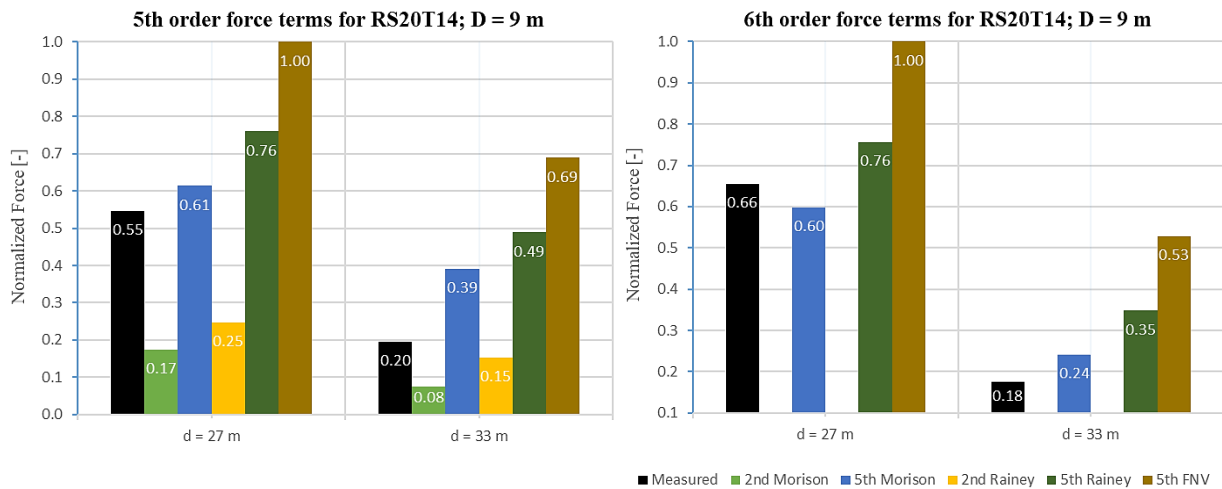


Figure 38: Comparison of fifth and sixth order force-term magnitudes

Lastly, it should be underlined that the measured values were exposed to many uncertainties due to limitations in the wave flume and measuring error. This sometimes led to smaller and sometimes to larger discrepancies among the results. The applied low-pass filter could also influence higher-order forces. Particularly the force terms in the fifth and sixth order should be interpreted with caution.

4.3.2 Irregular Wave Validation

To obtain accurate statistical results for irregular waves, it was necessary to test as many realizations (seeds) as possible for each sea state. However, the tests are immensely time-consuming, so a compromise of 10 seeds was selected for the investigation. In addition, to check the reliability of the measurements, repetition tests for a few seeds were performed. Effective duration of the tests corresponds to three-hours measurements of the full scale.

Due to limitations of the wave-maker through overvoltage, only a few runs of sea-state tests at water depth $d = 33\text{ m}$ were conducted and considered in the analysis. The sea states were IH6.5T12G1.4, IH9T12.5G2.6, and IH6.8T13.2G1. In those three sea states, the maximum amplitude of $\zeta_a = 11.56\text{ m}$ was observed in IH9T12.5G2.6, which was considerably higher than $\zeta_a = 8.86\text{ m}$, the highest calculated value for wave elevation.

After the wave elevation was measured and the wave spectrum was obtained, a minor smoothing of the function was applied. This enabled a clearer shape of the spectrum and a slightly better comparison against the calculated or theoretical spectrum.

Figure 39 shows the fifth seed of the calibration tests, resulting in the spectra for the representative sea state IH9T12.5G2.6 and two water depths. Initial examination of the form of the spectrum that was obtained from the measured waves yielded a noisy border-line. By contrast, a theoretical wave spectrum had a smooth border-line. The spectra gained from the wave-tank measurements differed in amplitude for both water depths, which should induce different forces. The theoretical spectrum did not depend on the water depth and peaked at $S_j = 26.5\text{ m}^2\text{s}$ (Figure 20), whereas the measured spectrum peaked at $S_{d=27\text{m}} = 18.1\text{ m}^2\text{s}$ and $S_{d=33\text{m}} = 20.0\text{ m}^2\text{s}$. This result implies a lower wave energy around the peak frequency, which could be caused by the wave breaking along the tank.

The red vertical lines show the borders of the theoretical spectrum. A small peak of low frequency on the left side of the borders indicates the frequency-difference between tank sloshing (seiching) and wave-reflections. This resulting frequency could residue from previous wave runs and can coincidence with the wave frequency; it should however not produce significant forcing by itself. The high-frequency tail to the right of the second red line was reconstructed fairly well.

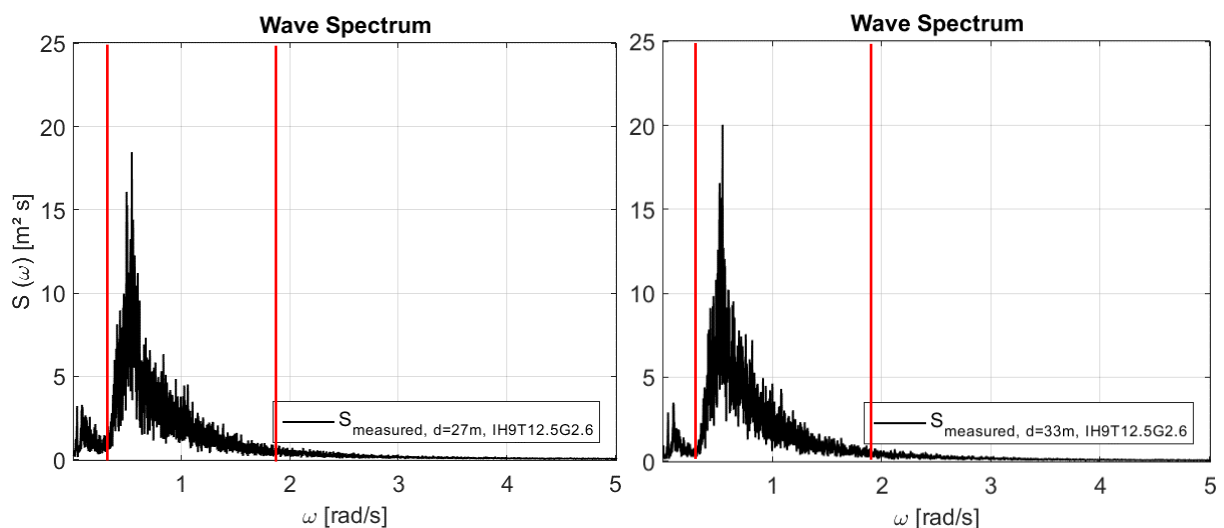


Figure 39: Examples of irregular wave spectra for IH9T12.5G2.6 in two water depths

In the case of other investigated sea states, the difference in spectrum-amplitudes was slightly less prominent than in this example. These results appear in the Appendix (Figures 54 and 55). Although the comparison between the calculated loads gained from the JONSWAP spectrum and the measured loads was not fully adequate, it could still be useful to observe the influence of certain effects that occurred. Therefore, the largest global loads were identified from the measurements in the wave flume and were compared with the theoretically calculated loads. Here, the normalization was again applied. Table 7 shows the comparison for three representative sea states and two pile diameters at water depth $d = 27\text{ m}$. The first observation, valid for both calculated and measured loads, was that the greatest global force occurred in the sea state IH9T12.5G2.6. The calculation strongly overpredicted the maximum force in this sea state. For other sea states, the calculated forces were generally slightly higher than the measured forces, but this discrepancy could perhaps be accounted for by experimental error. Furthermore, the force between the diameters grew roughly by expected 50% due to the domination of the inertia term in irregular waves.

Table 7: Maximum global force in irregular waves (water depth $d = 27\text{ m}$)

	Normalized max. global force [-]		
	$d = 27\text{ m}$, IH6.5T12G1.4	$d = 27\text{ m}$, IH9T12.5G2.6	$d = 27\text{ m}$, IH6.8T13.2G1
D = 9 m; calculated	0.43	0.69	0.44
D = 9 m; measured	0.41	0.48	0.41
D = 11 m; calculated	0.61	0.99	0.75
D = 11 m; measured	0.58	0.74	0.58

Table 8 shows a comparison of the maximum global force at water depth $d = 33\text{ m}$ in the same manner as in Table 7. Most conclusions from the previous table are identical here. However, there is a noteworthy difference between the two water depths regarding the maximum global force. Although the calculation included integration over a longer length, the calculated forces did not increase significantly with an increase in water depth, whereas the measured forces did. Global-force difference in the integration length for $d = 33\text{ m}$ was compensated by higher forces caused by shallow-water effects in $d = 27\text{ m}$. Another reason lies in the different spectra that exist in measured waves for two water depths but not in the JONSWAP spectrum.

Table 8: Maximum global force in irregular waves (water depth $d = 33\text{ m}$)

	Normalized max. global force [-]		
	$d = 33\text{ m}$, IH6.5T12G1.4	$d = 33\text{ m}$, IH9T12.5G2.6	$d = 33\text{ m}$, IH6.8T13.2G1
D = 9 m; calculated	0.44	0.69	0.45
D = 9 m; measured	0.49	0.59	0.46
D = 11 m; calculated	0.63	1.00	0.66
D = 11 m; measured	0.67	0.85	0.65

Because the distribution of wave energy is overestimated with the theoretical JONSWAP spectrum, further research could investigate the PM or TMA spectra. Additionally, the force calculated through the measured wave elevation would be more reasonable to use for

comparison. For even more accurate results, second-order irregular wave kinematics could be implemented.

4.4 Conclusions

In this chapter, several calculated versus measured load cases were compared. To provide a conclusion about which calculation method showed the best overall agreement with the measured values, four criteria were evaluated. The results are shown in Table 9. The criteria were weighted with different factors because their importance differed. An agreement of higher-order loading was assumed to be the most important, whereas load distribution along the pile was the least relevant. Where the calculation method fully agreed with the measurements, 10 points were assigned and the cell in the table is shaded dark green. If there was total disagreement, only 1 point was given, with dark red shading. The method with the highest sum is the best choice for the investigated environmental conditions.

Table 9: Comparison of the calculation methods

	<i>Weighting Factor: 15%</i>	<i>Weighting Factor: 20%</i>	<i>Weighting Factor: 30%</i>	<i>Weighting Factor: 35%</i>	
	<i>Load distribution along the pile</i>	<i>Max. global load</i>	<i>Load form over time</i>	<i>Higher-order load</i>	<i>Sum</i>
LWT	2	3	3	1	2.15
2 nd Morison	8	8	8	7	7.65
5 th Morison	7	6	8	8	7.45
2 nd Rainey	6	7	7	7	6.85
5 th Rainey	6	5	6	6	5.8
5 th FNV	6	4	6	5	5.25

None of the methods was able to completely capture the loads in all evaluated segments. However, the results showed that the best overall agreement was yielded by the Morison equation using second-order Stokes kinematics. Given that there was a slight overprediction of the loading with the fifth-order Stokes kinematics due to different wave number approximations, which led to minimally worse results, the fifth-order Morison was adequate. By contrast, the Rainey and FNV methods gave highly conservative results, which made them a non-optimal choice. Lastly, using LWT for these conditions would lead to strong underprediction in all aspects.

The wave elevation tests showed that there were some experimental uncertainties. Therefore, the results from the comparison of calculated versus measured loads should be interpreted with caution.

Compared to the measured spectrum, the results obtained by using the JONSWAP spectrum in the investigated irregular sea states gave only satisfactory results. The maximum random wave height that was observable within 10 seeds was considerably underpredicted. By

contrast, the forces obtained by using the JONSWAP spectrum were mostly overpredicted, which is a sign of the uncertainty of this theoretical method. The loads were fully inertia-dominated.

5 Calculated Responses for the Flexible Structure

Managing the wave responses is an important step to maximize the power output and reduce its fluctuations due to undesired behavior of the structure. To test responses using the calculated load models from the last two chapters, a numerical model was developed in *MATLAB*. It served as a simple SDOF system. In this chapter, structural parameters and the calculation methods are first presented. Then the response and displacement results are presented together with an analysis.

5.1 Structural Parameters

Based on a *SIMA* model of the complete wind turbine, including soil springs below the mudline, the first mode shape (ϕ_s) of the monopile was obtained. *SIMA* is a nonlinear, finite-element based tool that enables various dynamic calculations. Several calculations in this program were conducted by NTNU at the start of this study, and the results – in the form of structural information – were recorded and given as input for the following calculations [35]. The monopile model in *SIMA* and the shape of the first eigenmode are illustrated in Figure 40.

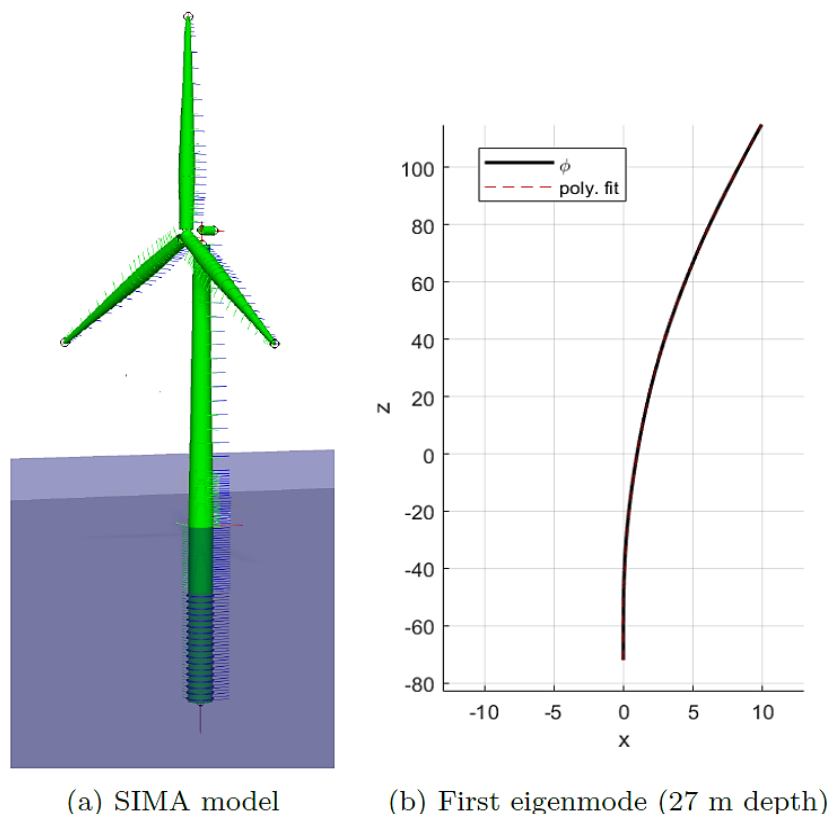


Figure 40: Monopile model with the first eigenmode [35]

The shape function (or generalized coordinates) are used to find approximate values for the eigenfrequencies of a beam, and to calculate dynamic responses, as follows:

$$\phi_s(z) = p_1 z^5 + p_2 z^4 + p_3 z^3 + p_4 z^2 + p_5 z + p_6 \quad (42)$$

where z represents the length segment of the turbine. The coordinate system is such that $z = 0$ is the mean still-water level, and z is positive upward. Six polynomial coefficients p for both water depths and structural diameter $D = 9 \text{ m}$ are given in Table 10. Using these values, it was possible to calculate the shape function for each length segment of the structure. Furthermore, the goodness of a calculation method depends on how accurately the shape function is determined. It should be noted that monopile structures have a range of structural modes in reality.

Table 10: Polynomial coefficients

	$d_1 = 27 \text{ m}$	$d_2 = 33 \text{ m}$
p_1	$-6.3817 \cdot 10^{-12}$	$-3.0614 \cdot 10^{-12}$
p_2	$-2.1694 \cdot 10^{-09}$	$-9.6657 \cdot 10^{-10}$
p_3	$5.1552 \cdot 10^{-07}$	$2.2191 \cdot 10^{-07}$
p_4	$3.5123 \cdot 10^{-04}$	$3.1223 \cdot 10^{-04}$
p_5	$3.5290 \cdot 10^{-02}$	$3.8804 \cdot 10^{-02}$
p_6	$9.5891 \cdot 10^{-01}$	$1.2502 \cdot 10^{+00}$

SIMA does not directly give an output of the modal mass and stiffness but provides the generalized coordinates for the mode. Therefore, the mass and stiffness distribution from the *SIMA* model were used in Eq. 43 and Eq. 44 and numerically integrated in *MATLAB*.

$$\bar{m} = \int_L m \phi_s^2 dz \quad (43)$$

$$\bar{k} = \int_L EI \frac{\partial^2 \phi_s}{\partial z^2} dz + \int_L k \phi_s^2 dz. \quad (44)$$

Structural damping is the structure's internal damping caused by plastic deformations and non-ideal behavior of the material. Calculating the exact damping-contributions is impossible for most of the cases. Critical damping for the first mode, with a reasonable assumption of damping ($\zeta = 2\%$), is given by the following equation:

$$\bar{c} = 2\bar{m}\omega_n\zeta. \quad (45)$$

The natural frequency of the system, ω_n , is found identically to Eq. 36, by the proportion of generalized stiffness and mass. All the calculated parameters for both water depths are presented in Table 11.

Table 11: SDOF model parameters

	$d_1 = 27 \text{ m}$	$d_2 = 33 \text{ m}$
\bar{m} [kg]	$1.0279 \cdot 10^{+08}$	$1.2163 \cdot 10^{+08}$
\bar{k} [N/m]	$2.8351 \cdot 10^{+08}$	$2.8890 \cdot 10^{+08}$
\bar{c} [Ns/m]	$6.8284 \cdot 10^{+06}$	$7.4980 \cdot 10^{+06}$
ω_n [rad/s]	$1.6608 \cdot 10^{+00}$	$1.5412 \cdot 10^{+00}$

Solving the differential equation for dynamic equilibrium using generalized parameters leads to the structural response; the equation is as follows:

$$\bar{m}\ddot{Y} + \bar{c}\dot{Y}(t) + \bar{k}Y(t) = \bar{P}. \quad (46)$$

Eq. 46 is identical to Eq. 35 and can be solved numerically with *MATLAB* function ODE45, where \bar{P} is the generalized force. It is calculated by the integration of the product of the distributed load per unit length f with the shape function:

$$\bar{P} = \int_L f \phi_s dz. \quad (47)$$

However, the force distribution along the structure is not obtainable from the measurements. Here, the total global force can be assumed to act at the SWL, and through multiplication with the shape function, the generalized force is obtainable.

For a “static” response with a constant load acting along the structure, Eq. 46 can be simplified as follows:

$$Y_{stat} = \frac{\bar{P}}{\bar{k}}. \quad (48)$$

When the response of the structure is known, the displacement for each point along the beam can be found by multiplication of the response with the previously introduced shape function:

$$w_d(z) = \phi_s(z)Y. \quad (49)$$

5.2 Response and Displacement Analysis

The first step in analyzing the structural behavior under periodic loads is to observe the development of the total response over a time step. For that purpose, all previously calculated global loads for a representative wave condition (RS20T14) at water depth $d = 27 \text{ m}$ were used as input for the equation of motion (Eq. 46). Its solving for each calculation method yielded the responses presented in Figure 41.

An observation, which is valid for all forcing inputs, is that the oscillation process starts with a transient effect in the form of several high-amplitude oscillations. After about $t = 40 \text{ s}$, the response settles down to a constant form with the amplitude of $A = 0.022 \text{ m}$ for measured forces, or $A = 0.038 \text{ m}$ for FNV-forcing. This behavior implies that the response lies beyond the resonance range. The non-linearities that occur in the forces affect the response meaningfully, in the form of smaller bumps. The effects of non-linearities are amplified and are thus more pronounced here. When the linear forcing is used as an input, the response after $t = 40 \text{ s}$ would be fully symmetrical over time, with significantly lower amplitudes. This trend would lead to marked underestimation of the maximum response.

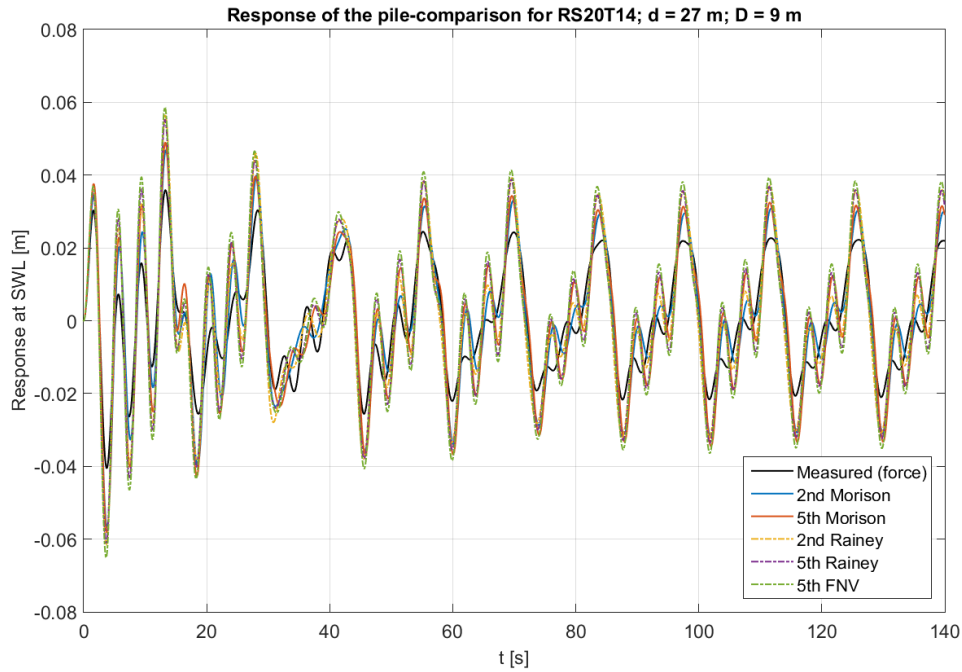


Figure 41: Comparison of the structural response, RS20T14

A closer look at the settled-down part of the response development (Figure 42) revealed that in this wave condition, all wave theories overpredicted the amplitude of the structural response. The measured force as input for the equation of motion was assumed to be representative, as the response tests on a model were not conducted in this study. In addition, the “bumpy” phase was replicated correctly. The theory that achieved the results closest to the measured data used the Morison equation with second-order Stokes kinematics. The FNV-theory showed the greatest discrepancy in this case due to overestimation of higher-order forces.

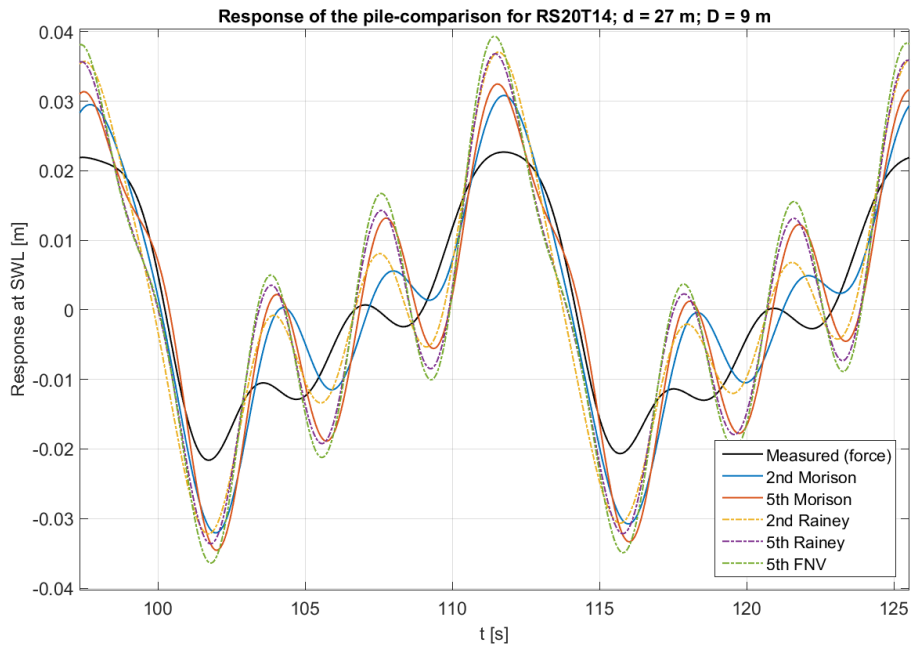


Figure 42: Comparison of the structural response, RS20T14 (zoomed)

As in Eq. 49, multiplying the maximum response by the shape function yielded the maximum displacement along the pile. This distribution is shown in Figure 41 in the form of solid lines. Here again, all calculated forces induced a higher displacement along the structure compared to the measured forces. Two responses with the Morison equation were distributed identically, whereas the Rainey and FNV equations yielded similar displacements. Overestimation by the Morison equation was approximately 35%, and by the Rainey and FNV equations it was 55% in each case. A slight displacement was also evident at the seabed, caused by the movement of the pile in the mud. This motion was included in the shape form.

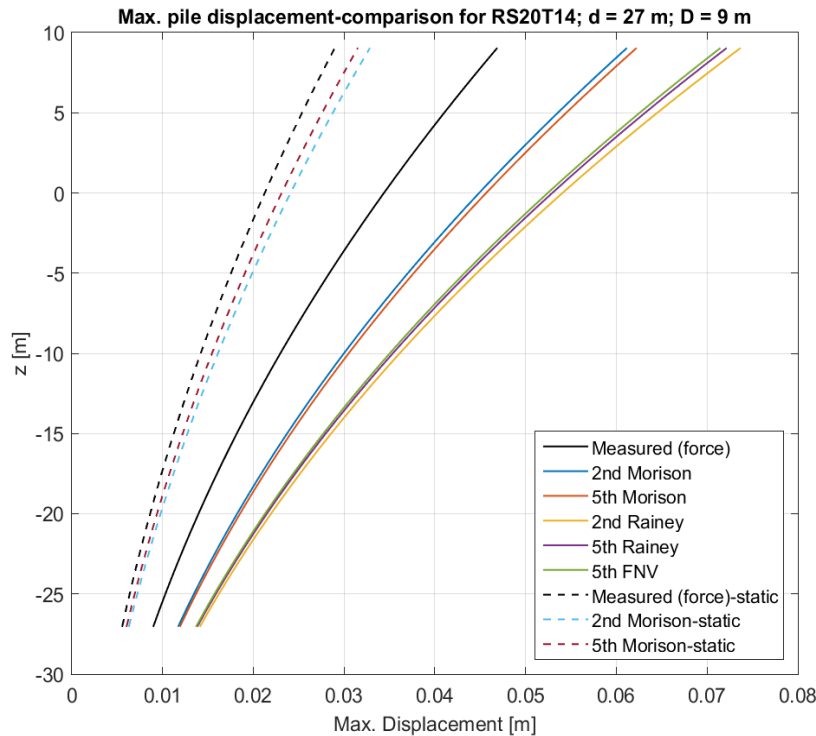


Figure 43: Comparison of the max. displacement along the structure for dynamic and static excitation, RS20T14

To validate the previous dynamic results, deformations caused by the static response were calculated and are shown by the dashed lines in Figure 43. For this purpose, the highest load from the model experiments and Morison equation was found and was applied as the static input in Eq. 46. That calculation yielded the fixed motion of the structure. As expected, the dynamic displacement of the structure was significantly higher than the static displacement. The difference between the measured forces was 62% and between the Morison equations it was 88%.

For comparison, the wave condition RS20T6 was chosen. The higher-order effects in this low-period wave condition are meaningfully lower, so the response was expected to be dissimilar. Figure 44 shows this response in its full form and during a selected time interval. After the transient part of the response, it became almost fully linear, due to the lower magnitude of higher-order forcing. This tendency was prominent for the measured force.

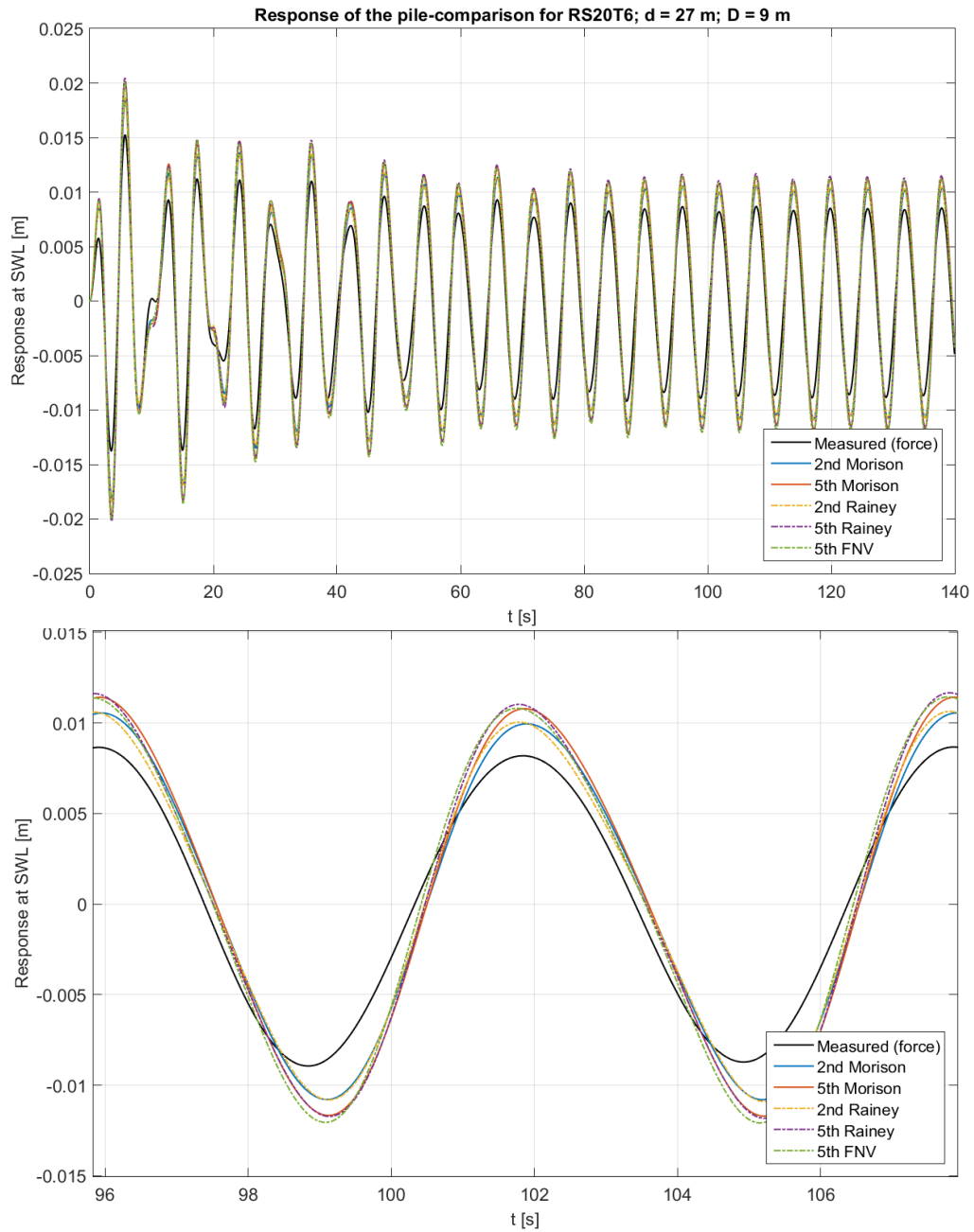


Figure 44: Comparison of the structural response, RS20R6

As demonstrated in the last chapter, all calculation methods for this wave condition overpredicted the magnitude of higher-order terms. In the lower panel of Figure 44, non-linearity of these responses was observable. The closest prediction to the measured forcing as input were from both theories that used second-order Stokes kinematics. The amplitude yielded by these calculation methods was about 20% higher than the measured amplitude.

Lastly, the maximum displacement of the pile was considerably lower than in the last wave condition, due to smaller forces (Figure 45). The most interesting observation was the increase of the dynamic response compared to the static one. For the measured forces, the dynamic response was almost three times higher than the maximum static response.

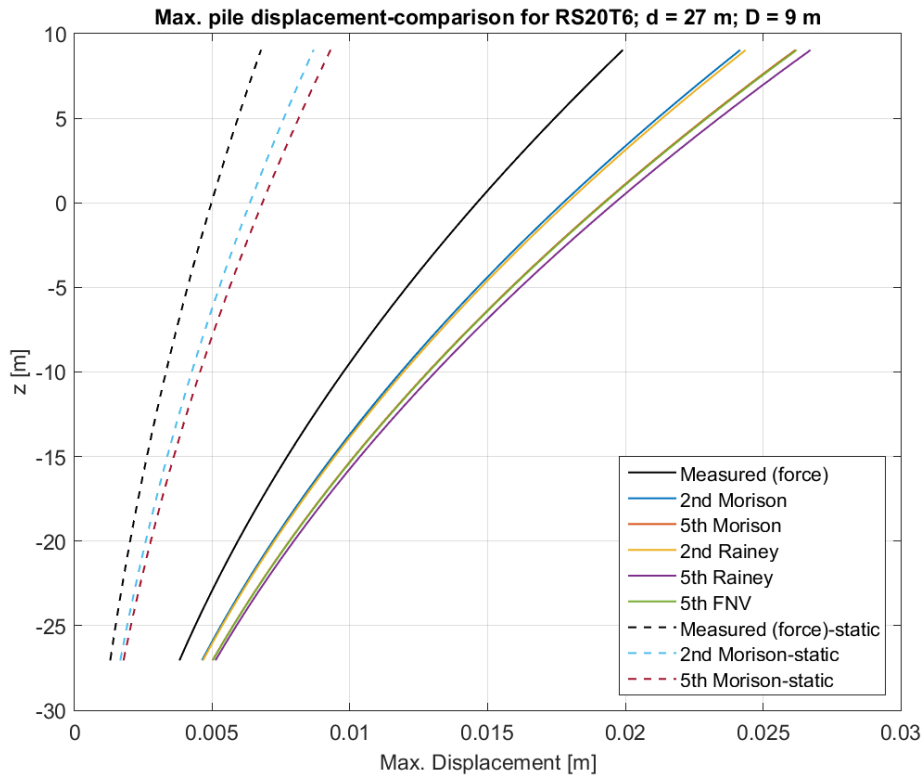


Figure 45: Comparison of the max. displacement along the structure for dynamic and static excitation, RS20R6

5.3 Conclusions

The general trend was that the response for all wave conditions had a transient form when excited, in which the highest magnitudes occurred. After a specific time period, the response form stabilized and remain roughly constant. These results meant that the investigated wave conditions feel outside of the resonance range.

The nonlinearity of the structural response is caused by nonlinear forces. In the response, the nonlinearity was observable as “bumpy” behavior instead of a symmetrical sinusoid form. The magnitude of the response is influenced as well as the form. Furthermore, if static calculations were used instead of dynamic calculations for the sake of simplicity, the response was strongly underpredicted.

6 Summary and Recommendations for Further Work

6.1 Summary

Predicting hydrodynamic loads and the structural response they induce on an offshore structure is a central aspect of correct design. This thesis was initiated to better understand the applicability of several common methods for computing hydrodynamic loads, using Stokes waves and obtaining a first prediction of the structural response. In this section, general observations are noted and the conclusions from the third, fourth, and fifth chapters are summarized.

The global hydrodynamic loads are mainly inertia-dominated and the pile structure can be assumed to be slender. The diffraction effects of the first order are thus insignificant. Nonlinear wave models approximated the occurring effects meaningfully, better than a pure linear model, which was expected due to nonlinearity of the examined steep waves. Generally, nonlinearity effects are amplified with an increase in structural diameter, steepness, or wave period. The nonlinearities were best predicted with the Morison model. The Morison model predicted the loads slightly better than the Rainey and FNV models, not only in terms of non-linearity but also regarding most of the investigated criteria. Those criteria included load distribution along the pile, maximum global load, and load development over time.

When the first three to four wave harmonics were important, the second-order Stokes wave kinematics was generally the best option. For all other cases, the fifth-order Stokes wave kinematics gave more accurate results. Although there was slight overprediction of the first-order term when using fifth-order wave number approximation, which mostly led to higher total forces, the fifth-order kinematics paired with the Morison equation was the most promising method for most of the investigated wave conditions. Because of increased calculation complexity, a benefit for practical applications of using fifth-order kinematics over second-order kinematics for the investigated wave conditions is however rather limited.

The non-linearities in the loads were even more prominent when implemented in the calculations of the structural response. That meant that response calculations gave more reasonable results for “gentle” waves, since the non-linearity effects were lower. For all investigated wave conditions, using the calculated forces as input in the equation of motion yielded a higher structural response than when the measured force was used as input. However, the Morison equation using second-order Stokes kinematics gave the closest results to the measured forces used as input. Depending on the investigated wave condition, the greatest difference in the response-amplitude between those two methods was 25% to 30%. When the wave hits the structure, a transient high-amplitude response is induced. Afterwards, the response stabilizes and hence lies beyond the resonance zone.

Using the JONSWAP spectrum to describe the energy distribution of the investigated irregular sea states gave only satisfactory results, compared to the measured spectrum. The maximum random wave height that was observable within 10 seeds was considerably lower than the measured height. Using the Morison equation to obtain the forcing led to the forces

being fully inertia-dominated. The forcing obtained using the JONSWAP spectrum was mostly overpredicted, which is a sign of the uncertainty of this method.

6.2 Recommendations for Further Work

In this study, a few sea conditions with a long wave period were not considered because they were outside of the range of validity. To take them into account, the fifth-order stream theory should be used to describe the kinematics.

Experimental uncertainty is inherently present in every model test because of wave tank limitations, measurement accuracy, and repeatability. Their impact should therefore be investigated and quantified to validate the experimental results. However, the measuring error during the test was kept to a minimum. To improve the accuracy of the irregular simulated surface process and the kinematics of the maximum event, the second-order process should be implemented. This would describe the wave history more similarly to the real ocean conditions, by increasing the crest height and reducing the trough depth.

Given that the distribution of the wave energy was mostly overestimated with the theoretical JONSWAP spectrum, the PM or TMA spectrum should be investigated in further research. PMA spectrum could be of special interest as it considers the dissipation of energy due to shallow water effects. Furthermore, the forces calculated with the measured wave elevation should be compared with the measured forcing in addition to using a theoretical spectrum.

Only the responses induced by regular waves were calculated and investigated in this thesis. Many important effects – like ringing or springing – could be observable if irregular waves acted on the structure. Moreover, several simplifications regarding the form of the structure and neglecting the wind loads were used when calculating the response. Those simplifications should also be included when measuring the test response and comparing the data with the calculated responses (Chapter 5). If the measured results for the response show promise, the study in this thesis should be repeated without the simplifications.

References

- [1] C. R. I. Funke, Offshore Wind Industry, 18 09 2017. [Online]. Available: <http://www.offshorewindindustry.com/news/european-offshore-wind-energy-market-expected>. [Accessed 05 08 2018].
- [2] Wind Europe, "The European Offshore Wind Industry," January 2017. [Online]. Available: <https://www.equinor.com/content/dam/statoil/documents/innovate/WindEurope-Annual-Offshore-Statistics-2016.pdf>. [Accessed 05 09 2018].
- [3] L. Arany, S. Bhattacharya, J. MacDonald and S. Hogan, "Design of monopiles for offshore wind turbines in 10 steps," *Soil Dynamics and Earthquake Engineering*, pp. 126-152, 2017.
- [4] M. J. Kaiser and B. Snyder, "Offshore Wind Energy Installation and Decommissioning Cost Estimation and Decommissioning Cost Estimation," Energy Research Group, LLC, Louisiana, U.S., 2010.
- [5] GE - Renewable Energy, [Online]. Available: <https://www.ge.com/renewableenergy/wind-energy/turbines/haliade-x-offshore-turbine>. [Accessed 17 09 2018].
- [6] SINTEF, [Online]. Available: <https://www.sintef.no/projectweb/was-xl/>. [Accessed 27 09 2018].
- [7] E. E. Bachynski, T. Kristiansen and M. Thys, "Experimental and numerical investigations of monopile ringing in irregular finite-depth water waves," *Applied Ocean Research* 68, pp. 154-170, August 2017.
- [8] E. E. Bachynski and H. Ormberg, "Hydrodynamic Modeling of Large-Diameter Bottom-Fixed Offshore Wind Turbines," in *ASME 2015 34th International Conference on Ocean, Offshore and Arctic Engineering*, St. John's, NL, Canada, 2015.
- [9] O. M. Faltinsen, J. N. Newman and T. Vinje, "Nonlinear wave loads on a slender vertical cylinder," *J. Fluid Mech.* 289, pp. 179-198, 1995.
- [10] M. Karimirad, *Offshore Energy Structures for Wind Power, Wind Energy and Hybrid Marine Platforms*, Cham, Heidelberg, New York, Dordrecht, London: Springer Verlag, 2014.

-
- [11] Det Norske Veritas AS, "Recommended Practice C205, Environmental Conditions and Environmental Loads," 2007.
- [12] G. Clauss, E. Lehmann and C. Östergaard, *Offshore Structures, Vol. 1, Conceptual Design and Hydromechanics*, London: Springer Verlag, 1992.
- [13] NORSOK Standard N-003, "Actions and action effects, Edition 2," Lysaker, Norway, 2007.
- [14] US Army Corps of Engineers, "Water Wave Mechanics EM 1110-2-11000 (Part 2)," 2008.
- [15] R. G. Dean and R. A. Dalrymple, *Water Wave Mechanics for Engineers and Scientists*, Singapore: World Scientific Publishing Co.Pte. Ltd., 1991, pp. 300-305.
- [16] L. Skjelbreia and J. Hendrickson, "Fifth Order Gravity Wave Theory," National Engineering Science Company, Pasadena, California, 1961.
- [17] J. D. Fenton, "A Fifth-Order Stokes Theory for Steady Waves," *Journal of Waterway, Port, Coastal and Ocean Engineering*, vol. 111, no. 2, pp. 216-234, 1985.
- [18] H.-K. Chang and S.-C. Lin, "An explicit approximation to the wavelength of nonlinear waves," *Ocean Engineering* 26, pp. 147-160, 1999.
- [19] J. D. Fenton and W. D. McKee, "On calculating the lengths of water waves," *Costal Engineering* 14, pp. 499-513, 1990.
- [20] J. D. Fenton, "Nonlinear Wave Theories," *The Sea, Vol.9: Ocean Engineering Science*, 1990.
- [21] R. G. Dean, "Stream Function Representation of Nonlinear Ocean Waves," *Journal of Geographical Research, Vol. 70, Issue18*, p. 1965, 15 09 1968.
- [22] Det Norske Veritas AS, "Offshore Standard J101, Design of Offshore Wind Turbine Structures," 2014.
- [23] J. Twidell and G. Gaudiosi, *Offshore Wind Power*, Brentwood, UK: Multi-Science Publishing Co. Ltd, 2009.
- [24] R. C. MacCamy and R. A. Fuchs, "Wave Forces on Piles: A Diffraction Theory," *Technical Memorandum No. 69*, 1954.
- [25] A. Mockutè, E. Marino, C. Lugni and C. Borri, "Comparison of hydrodynamic loading models for vertical cylinders in nonlinear waves," *Procedia Engineering* 199, pp. 3224-3229, 2017.

-
- [26] R. C. T. Rainey, "A new equation for calculating wave loads on offshore structures," *J. Fluid Mechanics Vol. 204*, pp. 295-324, 1989.
- [27] R. C. T. Rainey, "Slender-Body Expressions for the Wave Load on Offshore Structures," *Proceedings: Mathematical and Physical Sciences, Vol. 450, No. 1939*, pp. 391-416, 08 08 1995.
- [28] H. Bredmose, L. Sahlberg-Nielsen, P. Slabiak and F. Schlütter, "Dynamic Excitation of Monopiles by Steep and Breaking Waves. Numerical and Experimental Study," in *ASME 2013 32nd International Conference on Ocean, Offshore and Arctic Engineering*, Nantes, France, 2013.
- [29] H. Bredmose, "The Wave Loads Project," 2013. [Online]. Available: http://orbit.dtu.dk/files/103337046/DTUWind_Energy_E_0045.pdf.
- [30] O. M. F. T. Kristiansen, "Higher harmonic wave loads on a vertical cylinder in finite water depth," in *J. Fluid Mech.*, vol. 833, Trondheim, Cambridge University Press, 2017, pp. 773-805.
- [31] S. Chakrabati, *The Theory and Practice of Hydrodynamics and Vibrations*, Singapore: World Scientific Publishing Co. Pte. Ltd., 2002.
- [32] C. M. Larsen, "TMR 4182 Marine dynamics (NTNU lecture)," Trondheim, 2015.
- [33] M. Thys, E. E. Bachynski and F. Dadmarzi, "WAS-XL, Hydrodynamic Experiments, Phase 1 (Not freely accessible)," Trondheim, 2018.
- [34] J. Guo, "Simple and explicit solution of wave dispersion equation," *Coastal Engineering* 45, pp. 71-74, 2002.
- [35] E. E. Bachynski, "SDOF model for WAS-XL monopile (Not freely accessible)," Trondheim, 2018.
- [36] B. L. Méhauté, *Introduction to Hydrodynamics and Water Waves*, New York: Springer-Verlag, 1976.
- [37] USFOS Reality Engineering, 2010. [Online]. Available: http://www.usfos.no/manuals/usfos/theory/documents/Usfos_Hydrodynamics.pdf.
- [38] O. M. Faltinsen, *Sea Loads on Ships and Offshore Structures*, Cambridge, UK: Cambridge University Press, 1990.
- [39] T. Berlin, "LV Hydromechanik meerestechnischer Systeme (TU Berlin lecture)," Berlin, 2016.

A. Appendix

This appendix contains a selection of data-analysis diagrams that were not included in one of the previous chapters. An example of *MATLAB* code for calculating the Morison equation with regular second-order Stokes kinematics is additionally included. Given that it was not possible to provide diagrams for all investigated variables, the remaining *MATLAB* routines are attached in the digital appendix.

A.1 *MATLAB* code

```
% This code calculates the distribution of the forces on a monopile with a
% help of Morison equation for two water depths, five steepnesses, and 5
% wave heights.
%Stokes second-order wave theory is a non-linear theory that introduces a second
component of twice the wave frequency,
%but with a smaller amplitude, and therefore with a smaller contribution.

close all; clear; clc

%%%%%%%%%%%%%%%%%%%%%%%%%%%%%%%%%%%%%%%%%%%%%%%%%%%%%%%%%%%%%%%%%%%%%%%% Input %%%%%%%%%%%%%%%%%%%%%%%%%%%%%%%%%%%%%%%%%%%%%%%%%%%%%%%%%%%%%%%%%%%%%%%%%
g = 9.81;
rho = 1025;
d1 = 27;
d2 = 33;
T = (6:.5:16.5).';
D = 9;
s = [1/20 1/22 1/25 1/30 1/40];
dz_d1 = d1/27;
dz_d2 = d2/33;
dt = 0.0354;
omega = (2*pi)./T;
Fs = 1/dt; %sampling frequency from measurements
t = ((0:(dt):T(17)*30).');
n=length(t); %length of time domain signal;
n_2=2.^nextpow2(n); %length of signal in power of 2';
f=Fs*(0:n_2/2-1)/n_2.';
w_2=1*(f*2*pi);
%%%%%%%%%%%%%%%%%%%%%%%%%%%%%%%%%%%%%%%%%%%%%%%%%%%%%%%%%%%%%%%%%%%%%%%%

%%%%%%%%%%%%%%%%%%%%%%%%%%%%%%%%%%%%%%%%%%%%%%%%%%%%%%%%%%%%%%%%%%%%%%%%Fenton McKee Approximation of the wave number k%%%%%%%%%%%%%%%%%%%%%%%%%%%%%%%%%%%%%%%%%%%%%%%%%%%%%%%%%%%%%%%%%%%%%%%%
% k_d1 = (omega.^2)./((tanh(((omega.^2)*d1)/g).^0.75).^(2/3)*g);
% k_d2 = (omega.^2)./((tanh(((omega.^2)*d2)/g).^0.75).^(2/3)*g);
%%%%%%%%%%%%%%%%%%%%%%%%%%%%%%%%%%%%%%%%%%%%%%%%%%%%%%%%%%%%%%%%%%%%%%%%Guo's Approximation of the wave number, k_linear%%%%%%%%%%%%%%%%%%%%%%%%%%%%%%%%%%%%%%%%%%%%%%%%%%%%%%%%%%%%%%%%%%%%%%%%
k_d1 = ((omega.^2)./g).*((1-(exp(-(omega.*sqrt(d1./g)).^(5/2))))).^(-2/5));
k_d2 = ((omega.^2)./g).*((1-(exp(-(omega.*sqrt(d2./g)).^(5/2))))).^(-2/5));
%%%%%%%%%%%%%%%%%%%%%%%%%%%%%%%%%%%%%%%%%%%%%%%%%%%%%%%%%%%%%%%%%%%%%%%%

%%%%%%%%%%%%%%%%%%%%%%%%%%%%%%%%%%%%%%%%%%%%%%%%%%%%%%%%%%%%%%%%%%%%%%%%Wave Length Calculation%%%%%%%%%%%%%%%%%%%%%%%%%%%%%%%%%%%%%%%%%%%%%%%%%%%%%%%%%%%%%%%%%%%%%%%%
L_d1 = (2*pi)./k_d1;
L_d2 = (2*pi)./k_d2;
%%%%%%%%%%%%%%%%%%%%%%%%%%%%%%%%%%%%%%%%%%%%%%%%%%%%%%%%%%%%%%%%%%%%%%%%
```

```

%%%%%%%%%%%%%%%%%%%%%%%%%%%%%%%%%%%%%%%%%%%%%%%%%%%%%%%%%%%%%%%%%%%%%%%%%
Wave Height Calculation with Wave Steepness%%%%%%%%%%%%%%%%%%%%%%%%%%%%%%%%%%%%%%%%%%%%%%%%%%%%%%%%%%%%%%%%%%%%%%%%%
H_d1 = L_d1*s;
H_d2 = L_d2*s;
%%%%%%%%%%%%%%%%%%%%%%%%%%%%%%%%%%%%%%%%%%%%%%%%%%%%%%%%%%%%%%%%%%%%%%%%%

%%%%%%%%%%%%%%%%%%%%%%%%%%%%%%%%%%%%%%%%%%%%%%%%%%%%%%%%%%%%%%%%%%%%%%%%%
Cm and Cd determination%%%%%%%%%%%%%%%%%%%%%%%%%%%%%%%%%%%%%%%%%%%%%%%%%%%%%%%%%%%%%%%%%%%%%%%%%
% Cm = 2 (added mass coef.) for all frequencies according MacCamy-Fuchs
Cm = 2;
Cd = 0.9;
%%%%%%%%%%%%%%%%%%%%%%%%%%%%%%%%%%%%%%%%%%%%%%%%%%%%%%%%%%%%%%%%%%%%%%%%%

%%%%%%%%%%%%%%%%%%%%%%%%%%%%%%%%%%%%%%%%%%%%%%%%%%%%%%%%%%%%%%%%%%%%%%%%%
Particle velocities and accelerations%%%%%%%%%%%%%%%%%%%%%%%%%%%%%%%%%%%%%%%%%%%%%%%%%%%%%%%%%%%%%%%%%%%%%%%%%
% all wave parameters are stored in a 4-dimensional matrix (1st:time, 2nd:omega,
3rd:wave height, 4th:water depth)
for w=1:22 %omega, T, k
    for i=1:5 %steepness, H
        zeta_d1_t(:, :, i) = (bsxfun(@times, (cos(-
t*omega.'), (H_d1(:, i)/2).')))... %wave elevation
            + (bsxfun(@times, (cos(-
2*t*omega.'), (bsxfun(@times, (bsxfun(@rdivide, ((cosh(bsxfun(@times, (d1), k_d1.')))
.* (2 + (cosh(bsxfun(@times, (d1), 2*k_d1.'))))), sinh(k_d1.*d1).^3.'), ((pi.*H_d1(:, i)
).^2) ./ (8.*(L_d1))))).'))););
        zeta_d2_t(:, :, i) = (bsxfun(@times, (cos(-
t*omega.'), (H_d2(:, i)/2).')))... %wave elevation
            + (bsxfun(@times, (cos(-
2*t*omega.'), (bsxfun(@times, (bsxfun(@rdivide, ((cosh(bsxfun(@times, (d2), k_d2.')))
.* (2 + (cosh(bsxfun(@times, (d2), 2*k_d2.'))))), sinh(k_d2.*d2).^3.'), ((pi.*H_d2(:, i)
).^2) ./ (8.*(L_d2))))).'))););
        z_d1 = (-d1:dz_d1:round((zeta_d1_t(:, 22, 1))))'; %from the seabed to
the max. wave elevation
        z_d2 = (-d2:dz_d2:round((zeta_d2_t(:, 22, 1))))'; %from the seabed to
the max. wave elevation

        for tt = 1:length(t)
            %%%calculations for d1=27m%%
            for j=1:(28+(round((zeta_d1_t(tt, w, i)))) %1=sea bottom,
28= MWL
                u_d1_t(tt, w, i, j) = (bsxfun(@times, (cos(-
t(tt)*omega(w).'), (bsxfun(@times, (bsxfun(@rdivide, ((cosh(bsxfun(@times, (j-
1), k_d1(w).'))), sinh(k_d1(w).*d1).' ), (H_d1(w, i)/2).*omega(w).')))...
                    + bsxfun(@times, (cos(-
t(tt)*2*omega(w).'), (bsxfun(@times, (bsxfun(@rdivide, ((cosh(bsxfun(@times, (j-
1), (2*k_d1(w).'))), (sinh(k_d1(w).*d1).^4), ((3*(H_d1(w, i)).^2)/16).*omega(w)
).*k_d1(w).'))) ;
                a_d1_t(tt, w, i, j) = bsxfun(@times, (sin(-
t(tt)*omega(w).'), (bsxfun(@times, (bsxfun(@rdivide, ((cosh(bsxfun(@times, (j-
1), k_d1(w).'))), sinh(k_d1(w).*d1).' ), (H_d1(w, i)/2).*omega(w).^2).')))...
                    + bsxfun(@times, (sin(-
t(tt)*2*omega(w).'), (bsxfun(@times, (bsxfun(@rdivide, ((cosh(bsxfun(@times, (j-
1), (2*k_d1(w).'))), (sinh(k_d1(w).*d1).^4), ((3*(H_d1(w, i)).^2)/8).*omega(w)
).^2).*k_d1(w).'))) ;
                Fi_d1_t(tt, w, i, j) = (Cm*rho*pi*D.^2/4)*a_d1_t(tt, w, i, j);
                Fd_d1_t(tt, w, i, j) =
(Cd*rho/2)*D*abs(u_d1_t(tt, w, i, j)).*u_d1_t(tt, w, i, j);
                F_d1_t(tt, w, i, j) = Fi_d1_t(tt, w, i, j) + Fd_d1_t(tt, w, i, j);

                u_d1_max(w, i, j) = (max(u_d1_t(:, w, i, j)));
                a_d1_max(w, i, j) = (max(a_d1_t(:, w, i, j)));
                Fi_d1_max(w, i, j) = (max(Fi_d1_t(:, w, i, j)));
                Fd_d1_max(w, i, j) = (max(Fd_d1_t(:, w, i, j)));
                F_d1_max(w, i, j) = max((F_d1_t(:, w, i, j)));

            %global forces and moments on the soil
            F_d1_global(tt, w, i) = sum(F_d1_t(tt, w, i, :), 4);
            F_d1_global_max(w, i) = max(F_d1_global(:, w, i));
            M_d1_t(tt, w, i, j) = F_d1_t(tt, w, i, j)*(j-1);
            M_d1_global(tt, w, i) = sum(M_d1_t(tt, w, i, :), 4);

```

```

M_d1_global_max(w,i) = max(M_d1_global(:,w,i));

j=j+1;
end
%%%%%%%%%%%%%%%%%%%%%%%%%%%%%%%%%%%%%%%%%%%%%%%%%%%%%%%%%%%%%%%%%%%%%%%%FFT at MWL_d1%%%%%%%%%%%%%%%%%%%%%%%%%%%%%%%%%%%%%%%%%%%%%%%%%%%%%%%%%%%%%%%%%%%%%%%%
forcefft_d1_0m_1=(fft(F_d1_t(:,w,i,28),n));
forcefft_d1_0m(:,w,i,28)=abs(forcefft_d1_0m_1(1:n_2/2))./(n/2);
%%%%%%%%%%%%%%%%%%%%%%%%%%%%%%%%%%%%%%%%%%%%%%%%%%%%%%%%%%%%%%%%%%%%%%%%

%%%%%%%%%%%%%%%%%%%%%%%%%%%%%%%%%%%%%%%%%%%%%%%%%%%%%%%%%%%%%%%%%%%%%%%%FFT total forces_d1%%%%%%%%%%%%%%%%%%%%%%%%%%%%%%%%%%%%%%%%%%%%%%%%%%%%%%%%%%%%%%%%%%%%%%%%
forcefft_d1_global_1=(fft(F_d1_global(:,w,i),n));
forcefft_d1_global(:,w,i)=abs(forcefft_d1_global_1(1:n_2/2))./(n/2);
%%%%%%%%%%%%%%%%%%%%%%%%%%%%%%%%%%%%%%%%%%%%%%%%%%%%%%%%%%%%%%%%%%%%%%%%

%%%%%calculations for d2=33m%%%%%%%%%%%%%%%%%%%%%%%%%%%%%%%%%%%%%%%%%%%%%%%%%%%%%%%%%%%%%%%%%%%%%%%%
for k=1:(34+(round((zeta_d2_t(tt,w,i))))))
%1=sea bottom, 28= MWL

u_d2_t(tt,w,i,k) = (bsxfun(@times, (cos(-
t(tt)*omega(w).')), (bsxfun(@times, (bsxfun(@rdivide, ((cosh(bsxfun(@times, (k-
1), k_d2(w).'))), sinh(k_d2(w).*d2).')), ((H_d2(w,i)/2).*omega(w).')))...
+bsxfun(@times, (cos(-
t(tt)*2*omega(w).')), (bsxfun(@times, (bsxfun(@rdivide, ((cosh(bsxfun(@times, (k-
1), (2*k_d2(w).'))))), (sinh(k_d2(w).*d2).')).^4), ((3*(H_d2(w,i)).^2)/16).*omega(w)
).*k_d2(w).'))));
a_d2_t(tt,w,i,k) = bsxfun(@times, (sin(-
t(tt)*omega(w).')), (bsxfun(@times, (bsxfun(@rdivide, ((cosh(bsxfun(@times, (k-
1), k_d2(w).'))), sinh(k_d2(w).*d2).')), ((H_d2(w,i)/2).*omega(w).^2).')))...
+bsxfun(@times, (sin(-
t(tt)*2*omega(w).')), (bsxfun(@times, (bsxfun(@rdivide, ((cosh(bsxfun(@times, (k-
1), (2*k_d2(w).'))))), (sinh(k_d2(w).*d2).')).^4), ((3*(H_d2(w,i)).^2)/8).*omega(w)
).^2).*k_d2(w).'))));
Fi_d2_t(tt,w,i,k) = (Cm*rho*pi*D.^2/4)*a_d2_t(tt,w,i,k);
Fd_d2_t(tt,w,i,k) =
(Cd*rho/2)*D*abs(u_d2_t(tt,w,i,k)).*u_d2_t(tt,w,i,k);
F_d2_t(tt,w,i,k) = Fi_d2_t(tt,w,i,k) + Fd_d2_t(tt,w,i,k);

u_d2_max(w,i,k) = (max(u_d2_t(:,w,i,k)));
a_d2_max(w,i,k) = (max(a_d2_t(:,w,i,k)));
Fi_d2_max(w,i,k) = (max(Fi_d2_t(:,w,i,k)));
Fd_d2_max(w,i,k) = (max(Fd_d2_t(:,w,i,k)));
F_d2_max(w,i,k) = max((F_d2_t(:,w,i,k)));

%global forces and moments on the soil
F_d2_global(tt,w,i) = sum(F_d2_t(tt,w,i,:),4);
F_d2_global_max(w,i) = max(F_d2_global(:,w,i));
M_d2_t(tt,w,i,k) = F_d2_t(tt,w,i,k)*(k-1);
M_d2_global(tt,w,i) = sum(M_d1_t(tt,w,i,:),4);
M_d2_global_max(w,i) = max(M_d2_global(:,w,i));

k=k+1;
end
%%%%%%%%%%%%%%%%%%%%%%%%%%%%%%%%%%%%%%%%%%%%%%%%%%%%%%%%%%%%%%%%%%%%%%%%FFT at MWL_d2%%%%%%%%%%%%%%%%%%%%%%%%%%%%%%%%%%%%%%%%%%%%%%%%%%%%%%%%%%%%%%%%%%%%%%%%
forcefft_d2_0m_1=(fft(F_d2_t(:,w,i,34),n));
forcefft_d2_0m(:,w,i,34)=abs(forcefft_d2_0m_1(1:n_2/2))./(n/2);
%%%%%%%%%%%%%%%%%%%%%%%%%%%%%%%%%%%%%%%%%%%%%%%%%%%%%%%%%%%%%%%%%%%%%%%%

%%%%%%%%%%%%%%%%%%%%%%%%%%%%%%%%%%%%%%%%%%%%%%%%%%%%%%%%%%%%%%%%%%%%%%%%FFT total forces_d2%%%%%%%%%%%%%%%%%%%%%%%%%%%%%%%%%%%%%%%%%%%%%%%%%%%%%%%%%%%%%%%%%%%%%%%%
forcefft_d2_global_1=(fft(F_d2_global(:,w,i),n));
forcefft_d2_global(:,w,i)=abs(forcefft_d2_global_1(1:n_2/2))./(n/2);
%%%%%%%%%%%%%%%%%%%%%%%%%%%%%%%%%%%%%%%%%%%%%%%%%%%%%%%%%%%%%%%%%%%%%%%%

tt=tt+1;
end
i=i+1;
end

```

```

w=w+1;
end

F_d1_global_17_1 = F_d1_global(:,17,1);
F_d1_global_1_1 = F_d1_global(:,1,1);

%%

%%%%%%%%%%%%%%%%%%%%%%%%%%%%%%%%%%%%%%%%%%%%%%%%%%%%%%%%%%%%%%%%%%%%%%%%Plotting the amplitudes%%%%%%%%%%%%%%%%%%%%%%%%%%%%%%%%%%%%%%%%%%%%%%%%%%%%%%%%%%%%%%%%%%%%%%%%
figure ('Name','Forces acting at the struture')
fsize = 14;
lw = 1.2;
subplot(1,2,1) %Total Forces over length in d1
plot (squeeze(F_d1_max(1,1,:)),z_d1,'-xr', squeeze(F_d1_max(1,5,:)),z_d1,'-
xb',squeeze(F_d1_max(17,1,:)),z_d1,'-or', squeeze(F_d1_max(17,5,:)),z_d1,'-ob')
set(gca,'FontSize',fsize,'Box','on')
grid on
xlabel('Wave Force [N]','FontSize',fsize)
ylabel('z [m]','FontSize',fsize)
axis([0 4*10.^5 -35 10])
legend({'F morison_R_S_2_0_T_6', 'F morison_R_S_4_0_T_6',...
'F morison_R_S_2_0_T_1_4', 'F morison_R_S_4_0_T_1_4'},
'Location','Southeast')
title('Water Depth d = 27 m' , 'FontSize',fsize)
%
subplot(1,2,2) %Total Forces over water depth in d2
fsize = 14;
lw = 1.2;
plot (squeeze(F_d2_max(1,1,:)),z_d2,'-xr', squeeze(F_d2_max(1,5:)), z_d2,'-
xb',squeeze(F_d2_max(17,1:)),z_d2,'-or', squeeze(F_d2_max(17,5:)), z_d2,'-ob')
set(gca,'FontSize',fsize,'Box','on')
grid on
xlabel('Wave Force [N]','FontSize',fsize)
ylabel('z [m]','FontSize',fsize)
axis([0 4*10.^5 -35 10])
legend({'F morison_R_S_2_0_T_6', 'F morison_R_S_4_0_T_6',...
'F morison_R_S_2_0_T_1_4', 'F morison_R_S_4_0_T_1_4'},
'Location','Southeast')
title('Water Depth d = 33 m','FontSize',fsize)
%
figure ('Name','Drag and Inertia Forces over water depth') %)Drag and Inertia
Forces over water depth in d2; H1
subplot(1,2,1)
fsize = 14;
lw = 1.2;
plot (squeeze(Fi_d1_max(1,1:)),z_d1,'-xr', squeeze(Fd_d1_max(1,1:)), z_d1,'-
xb',squeeze(Fi_d1_max(17,1:)),z_d1,'-or', squeeze(Fd_d1_max(17,1:)),z_d1,'-ob')
set(gca,'FontSize',fsize,'Box','on')
grid on
xlabel('Wave Force [N]','FontSize',fsize)
ylabel('z [m]','FontSize',fsize)
axis([0 4*10.^5 -35 10])
grid on
legend({'Fi morison_R_S_2_0_T_6', 'Fd morison_R_S_2_0_T_6',...
'Fi morison_R_S_2_0_T_1_4', 'Fd morison_R_S_2_0_T_1_4'},
'Location','Southeast')
title('Water Depth d = 27 m','FontSize',fsize)

subplot(1,2,2)
fsize = 14;
lw = 1.2;
plot (squeeze(Fi_d2_max(1,1:)),z_d2,'-xr', squeeze(Fd_d2_max(1,1:)), z_d2,'-
xb',squeeze(Fi_d2_max(17,1:)),z_d2,'-or', squeeze(Fd_d2_max(17,1:)),z_d2,'-ob')
set(gca,'FontSize',fsize,'Box','on')
grid on
xlabel('Wave Force [N]','FontSize',fsize)
ylabel('z [m]','FontSize',fsize)

```

```

axis([0 4*10.^5 -35 10])
legend({'Fi morison_R_S_2_0_T_6', 'Fd morison_R_S_2_0_T_6',...
       'Fi morison_R_S_2_0_T_1_4', 'Fd morison_R_S_2_0_T_1_4'},
       'Location','Southeast')
title('Water Depth d = 33 m')
%
%%%%%%%%%%%%%%%%%%%%%%%%%%%%%%%%%%%%%%%%%%%%%%%%%%%%%%%%%%%%%%%%%%%%%%%%Plotting over time%%%%%%%%%%%%%%%%%%%%%%%%%%%%%%%%%%%%%%%%%%%%%%%%%%%%%%%%%%%%%%%%%%%%%%%%
figure ('Name','Forces over time at MWL')
subplot(2,2,1)
plot (t, F_d1_t(:,1,1,28),'-r',t, F_d1_t(:,1,5,28),'--b')
xlabel('t [s]')
ylabel('Wave Force [N]')
axis([0 35 -3.5*10.^5 3.5*10.^5])
grid on
grid minor
legend('F morison_d = 2_7_m, S = 1 / 2_0, T = 6_s', 'F
morison_d = 2_7_m, S = 1 / 4_0, T = 6_s','Location','Southeast')
title('Water Depth d = 27 m')
%
subplot(2,2,2)
plot (t, F_d1_t(:,17,1,28),'-r',t, F_d1_t(:,17,5,28),'--b') %the second term is
omega, the third term is height
xlabel('t [s]')
ylabel('Wave Force [N]')
axis([0 35 -4.5*10.^5 4.5*10.^5])
grid on
grid minor
legend('F morison_d = 2_7_m, S = 1 / 2_0, T = 1_4_._0_s', 'F
morison_d = 2_7_m, S = 1 / 4_0, T = 1_4_._0_s','Location','Southeast')
title('Water Depth d = 27 m')
%
subplot(2,2,3)
plot (t, F_d2_t(:,1,1,34),'-r',t, F_d2_t(:,1,5,34),'--b')
xlabel('t [s]')
ylabel('Wave Force [N]')
axis([0 35 -3.5*10.^5 3.5*10.^5])
grid on
grid minor
legend('F morison_d = 3_3_m, S = 1 / 2_0, T = 6_s', 'F
morison_d = 3_3_m, S = 1 / 4_0, T = 6_s','Location','Southeast')
title('Water Depth d = 33 m')

%
subplot(2,2,4)
plot (t, F_d2_t(:,17,1,34),'-r',t, F_d2_t(:,17,5,34),'--b') %the second term is
omega, the third term is height
xlabel('t [s]')
ylabel('Wave Force [N]')
axis([0 35 -3.5*10.^5 3.5*10.^5])
grid on
grid minor
legend('F morison_d = 3_3_m, S = 1 / 2_0, T = 1_4_._0_s', 'F
morison_d = 3_3_m, S = 1 / 4_0, T = 1_4_._0_s','Location','Southeast')
title('Water Depth d = 33 m')
%
figure ('Name','Forces over time at 6m above the seabed')
subplot(2,2,1)
plot (t, F_d1_t(:,1,1,7),'-r',t, F_d1_t(:,1,5,7),'--b')
xlabel('t [s]')
ylabel('Wave Force [N]')
axis([0 35 -3.5*10.^5 3.5*10.^5])
grid on
grid minor
legend('F morison_d = 2_7_m, S = 1 / 2_0, T = 6_s', 'F
morison_d = 2_7_m, S = 1 / 4_0, T = 6_s','Location','Southeast')
title('Water Depth d = 27 m')
%
%

```

```

subplot(2,2,2)
plot (t, F_d1_t(:,17,1,7), '-r', t, F_d1_t(:,17,5,7), '--b')
xlabel('t [s]')
ylabel('Wave Force [N]')
axis([0 35 -3.5*10.^5 3.5*10.^5])
grid on
grid minor
legend('F morison_d = 2_7_m, S = 1 / 2_0, T = 1_4_.0_s', 'F
morison_d = 2_7_m, S = 1 / 4_0, T = 1_4_.0_s', 'Location', 'Southeast')
title('Water Depth d = 27 m')
%
subplot(2,2,3)
plot (t, F_d2_t(:,1,1,7), '-r', t, F_d2_t(:,1,5,7), '--b')
xlabel('t [s]')
ylabel('Wave Force [N]')
axis([0 35 -3.5*10.^5 3.5*10.^5])
grid on
grid minor
legend('F morison_d = 3_3_m, S = 1 / 2_0, T = 6_s', 'F
morison_d = 3_3_m, S = 1 / 4_0, T = 6_s', 'Location', 'Southeast')
title('Water Depth d = 33 m')
%
subplot(2,2,4)
plot (t, F_d2_t(:,17,1,7), '-r', t, F_d2_t(:,17,5,7), '--b')
xlabel('t [s]')
ylabel('Wave Force [N]')
axis([0 35 -3.5*10.^5 3.5*10.^5])
grid on
grid minor
legend('F morison_d = 3_3_m, S = 1 / 2_0, T = 1_4_.0_s', 'F
morison_d = 3_3_m, S = 1 / 4_0, T = 1_4_.0_s', 'Location', 'Southeast')
title('Water Depth d = 33 m')
%%%%%%%%%%%%%%%%%%%%%%%%%%%%%%%%%%%%%%%%%%%%%%%%%%%%%%%%%%%%%%%%%%%%%%%%
%%%%%%%%%%%%%%%%%%%%%%%%%%%%%%%%%%%%%%%%%%%%%%%%%%%%%%%%%%%%%%%%%%%%%%%%Plotting FFT%%%%%%%%%%%%%%%%%%%%%%%%%%%%%%%%%%%%%%%%%%%%%%%%%%%%%%%%%%%%%%%%%%%%%%%%
figure (6)
fsize = 14;
lw = 1.2;
subplot(2,1,1)
plot(w_2,squeeze(forcefft_d1_0m(:,17,1,28)), '-
r',w_2,squeeze(forcefft_d2_0m(:,17,1,34)), '--
b',w_2,squeeze(forcefft_d1_0m(:,1,1,28)), '-
g',w_2,squeeze(forcefft_d2_0m(:,1,1,34)), '-y')
set(gca, 'FontSize', fsize, 'Box', 'on')
%set(gca, 'ytick', []) %hide y-values
xlabel('\omega [rad/s]', 'FontSize', fsize);
ylabel('Wave Force [N]', 'FontSize', fsize);
%axis([0 5 0 15*10.^6])
xlim([0 5])
grid on
legend('Ffft_d = 2_7_m, S = 1 / 2_0, T = 1_4_.0_s',
'Ffft_d = 3_3_m, S = 1 / 2_0, T = 1_4_.0_s', 'Ffft_d = 2_7_m, S = 1 / 2_0, T
= 6_s', 'Ffft_d = 3_3_m, S = 1 / 2_0, T = 6_s', 'Location', 'Southeast')
title('The Force FFT at MWL');

subplot(2,1,2)
fsize = 14;
lw = 1.2;
plot(w_2,squeeze(forcefft_d1_0m(:,17,5,28)), '-
r',w_2,squeeze(forcefft_d2_0m(:,17,5,34)), '--
b',w_2,squeeze(forcefft_d1_0m(:,1,5,28)), '-
g',w_2,squeeze(forcefft_d2_0m(:,1,5,34)), '-y')
set(gca, 'FontSize', fsize, 'Box', 'on')
%set(gca, 'ytick', []) %hide y-values
xlabel('\omega [rad/s]', 'FontSize', fsize);
ylabel('Wave Force [N]', 'FontSize', fsize);
%axis([0 5 0 15*10.^6])
xlim([0 5])
grid on

```

```

legend('Ffft_d = 2_7_m, S = 1 / 4_0, T = 1_4 . 0_s',
'Ffft_d = 3_3_m, S = 1 / 4_0, T = 1_4 . 0_s', 'Ffft_d = 2_7_m, S = 1 / 4_0, T = 6_s', 'Ffft_d = 3_3_m, S = 1 / 4_0, T = 6_s', 'Location', 'Southeast')
title('The Force FFT at MWL', 'FontSize', fsize);

figure (7)
fsize = 14;
lw = 1.2;
plot(w_2, squeeze(forcefft_d1_global(:,1,1)), '-b', w_2, squeeze(forcefft_d2_global(:,1,1)), '--r')
set(gca, 'FontSize', fsize, 'Box', 'on')
%set(gca, 'ytick', []) %hide y-values
xlabel('\omega [rad/s]', 'FontSize', fsize);
ylabel('Wave Force [N]', 'FontSize', fsize);
%axis([0 5 0 15*10.^6])
xlim([0 5])
grid on
legend('Ffft_d = 2_7_m, R_S_2_0_T_6',
'Ffft_d = 3_3_m, R_S_2_0_T_6', 'Location', 'Southeast')
title('FFT of the Global Force for RS20T6', 'FontSize', fsize);

figure (8)
fsize = 14;
lw = 1.2;
plot(w_2, squeeze(forcefft_d1_global(:,1,5)), '-b', w_2, squeeze(forcefft_d1_global(:,1,5)), '--r')
set(gca, 'FontSize', fsize, 'Box', 'on')
%set(gca, 'ytick', []) %hide y-values
xlabel('\omega [rad/s]', 'FontSize', fsize);
ylabel('Wave Force [N]', 'FontSize', fsize);
%axis([0 5 0 15*10.^6])
xlim([0 5])
grid on
legend('Ffft_d = 2_7_m, R_S_4_0_T_6',
'Ffft_d = 3_3_m, R_S_4_0_T_6', 'Location', 'Southeast')
title('FFT of the Global Force for RS40T6', 'FontSize', fsize);

figure (9)
fsize = 14;
lw = 1.2;
plot(w_2, squeeze(forcefft_d1_global(:,17,1)), '-b', w_2, squeeze(forcefft_d2_global(:,17,1)), '--r')
set(gca, 'FontSize', fsize, 'Box', 'on')
%set(gca, 'ytick', []) %hide y-values
xlabel('\omega [rad/s]', 'FontSize', fsize);
ylabel('Wave Force [N]', 'FontSize', fsize);
%axis([0 5 0 15*10.^6])
xlim([0 5])
grid on
legend('Ffft_d = 2_7_m, S_2_0_T_1_4',
'Ffft_d = 3_3_m, S_2_0_T_1_4', 'Location', 'Southeast')
title('FFT of the Global Force for RS20T14', 'FontSize', fsize);

figure (10)
fsize = 14;
lw = 1.2;
plot(w_2, squeeze(forcefft_d1_global(:,17,5)), '-b', w_2, squeeze(forcefft_d2_global(:,17,5)), '--r')
set(gca, 'FontSize', fsize, 'Box', 'on')
%set(gca, 'ytick', []) %hide y-values
xlabel('\omega [rad/s]', 'FontSize', fsize);
ylabel('Wave Force [N]', 'FontSize', fsize);
%axis([0 5 0 15*10.^6])
xlim([0 5])
grid on

```

```
legend('Ffft_d = 2_7_m, S_4_0_T_1_4',  
'Ffft_d = 3_3_m, S_4_0_T_1_4', 'Location', 'Southeast')  
title('FFT of the Global Force for RS40T14', 'FontSize', fsize);  
  
%%%%%%%%%%%%%%%%%%%%%%%%%%%%%%%%%%%%%%%%%%%%%%%%%%%%%%%%%%%%%%%%%%%%%%%%  
figure(11)  
plot (t, F_d1_global(:,17,1), '-r')%, t, F_d2_global(:,17,1), '--b')  
xlabel('t [s]')  
ylabel('Wave Force [N]')  
axis([0 50 -8*10.^6 8*10.^6])  
grid on  
grid minor  
legend('F linear-morison', 'Location', 'Southeast')  
title('Global force for RS20T14; D=9m;')
```

A.2 Diagrams

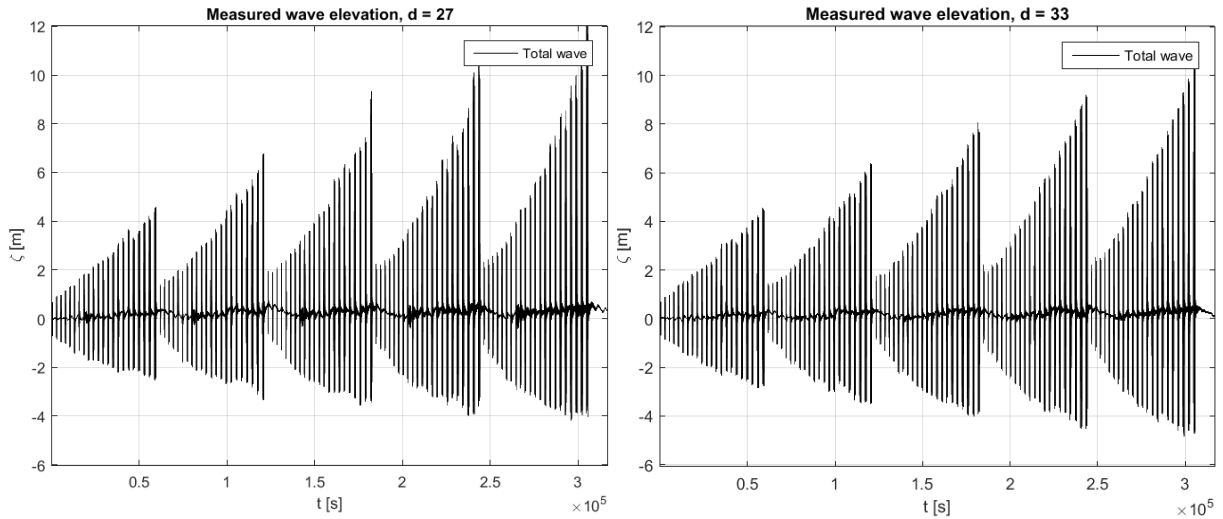


Figure 46: Whole wave-elevation set from gentle to severe wave conditions (measured)

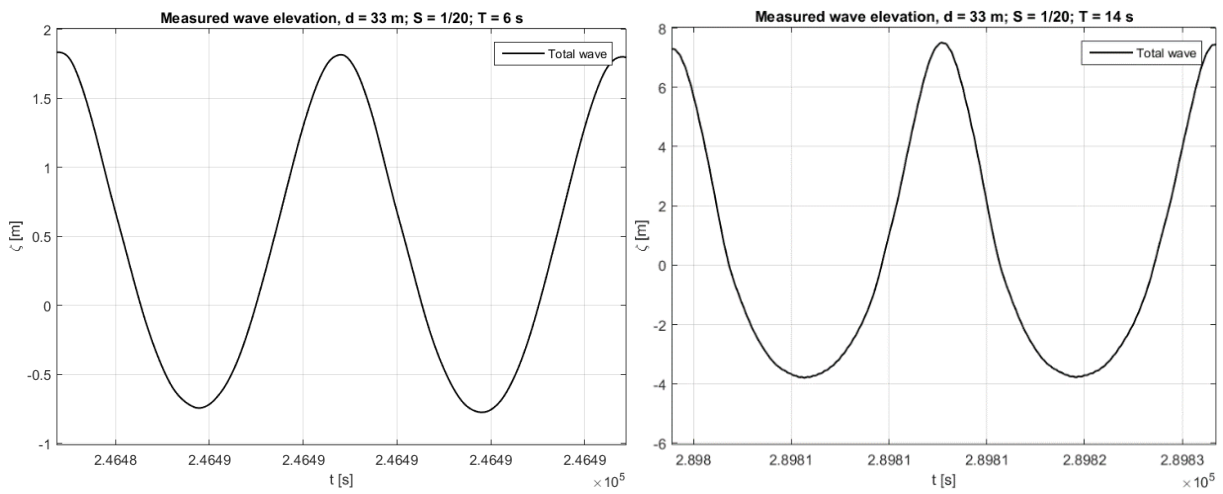


Figure 47: Measured wave elevation for two selected sea states (d = 33 m)

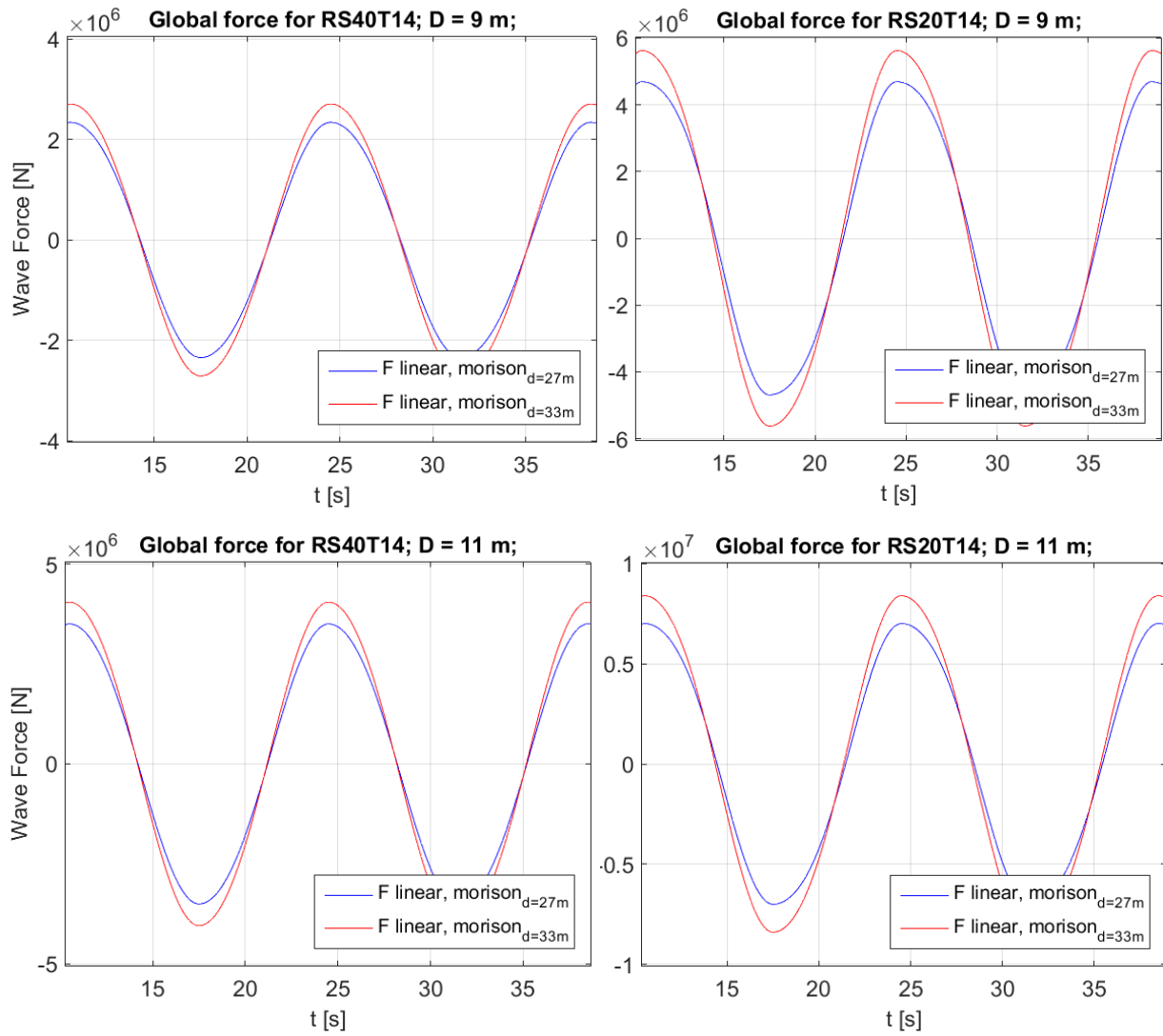


Figure 48: Global force for two wave conditions in two water depths and for two pile diameters, using first-order Morison equation

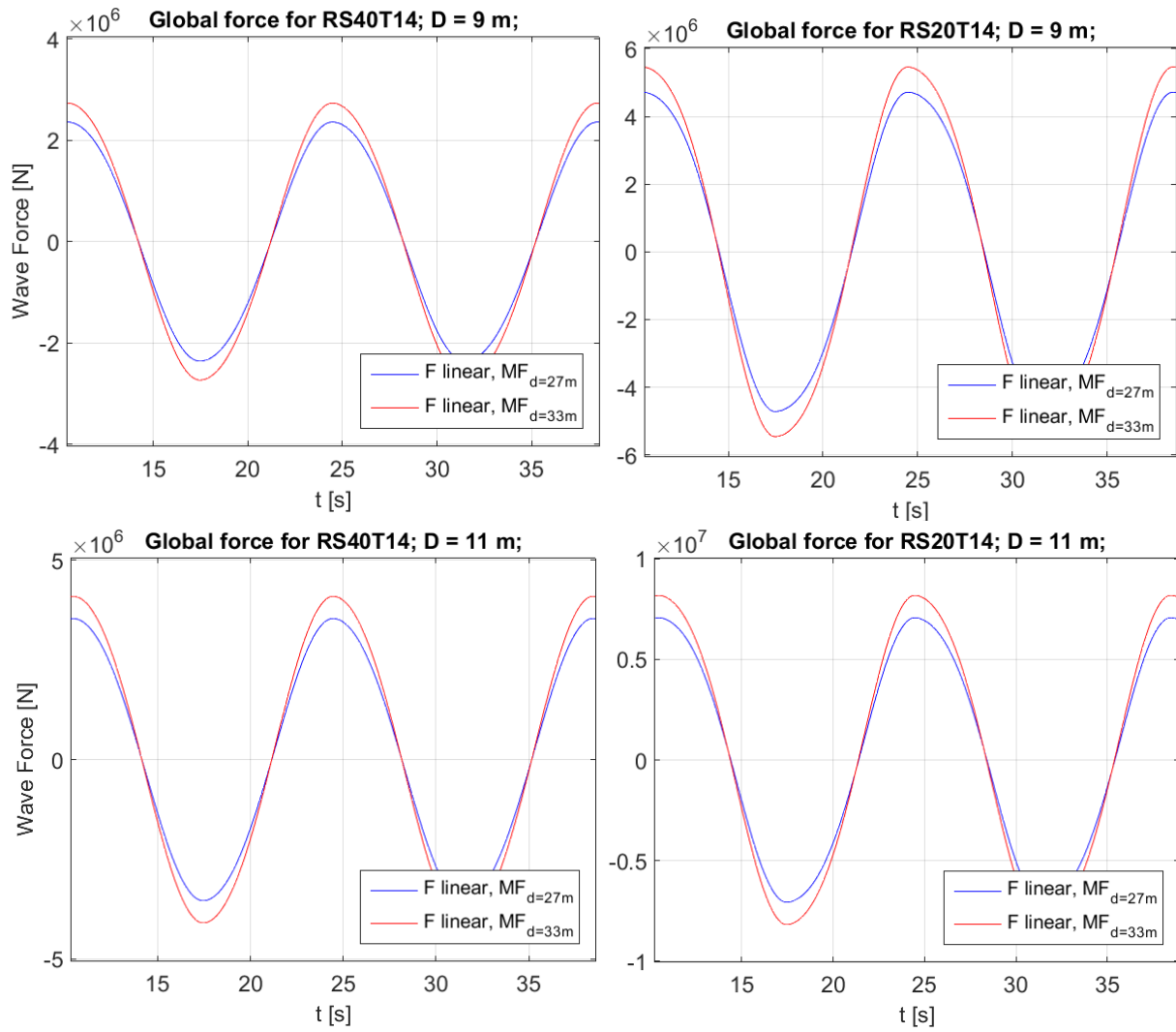


Figure 49: Global force for two wave conditions in two water depths and for two pile diameters, using first-order MacCamy-Fuchs equation (drag term included)

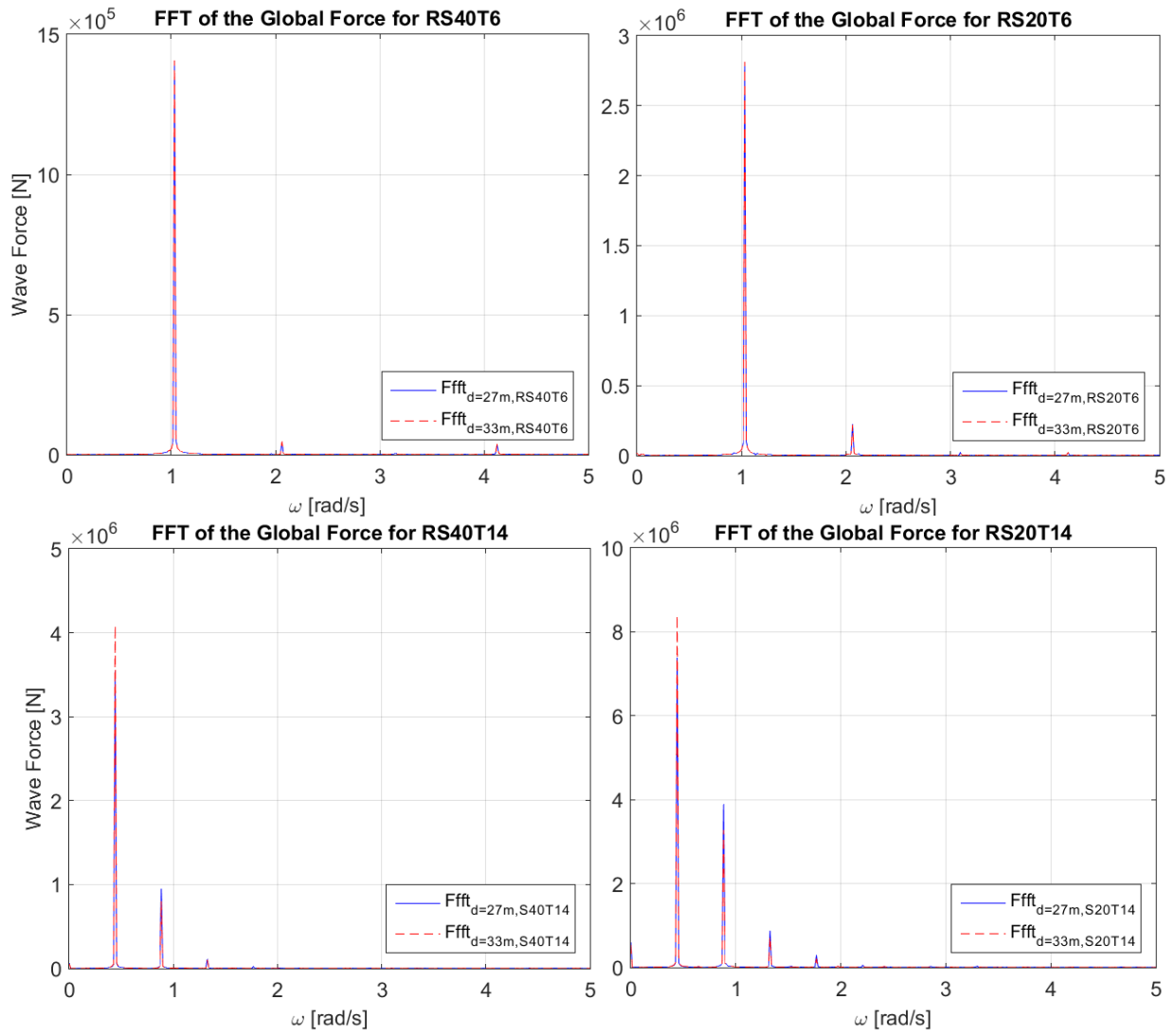


Figure 50: FFT of the global force for four wave conditions in two water depths, using second-order Morison equation ($D = 11$ m)

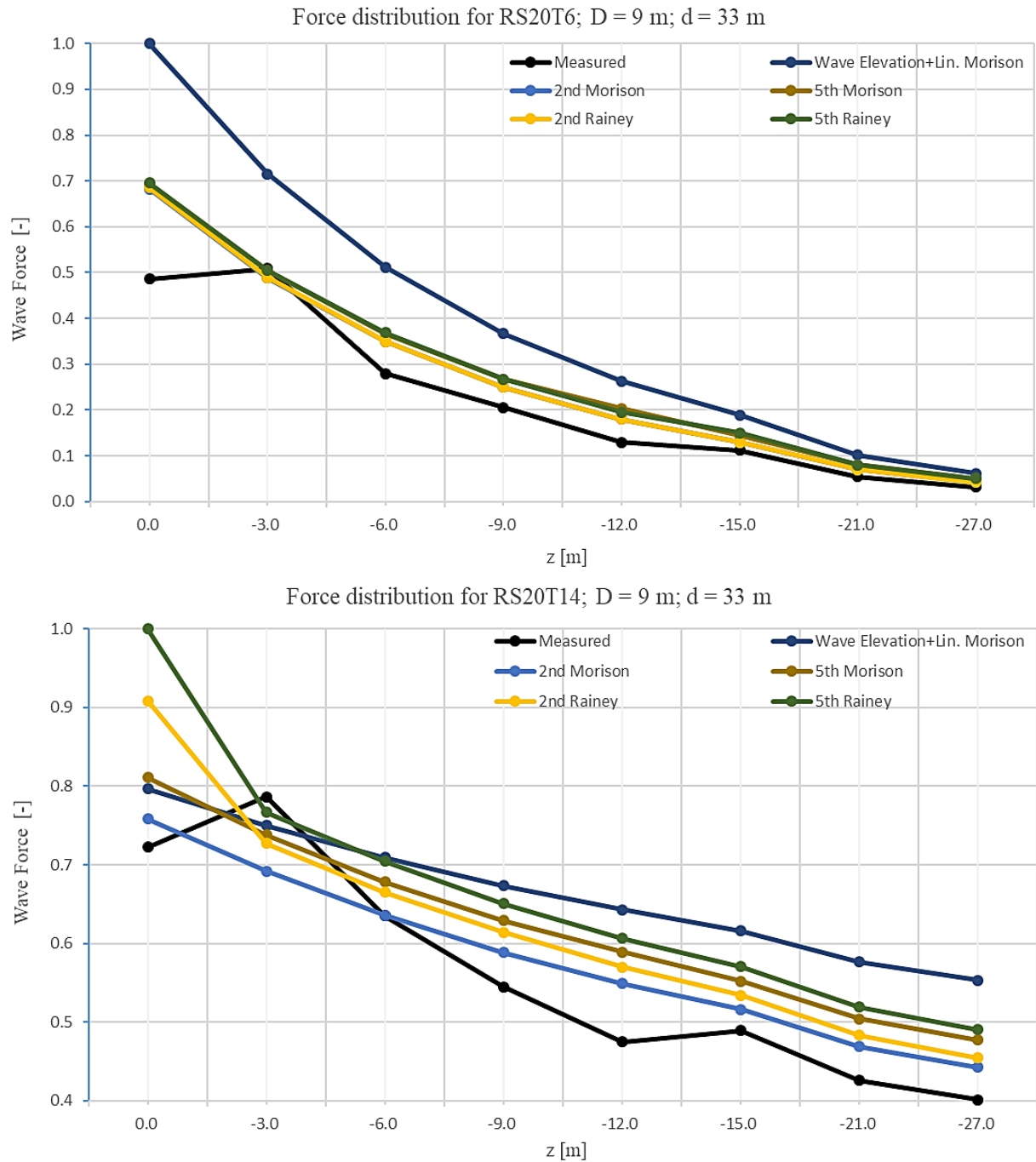


Figure 51: Comparison of the total force distribution over the length of structure, $d = 33$ m (calculated force obtained from the measured wave-elevation is additionally given)

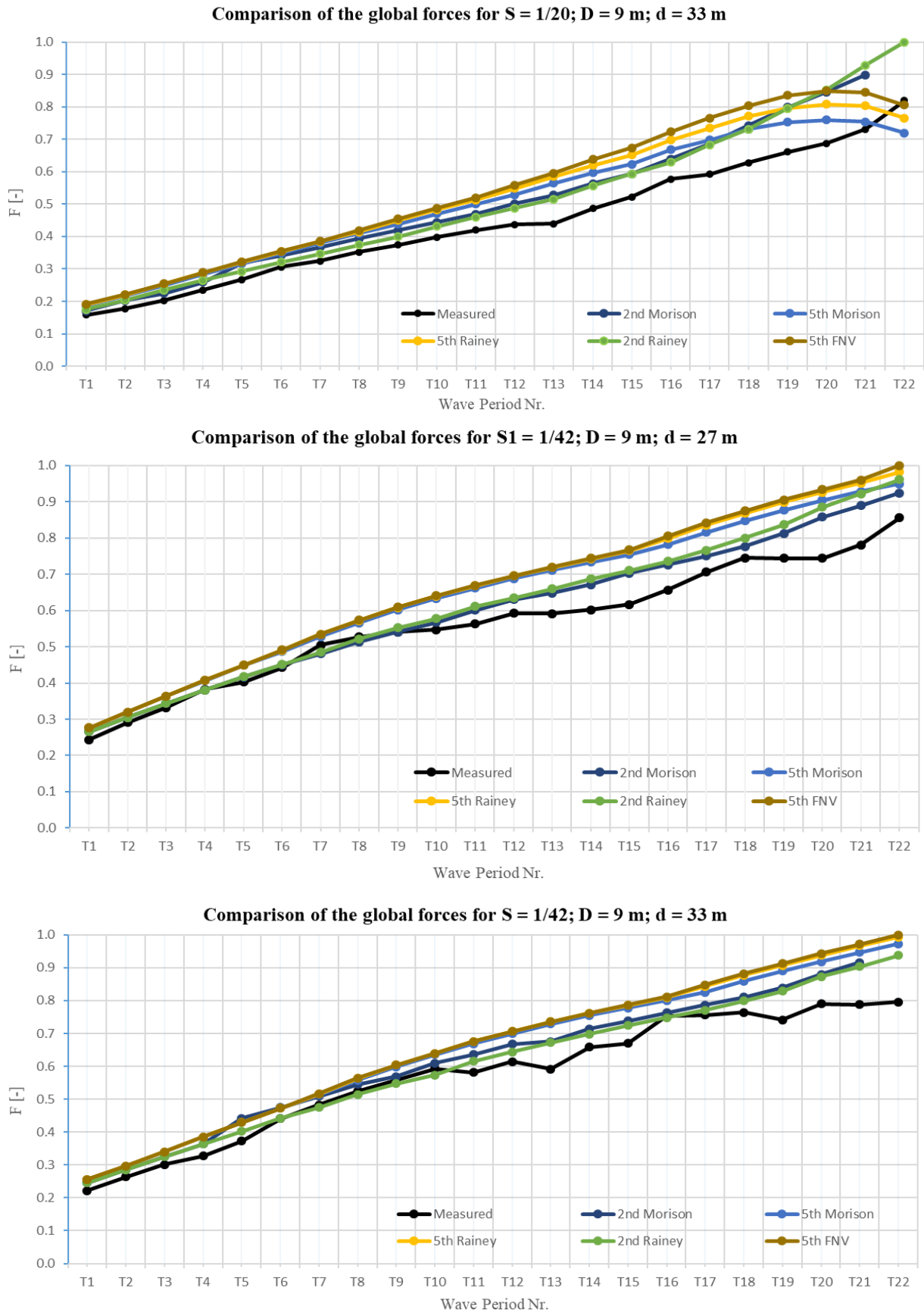


Figure 52: Comparison of highest global forces for all wave periods

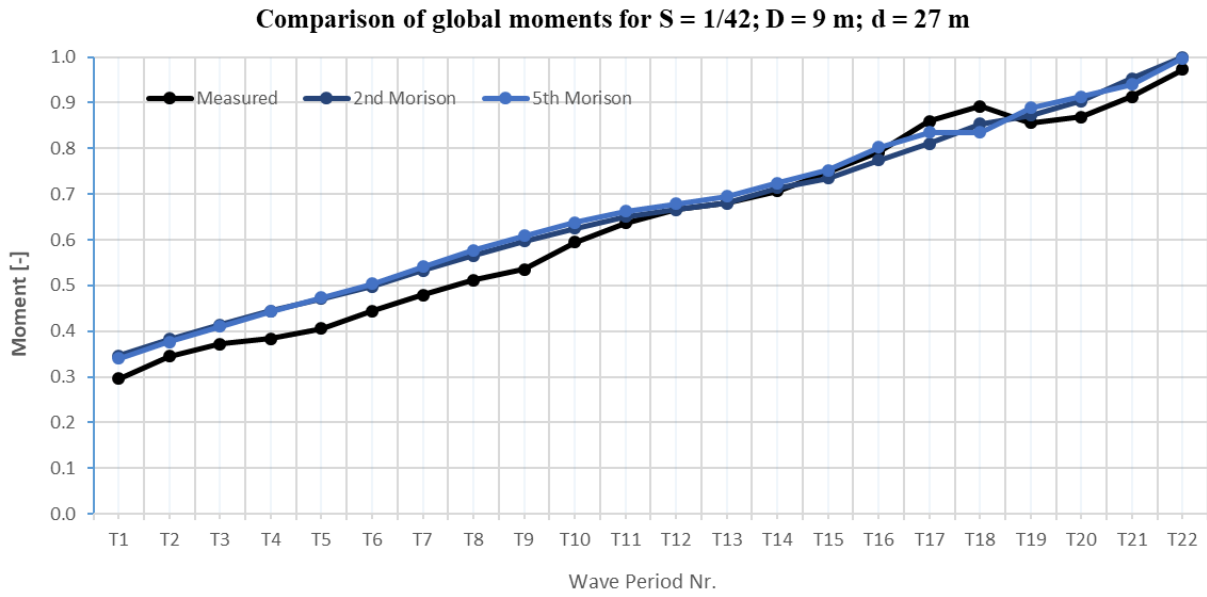


Figure 53: Comparison of highest global moments for all wave periods

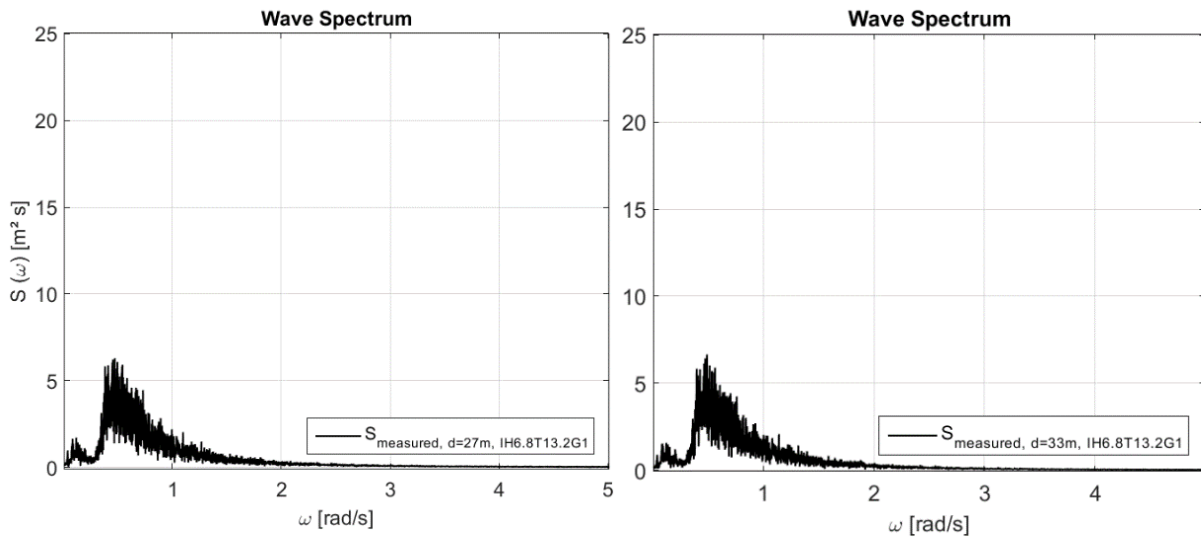


Figure 54: Examples of irregular wave spectra for IH6.8T13.2G1 in two water depths

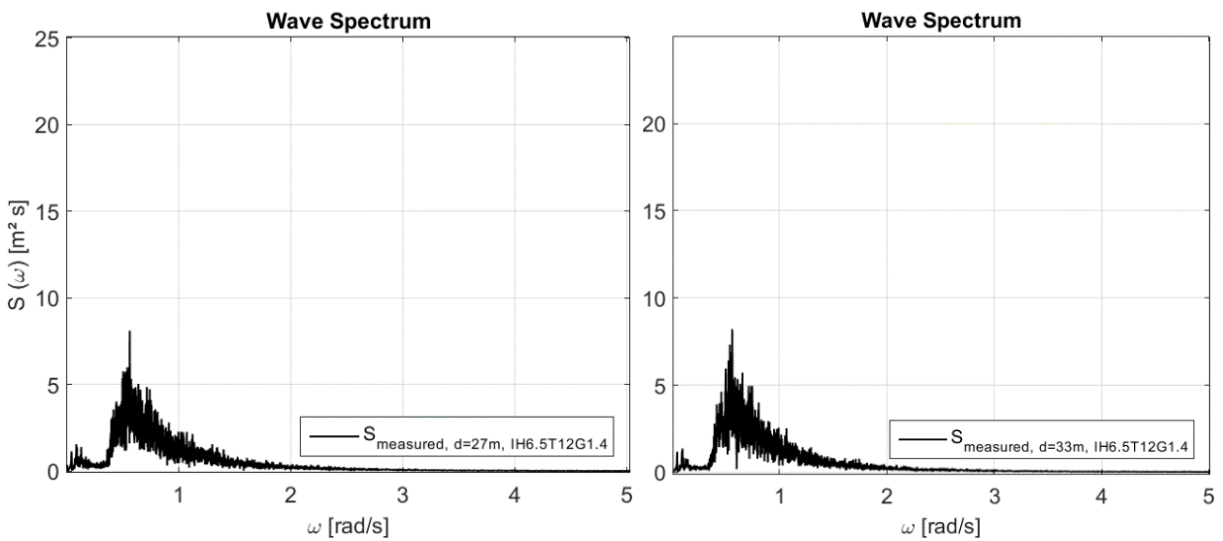


Figure 55: Examples of irregular wave spectra for IH6.5T12G1.4 in two water depths